4-2012

An Exploration of Neutron Detection in Semiconducting Boron Carbide

Nina Hong
University of Nebraska-Lincoln, ninahong@huskers.unl.edu

An Exploration of Neutron Detection in Semiconducting Boron Carbide

by

Nina Hong

A DISSERTATION

Presented to the Faculty of

The Graduate College of the University of Nebraska

In Partial Fulfillment of Requirements

For the Degree of Doctor of Philosophy

Major: Physics & Astronomy

Under the Supervision of Professor Shireen Adenwalla

Lincoln, Nebraska

April, 2012

An Exploration of Neutron Detection in Semiconducting Boron Carbide

Nina Hong, Ph.D.

University of Nebraska, 2012

Advisor: Shireen Adenwalla

The ^{3}He supply problem in the U.S. has necessitated the search for alternatives for neutron detection. The neutron detection efficiency is a function of density, atomic composition, neutron absorption cross section, and thickness of the neutron capture material. The isotope ^{10}B is one of only a handful of isotopes with a high neutron absorption cross section—3840 barns for thermal neutrons. So a boron carbide semiconductor represents a viable alternative to ^{3}He. This dissertation provides an evaluation of the performance of semiconducting boron carbide neutron detectors grown by plasma enhance chemical vapor deposition (PECVD) in order to determine the advantages and drawbacks of these devices for neutron detection. Improved handling of the PECVD system has resulted in an extremely stable plasma, enabling deposition of thick films of semiconducting boron carbide. A variety of material and semiconducting characterization tools have been used to investigate the structure and electronic properties of boron carbide thin films, including X-ray diffraction, X-ray photoelectron spectroscopy, atomic force microscopy, infrared/Raman spectroscopy, current-voltage measurements and capacitance-voltage measurements. Elemental concentrations in the boron carbide films have been obtained from Rutherford backscattering and elastic recoil detection analysis.

Solid state neutron detection devices have been fabricated in the form of heterostructured p-n diodes, p-type boron carbide/n-type Si. Operating conditions, including applied bias voltage, and time constants, have been optimized for maximum detection efficiency and correlated to the semiconducting properties investigated in separate electronic measurements. Accurate measurements of the neutron detection efficiency and the response of the detector to a wide range of neutron wavelengths have been performed at a well calibrated, tightly collimated, "white" cold neutron beam source using time-of-flight neutron detection technique. Because neutron detection measurements indicate that charge capture in boron carbide is affected by the nanocrystalline/amorphous nature of the semiconductor, the effects of incomplete charge collection efficiencies on the neutron detection efficiencies and pulse height spectra in heterostructured p-n diode neutron detectors have been modeled using a Monte Carlo GEANT4 simulation.

The dissertation ends with suggestions for devices with improved neutron detection efficiencies.

Acknowledgements

First and foremost, I thank God for raising and cheering me up along this long journey.

My sincerest appreciation to my advisor, Professor Shireen Adenwalla for her guidance, encouragement, and valuable discussions throughout my graduate work. She has been my mentor and role model.

In completing this dissertation, I have had the benefit of constructive criticism from my committee members: Professor Brian Robertson, Professor Peter Dowben, and Professor Kirill Belashchenko. I greatly appreciate their time and efforts.

I would like to thank my research mentors and colleagues: Ellen Day, Andrew Baruth, Abhijit Mardana, Ravi Billa, Sam Davis, Dhairyashil Aher, Keith Foreman, Uday Singh, John Mullins, A. Dwayne Riley, Michael Chu, Anil Rajapitamahuni, and Wei Xiong. In addition special thanks to Professor Mathias Schubert and his students for their fruitful discussions and interest in this project.

I am especially indebted to my previous advisor, Professor Y.P. Lee of Hanyang University who has broadened my horizons as a physicist.

Finally, I want to thank my family for their everlasting trust in me.

Table of Contents

List of Figures

List of Tables

Acronyms/Abbreviations

AES	Auger Electron Spectroscopy
AFM	Atomic Force Microscope
BC	Boron Carbide
$B_5C_1H_2$	Boron Carbide
CAMD	Center for Advanced Microstructures & Devices
$C_2B_{10}H_{12}$	Orthocarborane (Other types of isomers are not discussed in this dissertation.)
C-V	Capacitance-Voltage
CVD	Chemical Vapor Deposition
DD	Deuterium-Deuterium
DT	Deuterium-Tritium
DSP	Digital Signal Processor
ENDF	Evaluated Nuclear Data File
ERDA	Elastic Recoil Detection Analysis
DOE	Department of Energy
DSP	Digital Signal Processor
FT-IR	Fourier Transform Infrared
GEANT4	Geometry And Tracking4
HF	Hydrofluoric acid
HFIR	High Flux Isotope Reactor
IBA	Ion Beam Analysis
IR	Infrared

I-V	Current-Voltage
JFET	Junction gate Field-Effect-Transistor
LANL	Los Alamos National Laboratory
LCVD	Laser Chemical Vapor Deposition
MFC	Mass Flow Controller
ORNL	Oak Ridge National Laboratory
PECVD	Plasma Enhanced Chemical Vapor Deposition
RBS	Rutherford Backscattering Spectroscopy
RF(rf)	Radio Frequency
RPM	Radiation Portal Monitor
SCCM	Standard Cubic Centimeters per Minute
SE	Spectroscopic Ellipsometry
SNM	Special Nuclear Materials
TOF	Time-of-Flight
UNL	University of Nebraska-Lincoln
V_{bi}	Built-in Potential
XANES	X-ray Absorption Near Edge Structure
XPS	X-ray Photoelectron Spectroscopy
XRD	X-Ray Diffraction
XRR	X-Ray Reflectivity

Chapter 1 Introduction

This dissertation is focused on an exploration of boron carbide thin film based neutron detectors for real-world applications as an alternative to ^{3}He detectors and supports the hypothesis that boron carbide neutron detectors are attractive candidates for the next generation of commercially realizable neutron detectors. Determining the ultimate performance of boron carbide detectors has previously been difficult because of the lack of knowledge of their material characteristics and because of irreproducibility and lack of stability of the thin films. Consequently, the exploration of semiconducting boron carbide neutron detectors in this dissertation is devoted to exploring two major streams: (i) neutron detection experiments or simulations using the boron carbide material (Chapter 6-9) and (ii) independent studies to investigate the physical and electronic properties of the material in the thin film (Chapter 2-5).

The dissertation begins, in Chapter 2, with a discussion regarding the optimal conditions for boron carbide sample preparation using Plasma Enhanced Chemical Vapor Deposition (PECVD). The crucial improvement reported here is the ability to maintain a stable plasma for long periods of time in order to deposit thick films, because thick boron carbide films are indispensable in enhancing the neutron detection efficiency. Chapter 3 employs ion beam analysis (IBA) techniques to obtain the exact elemental compositions of thin and thick boron carbide films and reveal that the films contain a certain amount of hydrogen as well as boron and carbon. The molecular structures of boron carbide films are inferred from infrared (IR) and Raman spectroscopies in Chapter 4. The elemental information from Chapter 3 validates the use of the fingerprint method to identify the resonant vibrational frequencies in IR and Raman spectra. Previous work had shown that boron carbide films can change from p-type to n-type semiconductors with the addition of Ni as a dopant. Chapter 5 is focused on the control of Ni

dopant concentrations and the resulting Fermi level shifts of the Ni-doped boron carbides, which are both important to the development of homojunction boron carbide p-n diode neutron detectors. Chapter 6 introduces general concepts regarding the generation and moderation of neutrons and neutron detection. Neuron detection experiments using thermal neutrons and a heterojunction boron carbide/n-type Si p-n diode are described in Chapter 7 and similar experiments with cold neutrons are described in Chapter 8. Specifically, Chapter 8 details neutron detection as a function of neutron wavelength using time-of-flight (TOF) techniques, as well as allowing for a detailed and reliable measure of neutron detection efficiency. The boron carbide neutron detectors employed in this dissertation are based on heterostructure p-n diodes where the p and the n type materials differ in their crystal/electronic structures, and charge transport properties. A Monte Carlo simulation using GEANT4 introduced in Chapter 9 allows for predictions of efficiency and pulse height spectra as a function of semiconducting properties in the heterostructured p-n diode neutron detectors.

This dissertation concludes with a summary that describes the progress achieved so far and details ideas for future experiments.

Chapter 2 Preparation of PECVD Grown Boron Carbide Thin Films

Part of the work reported in this chapter on XPS was performed in collaboration with Marjorie A. Langell of Department of Chemistry, University of Nebraska-Lincoln, Lincoln, NE, U.S.A.

2.1 Introduction

Since the first discovery of a boron carbide compound in 1858, there have been many different material preparation routes [1], each of which results in specific combinations of composition and structure, and both physical and chemical properties. Figure 2.1 shows one boron-carbon phase diagram that reveals the wide phase homogeneity range for bulk boron carbides. Among all possible phases, $B_{12}C_3$ (often called B_4C) is understood to be the stoichiometric single crystal boron carbide. A study of the free energy of boron carbides by Emin shows that replacing carbon atoms within B_4C with boron atoms enables a wide range of compositions explaining the wide single-phase regime [2].

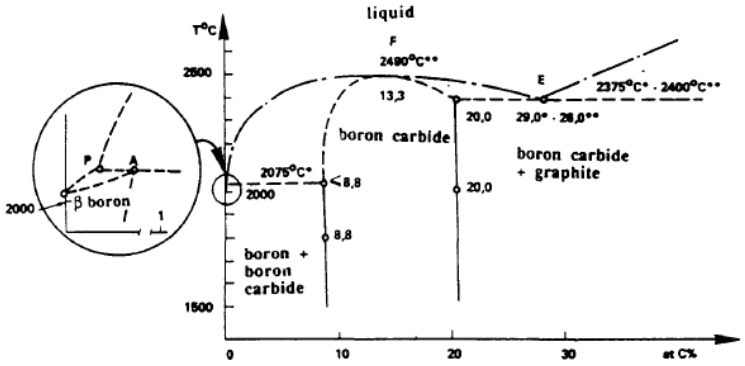

Figure 2. 1 Boron-carbon phase diagram. O: hot-pressed samples, P: peritexy, F: congruent melting, E: eutectic (adapted from Ref. [3]). —•— (adapted from Ref. [4]), ——— corresponds to vertical limits, – – – – (adapted from [5-8]). Figure adapted from Ref. [1].

The study of phase diagrams for thin films of the boron-carbon system deposited by laser chemical vapor deposition (LCVD) from a reaction gas mixture consisting of BCl_3, CH_4, and H_2 showed multiple phases, rhombohedral boron carbide and graphite (stable phases), and a tetragonal boron rich carbide (meta-stable phase) [9]. In general, phase diagrams for thin films show a strong dependence on the deposition technique and vacuum conditions [10]. Various deposition techniques have been used to grow boron carbide thin films: RF/DC magnetron sputtering using boron carbide targets (mostly B_4C) [11-13], reactive sputtering using a boron target [14], ion beam deposition [15], pulsed laser deposition [16] and chemical vapor deposition (CVD) [17-26]. Plasma Enhanced CVD (PECVD) grown boron carbide films [20-32] show semiconducting properties, enabling applications that include semiconducting diode devices [21, 24, 26], Fermi level engineering via impurity doping [23, 26, 30] and all solid state neutron detectors [32-35]. The semiconducting properties are highly sensitive to deposition conditions and the particular growth technique. This chapter outlines the film fabrication methods and other useful information related to the deposition procedures for the PECVD grown boron carbides.

2.2 PECVD system

PECVD is a film deposition technique in which chemical reactions occur between gaseous source molecules and a plasma. This deposition technique yields fast deposition rates without loss in film quality and is often used in semiconductor manufacturing [28, 36-41].

The PECVD chamber used in boron carbide film growth consists of two parts: a main deposition chamber [24], based on the Gaseous Electronics Conference design [42], consisting of a 10 inch stainless steel sphere and a second chamber connected to the main chamber via a gate valve. The second chamber enables sample loading to the main chamber without opening the PECVD chamber. This load lock system enables us to keep the surface of the PECVD chamber

passivated so that we obtain the desirable boron carbide film composition (more details are given in section 2.3.3). In addition to functioning as a load-lock, the second chamber is used for sputter deposition of various magnetic and nonmagnetic metal targets. For device fabrication, *in-situ* sputter deposition of electrodes on a film is possible using mask systems. PECVD chamber accessories such as gas lines, RF power, temperature controlling system, vacuum pumps, have been illustrated and explained in the theses and dissertations of previous group members [43-46].

2.3 Sample depositions

2.3.1 Source molecules

While sputter depositions use solid state targets to grow a crystal, PECVD uses vapor phase source molecules. The molecular structure and stoichiometry of source compounds may or may not be preserved in films grown by PECVD and this may be investigated by comparing molecular bonds in the precursor and the thin films (see Chapter 4), as well as by measurements of the elemental composition of thin films (see Chapter 3). Three different icosahedral carborane isomers: *ortho-*, *meta-*, *para- closo*-dicarbadodecaborane(12) ($C_2B_{10}H_{12}$) [47] have been used at UNL as source compounds for semiconducting boron carbide films. They are distinguished by the differing positions of carbon atoms in the icosahedral cage, resulting in different optical and electrical properties of the corresponding films [48, 49]. In this dissertation, we deal with the *ortho* isomer, orthocarborane (o-carborane), as the source molecule for boron carbide films. We also describe nickelocene, which is used for n-type doping of the boron carbide films.

Orthocarborane (*ortho*-carborane, or *closo*-1,2,-dicarbodecaborane) has been successfully used as a source molecule for the growth of semiconducting boron carbide films on n- or p-type Si substrates [20, 21, 24, 26], n-type SiC substrates [24], and insulating substrates [50]. The

icosahedral molecular structure of orthocarborane is shown on the left side of figure 2.2. The two black spheres represent carbon atoms, with the remaining ten apical sites occupied by boron atoms. The twelve hydrogen atoms that are bonded to the carbon and boron atoms are not shown in the figure. Orthocarborane, with the natural isotopic abundance of boron (19% ^{10}B) is purchased from Sigma-Aldrich [51] in the form of a white powder. The product has 98% purity and a molecular weight of 144.23 g/mol. It melts at 260 ℃ and the heat of sublimation measured at 300 K is 70 kJ/mol [52]. The hydrogen bonds are relatively weak, resulting in a significant loss of the bonds after thin film deposition while the 5:1 ratio of boron to carbon is well preserved (see Chapter 3).

Nickelocene (nickel-biscyclopentadienyl, $Ni(C_5H_5)_2$, or $NiCp_2$), an n-type dopant for the boron carbide film [23], is an alkali-metal cyclopentadienyl complex where the Cp ligand bonds to Ni through all five carbon atoms as shown on the right-hand side of figure 2.2. The molecule was purchased from Sigma-Aldrich [51] in the form of a green powder. This organonickel compound has been also used as a source molecule to prepare Ni films using decomposed Ni atoms from gaseous nickelocene on a hot substrate [53, 54]. The hydrocarbon ligands are released after the decomposition. The Ni in the PECVD grown boron carbide films, however, is incorporated into the icosahedral cage [27] and does not exist as a pure metal. In order to avoid the well-known light-induced decomposition [55], the nickelocene was handled and kept in the dark.

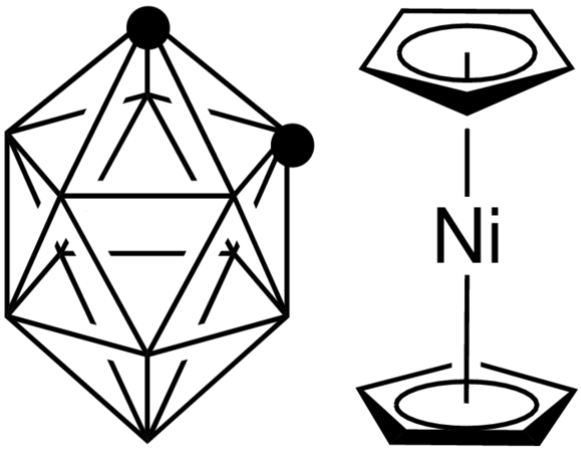

Figure 2. 2 A cartoon of the molecular structure for orthocarborane and nickelocene. Figure adapted from [51].

2.3.2 Substrates

Numerous substrates have been shown to be suitable for growth of boron carbide films. The cleaning processes and deposition conditions differ slightly, depending on the type of substrate.

The most commonly used semiconducting substrates were n-type or p-type Si substrates. Si wafers are cleaned in acetone, methanol, and deionized water in an ultrasonic cleaner for 5 min. The wafers are then chemically etched in 4.9% hydrofluoric (HF) acid solution to remove the surface SiO_2 layer, as checked by ellipsometry measurements [56]. Boron carbide films on the Si grow and adhere with or without post-annealing. For insulating substrates, various optically transparent substrates were tested: glass, A- or R- plane sapphire, and quartz. They were cleaned using a similar process as described for the Si wafers, with the exception of HF. Films on insulating substrates were not as robust and delaminated fairly easily. Additional heat treatments of the substrates increased the time over which the films were stable, but these, too, eventually delaminated. The delamination problem is thought to originate from significantly

different thermal expansion coefficients between the boron carbide film and the substrate used. However, an *in-situ* post-annealing at 600 ℃ in an Ar atmosphere after film growth prevented film delamination. The use of insulating substrates enabled fabrication of resistive boron carbide devices, magnetic tunnel junction devices, and semiconducting thin film transistors. As is discussed later in Chapter 3, post-annealing changes the elemental composition on the surface of the boron carbide film.

Si/SiO_2 substrates are widely used as an insulating substrate for many electronic devices. The substrate was relatively thin and fragile compared to the other insulating substrates mentioned above and so was much easier to cut to a suitable size for the devices. The substrate was tested for boron carbide film growth with the same cleaning process as for the other oxide substrates. As-deposited boron carbide films on Si/SiO_2 substrates did not show any delamination. Deposition on insulating Si/SiO_2 substrate, therefore, excluded possible concerns about modified surface effects on device properties which might arise in the devices during post-annealing.

2.3.3 Deposition conditions

The deposition protocol for PECVD has been well described in Ref. [43] and the films described in this dissertation followed the same deposition process, unless mentioned otherwise. In this section, the deposition conditions are outlined and additional explanations are given about the parameters that differ from those in Ref. [43].

The following list gives the parameters chosen for the PECVD grown boron carbide films:

- Reactor or carrier gas: Ar.
- Substrate temperature for deposition: 330 – 350 ℃.
- Temperature of carrier gas lines: 90 ℃.

- Temperature of PECVD chamber: 90 ℃.
- Temperature of the orthocarborane source molecule vial: 90 ℃. (This temperature was previously set at 70 ℃ but has been changed to 90 ℃ to avoid arc discharge in the PECVD chamber during deposition, caused by a temperature difference between the orthocarborane and its carrier gas. Previously, arcing hindered long depositions.)
- Temperature for the nickelocene dopant molecule vial: Room temperature. (This temperature is lower than the temperature of carrier gas, but did not cause arcing because the amount of dopant introduced to the chamber was small.)
- Base pressure for PECVD chamber: 10^{-6} to 10^{-7} Torr.
- Working pressure for PECVD chamber: 200 mTorr in an Ar atmosphere
- RF power: 30W
- Plasma etching of substrate prior to deposition: 30 min in an Ar plasma.
- Post-annealing condition: After film growth, the chamber temperature was increased to 600 ℃ over a period of one hour, held stable for 20 min, and then slowly cooled down to 90 ℃ over times longer than one hour.
- The Ni doping concentration was controlled by changing the flow of Ar gas to the orthocarborane and nickelocene vials by using the mass flow controllers (MFC) settings. For example, we can fix the MFC that controls the flow to the orthocarborane vial at 1 SCCM and vary the MFC to the nickelocene vial as required. This change will give us information about relative changes in Ni dopant concentration.
- Chamber passivation: The passivation of the main chamber inner surfaces was done by performing a 10 min test deposition of orthocarborane molecules in a cleaned

chamber. This step is important in obtaining the correct right ratio (5:1) of boron to carbon. Figure 2.3 is an X-ray photoelectron spectroscopy (XPS) for boron carbide films grown in a passivated chamber (red line) and virgin chamber (black line). On both films, carbon peaks are clearly visible but the sample deposited in the virgin chamber did not show a boron peak. Moreover, the film grown in a virgin chamber is easily delaminated even on Si substrates. From the XPS results, we conclude that a passivation process is necessary for all boron carbide film growth. We hypothesize that the thin insulating coating that is deposited on the PECVD chamber's inner walls changes the electric field distribution.

Earlier theses and dissertations have described the process of deposition in extensive detail. Key improvements that enabled the measurements described in the rest of this dissertation include: (1) detailed process parameter control: In particular, the rf power and the temperature of the carrier gas and the source molecule were carefully controlled during the deposition, (2) chamber passivation enabled us to make films with the appropriate stoichiometry, and (3) post-annealing processes broadened the substrate choices. The improvements resulted in greatly improved semiconducting properties. Briefly, we were able to fabricate diodes with much smaller leakage currents (nA-μA) and much greater reverse breakdown voltages (>40 V), we were able to make much thicker films and maintain the stoichiometry over the entire thickness range, and we were able to control the amount of Ni doping and hence the Fermi level with unprecedented accuracy.

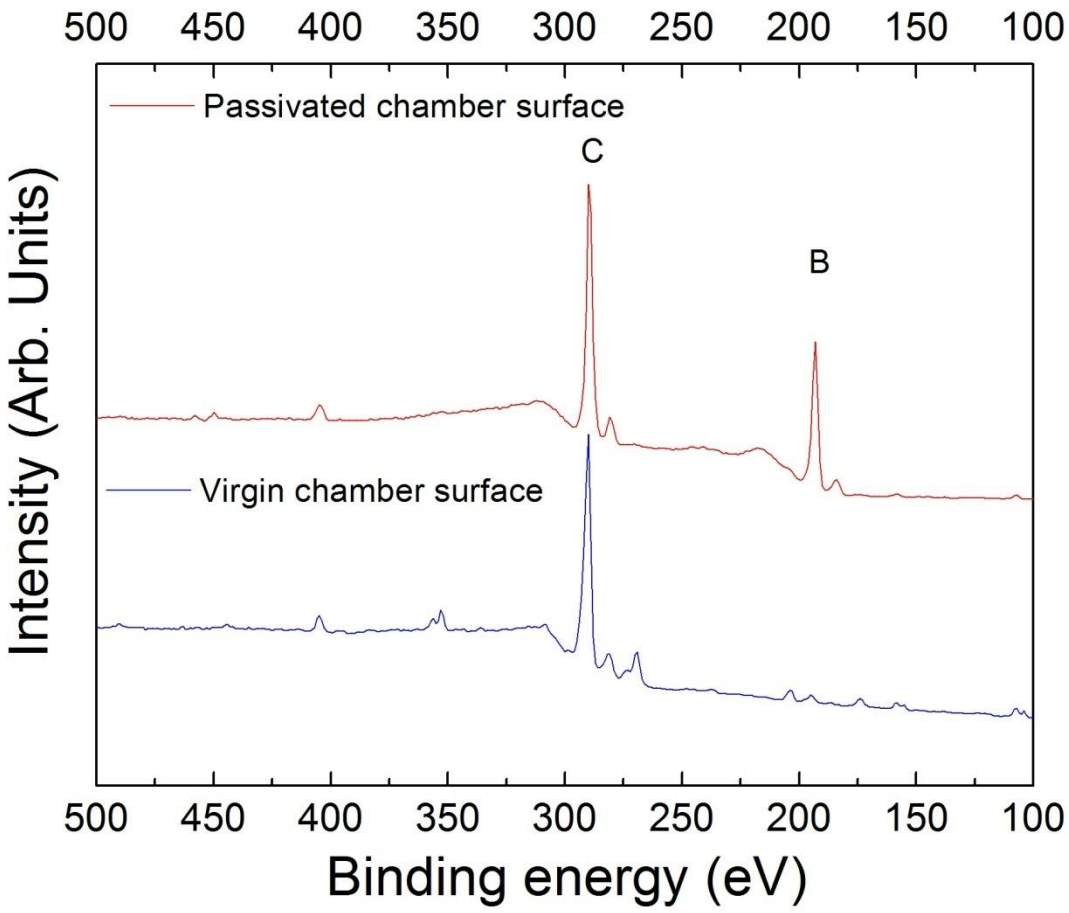

Figure 2. 3 XPS spectra of undoped boron carbide films on Si substrates. Passivation of the PECVD chamber surface is necessary if we are to obtain the desirable boron to carbon ratio in the thin film.

REFERENCES

1. Thévenot, F., *Boron carbide- comprehensive review.* Journal of the European Ceramic Society, 1990. **6**(4): p. 205-225.
2. Emin, D., *Structure and single-phase regime of boron carbides.* Physical Review B, 1988. **38**(9): p. 6041-6055.
3. Elliott, R.P., *THE BORON-CARBON SYSTEM. Quarterly Report No. 3, November 1, 1960-January 31, 1961*, in *Other Information: Project Agreement No. 4. Orig. Receipt Date: 31-DEC-61*. 1961. p. 11.
4. Kieffer, R., et al., *Investigations on the systme boron-carbon silicon.* Ber. der Deut. Keram. Ges , (West Germany), 1972. **49**(2): p. 41-46.
5. Bouchacourt, M., *Etudes sur la phase carbure de bore: corrélations propriétés-composition*. 1982.
6. Bouchacourt, M., F. Thevenot, and J. Ruste, *Études sur le carbure de bore iii. domaine d'existence de la phase carbure de bore.* Journal of the Less Common Metals, 1978. **59**(2): p. 139-152.
7. Bouchacourt, M. and F. Thevenot, *The melting of boron carbide and the homogeneity range of the boron carbide phase.* Journal of the Less Common Metals, 1979. **67**(2): p. 327-331.
8. Bouchacourt, M. and F. Thevenot, *Analytical investigations in the B-C system.* Journal of the Less Common Metals, 1981. **82**(0): p. 219-226.
9. Oliveira, J.C. and O. Conde, *Deposition of boron carbide by laser CVD: a comparison with thermodynamic predictions.* Thin Solid Films, 1997. **307**: p. 29-37.
10. Ohring, M., *Materials Science of Thin Films*. 2nd ed: Academic Press.

11. Chiang, C.L., H. Holleck, and O. Meyer, *Properties of RF sputtered B_4C thin films.* Nuclear Instruments and Methods in Physics Research Section B: Beam Interactions with Materials and Atoms, 1994. **91**: p. 692-695.

12. Knotek, O., E. Lugscheider, and C.W. Siry, *Tribological properties of B-C thin films deposited by magnetron-sputter-ion plating method.* Surface and Coatings Technology, 1997. **91**(3): p. 167-173.

13. Jacobsohn, L.G., et al., *X-ray photoelectron spectroscopy investigation of boron carbide films deposited by sputtering.* Surface Science, 2004. **572**: p. 418-424.

14. Lee, K.E., et al., *Preparation of boron carbide thin films from reactive sputtering of boron.* physica status solidi (b), 2004. **241**(7): p. 1637-1640.

15. Blumenstock, G., M., K. Keski, and M. R. A, *Ion-beam-deposited boron carbide coatings for the extreme ultraviolet*. Vol. 33. 1994, Washington, DC, ETATS-UNIS: Optical Society of America. 2.

16. Kokai, F., et al., *Laser ablation of boron carbide: thin-film deposition and plume analysis.* Diamond and Related Materials, 2001. **10**: p. 1412-1416.

17. Postel, O. and J. Heberlein, *Deposition of boron carbide thin film by supersonic plasma jet CVD with secondary discharge.* Surface and Coatings Technology, 1998. **108**: p. 247-252.

18. Sezer, A.O. and J.I. Brand, *Chemical vapor deposition of boron carbide.* Materials Science and Engineering: B, 2001. **79**(3): p. 191-202.

19. Conde, O., A.J. Silvestre, and J.C. Oliveira, *Influence of carbon content on the crystallographic structure of boron carbide films.* Surface and Coatings Technology, 2000. **125**: p. 141-146.

20. Lee, S., et al., *Characterization of boron carbide thin films fabricated by plasma enhanced chemical vapor deposition from boranes.* Journal of Applied Physics, 1992. **72**(10): p. 4925-4933.

21. Hwang, S.-D., et al., *Fabrication of boron-carbide/boron heterojunction devices.* Applied Physics Letters, 1996. **68**(11): p. 1495-1497.

22. Byun, D., et al., *Comparison of different chemical vapor deposition methodologies for the fabrication of heterojunction boron-carbide diodes.* Nanostructured Materials, 1995. **5**(4): p. 465-471.

23. Hwang, S., et al., *Nickel doping of boron carbide grown by plasma enhanced chemical vapor deposition.* Journal of Vacuum Science & Technology B: Microelectronics and Nanometer Structures, 1996. **14**(4): p. 2957-2960.

24. Adenwalla, S., et al., *Boron carbide/n-silicon carbide heterojunction diodes.* Applied Physics Letters, 2001. **79**(26): p. 4357-4359.

25. Ahmad, A., A., et al., *Optical properties of boron carbide (B_5C) thin films fabricated by plasma-enhanced chemical-vapor deposition.* Journal of Applied Physics, 1996. **79**(11): p. 8643-8647.

26. Hong, N., et al., *Ni doping of semiconducting boron carbide.* Journal of Applied Physics, 2010. **107**(2): p. 024513.

27. Liu, J., et al., *The local structure of transition metal doped semiconducting boron carbides.* Journal of Physics D: Applied Physics, 2010. **43**(8): p. 085403.

28. Kim, B.-H., et al., *Photoluminescence of silicon quantum dots in silicon nitride grown by NH_3 and SiH_4.* Applied Physics Letters, 2005. **86**(9): p. 091908.

29. Padmanabhan, R., *Optical characterization of PECVD boron carbide films*. 2005: University of Nebraska--Lincoln.

30. Hwang, S.-D., et al. *Nickel doping of boron--carbon alloy films and corresponding Fermi level shifts*. Journal of Vacuum Science & Technology A, 1997. **15**(3):p. 854-859.

31. Lee, S., et al., *The structural homogeneity of boron carbide thin films fabricated using plasma-enhanced chemical vapor deposition from B_5H_9+CH_4.* Journal of Applied Physics, 1993. **74**(11): p. 6919-6924.

32. Hong, N., et al., *Boron carbide based solid state neutron detectors: the effects of bias and time constant on detection efficiency.* Journal of Physics D: Applied Physics, 2010. **43**(27): p. 275101.

33. Day, E., M.J. Diaz, and S. Adenwalla, *Effect of bias on neutron detection in thin semiconducting boron carbide films.* Journal of Physics D: Applied Physics, 2006. **39**(14): p. 2920.

34. Caruso, A. N., et al., *The all boron carbide diode neutron detector: Comparison with theory.* Materials Science & Engineering B, 2006. **135**: p.129-133.

35. Caruso, A. N., *The physics of solid-state neutron detector materials and geometries*. Journal of Physics: Condensed Matter, 2010. **22**(44):p.443201.

36. Meyyappan, M., *A review of plasma enhanced chemical vapour deposition of carbon nanotubes.* Journal of Physics D: Applied Physics, 2009. **42**(21): p. 213001.

37. Li, B.S., et al., *High quality ZnO thin films grown by plasma enhanced chemical vapor deposition.* Journal of Applied Physics, 2002. **91**(1): p. 501-505.

38. Meyyappan, M., *Plasma nanotechnology: past, present and future.* Journal of Physics D: Applied Physics, 2011. **44**(17): p. 174002.

39. Li, Y., et al., *Preferential Growth of Semiconducting Single-Walled Carbon Nanotubes by a Plasma Enhanced CVD Method.* Nano Letters, 2004. **4**(2): p. 317-321.

40. Paquette, M., M. , et al., *The local physical structure of amorphous hydrogenated boron carbide: insights from magic angle spinning solid-state NMR spectroscopy.* Journal of Physics: Condensed Matter, 2011. **23**(43): p. 435002.

41. Hayashi, K., et al., *Investigation of the effect of hydrogen on electrical and optical properties in chemical vapor deposited on homoepitaxial diamond films.* Journal of Applied Physics, 1997. **81**(2): p. 744-753.

42. Hargis, P. J. Jr., et al., *The Gaseous Electronics Conference radio-frequency reference cell: A defined parallel-plate radio-frequency system for experimental and theoretical studies of plasma-processing discharges.* Review of Scientific Instruments, 1994. **65**(1): p. 140-154.

43. Day, E.E., *Boron carbide devices for neutron detection applications*, in *Ph.D. dissertation, The University of Nebraska - Lincoln*. 2006.

44. Billa, R.B., *Optical properties of semiconducting boron carbide for neutron detection applications*, in *Ph.D. dissertation, The University of Nebraska - Lincoln*. 2009.

45. Welsch, P., *Boron carbide and diodes: Electrical characteristics and neutron detection*, in *MS dissertation, The University of Nebraska - Lincoln*. 2002.

46. Aher, D.U., *Mechanical properties of PECVD boron carbide.* Ph.D. dissertation, The University of Nebraska - Lincoln, 2011.

47. Paroli, R.M., et al., *Variable-temperature and -pressure vibrational spectra of o-carborane.* Inorganic Chemistry, 1989. **28**(10): p. 1819-1823.

48. Lunca-Popa, P., et al., *Evidence for multiple polytypes of semiconducting boron carbide (C_2B_{10}) from electronic structure.* Journal of Physics D: Applied Physics, 2005. **38**(8): p. 1248.

49. Caruso, A., N., et al., *The heteroisomeric diode.* Journal of Physics: Condensed Matter, 2004. **16**(10): p. L139.

50. Bernard, L., et al., *Magnetoresistance in boron carbide junctions.* Applied Physics Letters, 2003. **83**(18): p. 3743-3745.

51. *Sigma-Aldrich, http://www.sigmaaldrich.com.*

52. Gamba, Z. and B.M. Powell, *The condensed phases of carboranes.* The Journal of Chemical Physics, 1996. **105**(6): p. 2436-2440.

53. Brissonneau, L., et al., *MOCVD-Processed Ni Films from Nickelocene. Part II: Carbon Content of the Deposits.* Chemical Vapor Deposition, 1999. **5**(4): p. 143-149.

54. Pugmire, D.L., et al. *Nickelocene adsorption on single-crystal surfaces*. Journal of Vacuum Science & Technology A, 1999 **17**(4):p. 1581-1586.

55. Welipitiya, D., et al., *Fabrication of large arrays of micron-scale magnetic features by selective area organometallic chemical vapor deposition.* Journal of Applied Physics, 1996. **80**(3): p. 1867-1871.

56. Tompkins, H.G., *Handbook of Ellipsometry*. 2005: Springer-Verlag GmbH & Co. KG.

Chapter 3 Stoichiometry of PECVD Grown Boron Carbide Films

Part of the work reported in this chapter on RBS and ERDA was performed in collaboration with Y. Q. Wang of the Ion beam Materials Laboratory, Materials Science and Technology Division, Los Alamos National Laboratory, Los Alamos, NM, U.S.A. and Carina Höglund[1,2], Jens Jensen[2], Jens Birch[2], and Lars Hultman[2] of [1]European Spallation Source, Lund, Sweden and [2]Department of Physics, Chemistry and Biology (IFM), Thin Film Physics Division, Linköping University, Linköping, Sweden.

3.1 Ion Beam Analysis (IBA)

The elemental composition of the orthocarborane source molecule for boron carbide thin film deposition is $C_2B_{10}H_{12}$. The ratio of boron to carbon and the presence or absence of hydrogen in the resultant thin films are important quantities for calculations of the neutron detection efficiency and are difficult to ascertain with common techniques. Most X-ray techniques for compositional analysis are blind to hydrogen and x-ray diffraction experiments cannot distinguish B from C due to their very similar Z values (5 and 6). The presence of ^{10}B at a fraction of 20% in naturally occurring boron results in very high absorption of neutrons, leading to difficulties in the interpretation of neutron diffraction data.

There have been several attempts to investigate the composition of plasma enhanced chemical vapor deposition (PECVD) grown boron carbide films using X-ray photoelectron spectroscopy (XPS) [1] and Auger electron spectroscopy (AES) [2]. These show a range of compositions for the boron carbide films that depend upon deposition conditions, thickness, and heat treatments. These previous studies indicate the sensitivity to sample preparation conditions, but were unable to pinpoint the amount of hydrogen in the film.

Here, we have used two ion beam analysis techniques (IBA) to investigate the composition and elemental depth profiles of as-deposited and post-annealed boron carbide films on Si substrates. IBA refers to analytical techniques utilizing ion beams with energies in the MeV range to probe the elemental composition of light/heavy materials. The specific IBA techniques used in this dissertation are Rutherford backscattering spectrometry (RBS) and elastic recoil detection analysis (ERDA).

3.2 Rutherford Back Scattering (RBS)

RBS is an analytical technique which measures the number and energy of projectile ions (usually alpha particles and less commonly protons) backscattered from the atoms of a target foil [3]. The classical model for an elastic collision works well to describe the process of interaction between the bombarding ion and the target nucleus. In RBS experiments, the energies of the bombarding ion are chosen to be high enough so that interactions with the electron cloud do not lead to appreciable scattering except in the forward direction, but low enough so that the ion remains outside the nucleus and the interactions between the ion and the nucleus are purely electrostatic in nature.

The energy loss of a projectile ion backscattering at a given angle depends on the target atomic number and is given by the kinematic factor K which is the ratio of projectile energy after the scattering to before. The kinematic factor (K) is defined in equation (3.1), where E is the energy of the alpha particle, M_α is the mass of the incident alpha article, M_t is the mass of the target atom, and θ is the scattering angle.

$$K = \frac{E_{Scattered}}{E_{incident}} = \left[\frac{\sqrt{1-\left(\frac{M_\alpha sin\theta}{M_t}\right)^2}+\frac{M_\alpha cos\theta}{M_t}}{1+\frac{M_\alpha}{M_t}}\right]^2 \quad (3.1)$$

The energy loss mechanism for scattering is momentum transfer from the projectile to the target which is higher for lighter elements and results in higher accuracy of the mass resolution of RBS for light elements. Because the ions cannot be backscattered by atoms of smaller masses, alpha particles cannot be backscattered by hydrogen (and helium), so additional experiments are necessary to obtain the hydrogen concentration in boron carbide films.

The yield for alpha particles backscattered from a target into a given solid angle of detector is related to the differential scattering cross section, which relates to the probability of observing a scattering event. The differential scattering rate will depend on the density of target atoms and the intensity of the incident beam, as well as the interaction strength (or scattering length) of the target/ion pair. The differential scattering cross section ($\frac{\partial\sigma}{\partial\Omega}$) for RBS for alpha particles is described in equation (3.2), where Z_t is the target atomic number, Z_α is the alpha particle mass number, Ω is solid angle , and the total cross section is obtained by integrating over solid angle.

$$\frac{\partial\sigma}{\partial\Omega} = \left[\frac{Z_\alpha Z_t e^2}{4E}\right]^2 \cdot \frac{4}{sin^4\theta} \cdot \frac{\left[\sqrt{1-\left[\frac{M_\alpha sin\theta}{M_t}\right]^2}+cos\theta\right]^2}{\sqrt{1-\left[\frac{M_\alpha sin\theta}{M_t}\right]^2}} \tag{3.2}$$

The scattering cross section is proportional to the square of the atomic number of the target atom ($\sim Z_t^2$) leading to a higher relative yield for heavy elements. RBS is more sensitive to heavy elements, but this signal sensitivity should be distinguished from the mass resolution discussed above, which is higher for light elements.

RBS experiments were conducted at the Ion Beam Materials Laboratory at Los Alamos National Laboratory (LANL) [4]. Figure 3.1 shows a schematic diagram of the beam line for the RBS/ERDA measurements at LANL. RBS measurements were obtained on two thin boron

carbide films (~50 nm) on Si substrates, as-deposited and post-annealed at 600 ℃, using 2 MeV alpha particles. The alpha particle is normally incident on the target, the RBS detector is fixed at a scattering angle of 167° and covers a solid angle of 2.23 msr.

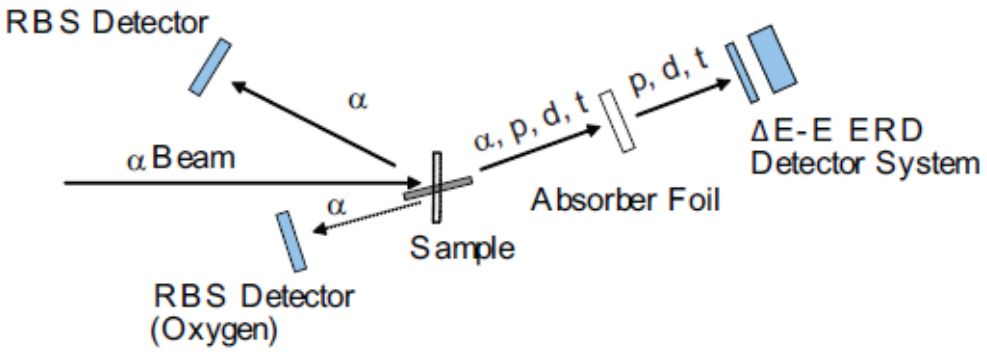

Figure 3. 1 A schematic diagram of the RBS and ERDA system in the Ion Beam Materials Laboratory at LANL. Figure adapted from Ref. [4].

Because the distance between nuclei (~2×10^{-10} m) is much larger than the size of nucleus (~10^{15} m) [3], the probability of the Rutherford backscattering collisions is small. Collisions with the electron cloud are more probable, but the low charge density in the electron cloud leads mainly to forward scattering. As the alpha particles travel through the film, they dissipate energy, and the energy dissipation is dependent on the material's stopping power [5]. For 2 MeV alpha particles, the stopping power and the corresponding range in the boron carbide film were calculated using SRIM/TRIM software [6], and are shown in table 3-1. Here, the electronic stopping power refers to the interactions of the alpha particle with the electrons and the nuclear stopping power refers to glancing collisions with the target nuclei. The projected range of 4.52 μm implies that the alpha particles penetrate the total thickness of the 50 nm films with minimal reduction in the energy.

Table 3. 1 SRIM/TRIM results for 2 MeV alpha particles in the boron carbide film. The density of boron carbide is 2.463 g/cc obtained from the critical edge measurement of X-ray reflectivity. Here, straggling refers to the square root of the variance of range representing the statistical fluctuation.

Alpha particle Energy	dE/dx (Elec.)	dE/dx (Nucl.)	Projected Range	Longitudinal Straggling	Lateral Straggling
2 MeV	1.495 MeV/(mg/cm^2)	1.164×10^{-3} MeV/(mg/cm^2)	4.52 μm	1499 Å	1236 Å

Figure 3.2 shows the spectrum for the as-deposited (black line) and post-annealed thin boron carbide film (red line) as a function of the scattered alpha particle energy. The higher energy peaks result from scattering off the heavier elements, with lower momentum transfer. The peaks are indexed to the respective elements. Because the orthocarborane source molecule contains naturally occurring boron with a ^{10}B: ^{11}B ratio of 1:4, we expect that the film will preserve that ratio. The two peaks for boron are separated by the different masses of the ^{10}B and ^{11}B nuclei, resulting in differing kinematic factors. The areal densities for ^{11}B, ^{12}C, and ^{16}O are obtained by integrating the area under the peak and normalizing to the appropriate cross section, and are shown in the figure in units of 10^{15} atoms/cm^2. Because the alpha particle penetrates the total thickness of the thin films, the areal density (the product of atomic density and thickness) is proportional to the total amount of each element in a given thickness of the film, without any need for adjustment for depth resolution. Any change in composition with depth would be invisible to RBS in this case.

The relative elemental ratio of the films are calculated based on the areal densities shown in figure 3.2 by taking into account the natural abundance of isotopes for boron, carbon, and oxygen. Table 3.2 shows the elemental ratio normalized to the carbon concentration. There is no

significant difference in the compositional ratio between the as-deposited and post-annealed thin films, but both ratios deviate quite significantly from the stoichiometry of the source molecule $C_2B_{10}H_{12}$ in which the boron/carbon ratio is 5 to 1. There are two possible scenarios: 1) carbon contamination of the surface results in a false higher carbon concentration, and/or 2) the PECVD process destroys the icosahedral cage of $C_2B_{10}H_{12}$ during film growth, leading to a totally different composition from that of the source molecule. Because we have previously observed adventitious carbon contamination on the surface [7], the former scenario is likely. An additional puzzling feature is the high concentration of oxygen. Previous X-ray photoelectron spectroscopy (XPS) results (see Chapter 4) indicate the presence of oxygen on the surface, indicating that the boron carbide film surface is easily oxidized. Since RBS results reflect the relative elemental concentrations within the whole 50 nm thickness, additional experiments (described later in this chapter) are necessary to clarify the elemental concentration.

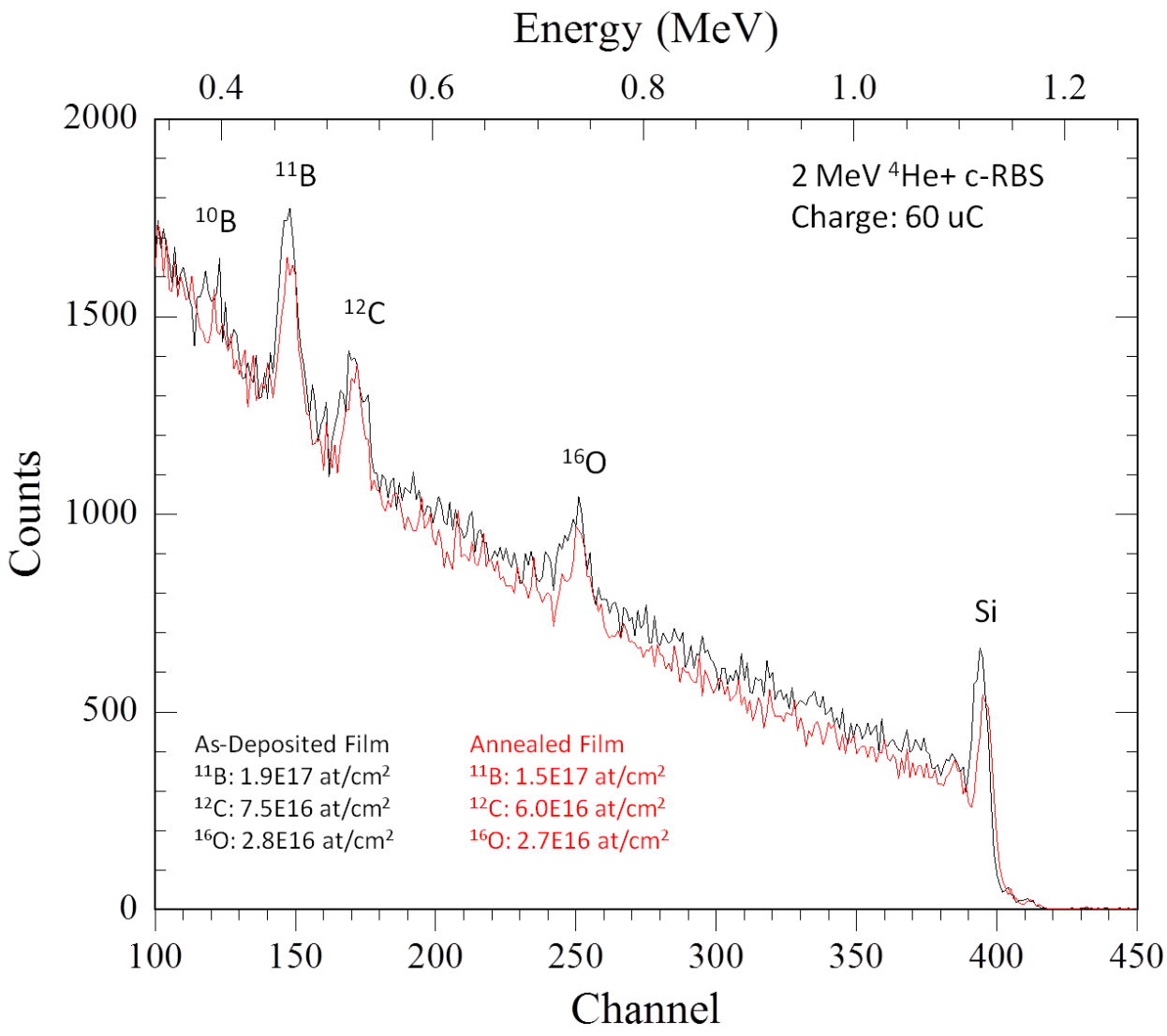

Figure 3. 2 RBS spectrum for as-deposited (black line) and post-annealed (red line) 50 nm boron carbide films on Si substrate. The incident energy of the alpha particles was 2 MeV. The spectrum was obtained at LANL.

Table 3. 2 Relative compositional ratio of the as-deposited and post-annealed 50 nm boron carbide film obtained from RBS results at LANL. These results probe the entire thickness of the film.

	B	C	O
As-deposited film	3.13	1.00	0.37
Post-annealed film	3.09	1.00	0.45

3.3 Elastic Recoil Detection Analysis (ERDA)

ERDA, another ion beam analysis technique, uses heavy ions to strike the target ions, and detects the recoil of the target atoms, rather than the energy of the scattered bombarding ions. The kinematic factor for the projectile particle (the fraction of the primary energy retained by the projectile particle after scattering) is the same as in RBS, shown in equation (3.1). For the recoil particles, the recoil kinematic factor (K_r) describes the fraction of energy transferred from incident projectile to recoil particle. Equation (3.3) shows the recoil kinematic factor calculated from energy and momentum conservation at a given recoil angle of φ [8], where 1 and 2 denote the primary and recoil particle, respectively.

$$K_r = \frac{4M_1M_2cos^2\varphi}{(M_1+M_2)^2} \tag{3.3}$$

The scattering and recoiling occur simultaneously and the M_2/M_1 ratio determines the relative weight of the kinematic factor for each. For example, if M_2/M_1 is higher than 1, the scattering kinematic factor is larger than the recoiling one.

ERDA is advantageous in the detection of light elements, with the relevant information being carried by the target nuclei themselves, not by the backscattering of the bombarding ions,

as in RBS [9]. Therefore, the compositional analysis of boron carbide, which consists of mostly light elements such as boron, carbon, and hydrogen, benefits greatly from ERDA. In conventional ERDA heavy primary ions are used and an absorber foil/detector combination is employed to stop the bombarding particles as shown in figure 3.1. Since the scattering in ERDA occurs in the forward direction, both scattered primary ions and recoil particles would enter the detector. The absorber foil stops the heavy primary particles while light energetic recoil particles can still reach the detector. The absorber foil/detector combination makes ERDA sensitive to light elements in a heavy matrix which is not the case for RBS. The results from ERDA experiments are obtained in terms of areal densities (atoms/cm^2) and concentration ratios (%) of the elements at a fixed areal density, just as in RBS.

ERDA were conducted at two different experimental set-ups 1) the same set-up as for our RBS experiments at LANL using 3 MeV alpha particles for the primary ion and 2) an ERDA set-up in Linköping University, Sweden, which uses iodine ions. The first one was performed for thin 50 nm boron carbide films on Si substrates to investigate the absolute concentration of hydrogen. The second set-up was for 1 μm thick boron carbide films on Si substrates to investigate all elements of the thick film sample as a function of depth.

Figure 3.3 shows the ERDA results for hydrogen in the thin as-deposited (black line) and post-annealed (red line) film from LANL. The hydrogen concentration was calculated based on a hydrogen standard (a 200 nm thick hydrogenated Si film on Si substrate) in which the hydrogen concentration was already known. The alpha particles scattered from the samples were completely stopped by an 18 μm Mylar absorber foil in front of the detector. About 34% of hydrogen is reduced by the post-annealing at 600 °C showing good agreement with previous infrared (IR) spectroscopy measurements [10] which shows a significant suppression of the

boron-hydrogen peak after annealing. The relative elemental ratio between the hydrogen from ERDA and the carbon from RBS is about 2.15 to 1 (H to C) for the as-deposited and 1.78 to 1 for the post-annealed. Therefore, if we assume that the elemental composition does not change with depth, the elemental composition is $B_{3.13}C_1H_{2.15}O_{0.37}$ for the as-deposited and $B_{3.09}C_1H_{1.78}O_{0.45}$ for the post-annealed films respectively, quite distinct from the elemental composition of the $B_{10}C_2H_{12}$ orthocarborane source molecule, showing a relatively higher concentration of C and a reduction in the concentration of hydrogen.

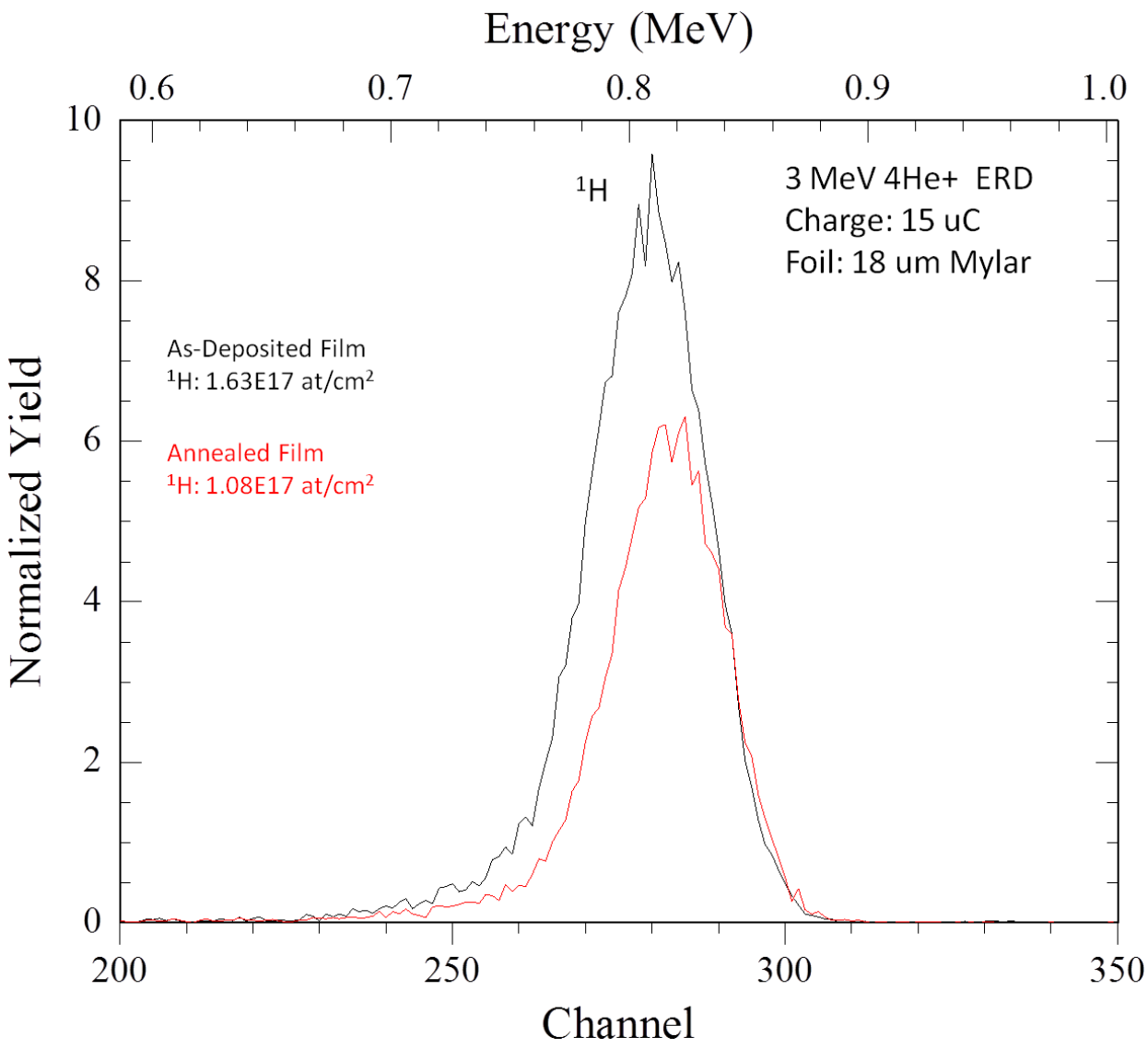

Figure 3. 3 ERDA spectrum for as-deposited (black line) and post-annealed (red line) 50 nm boron carbide film on Si substrate. The incident energy of the alpha particles was 3 MeV. The spectrum was obtained at LANL. (The X-axis indicates the energy of the recoiled particle. With a thicker absorber foil, the peak position would move to the left.)

The second experiment, time-of-flight ERDA, performed at Linköping University enables an elemental analysis as a function of areal density (or sampling depth) for thick 1μm boron carbide films, 20 times thicker than the thin films for the RBS/ERDA at LANL. These ERDA experiments utilize primary ions of 30-40 MeV iodine, which are stopped completely in the boron carbide film at an incident angle of 66 degree, thus eliminating the background signal from the Si substrate. Depth profiling was performed by sputtering of the thin film and the correlation between depth and energy was obtained by evaluating the stopping powers and the corresponding energy loss of the primary ion. Figure 3.4 shows the ERDA results as a function of areal density for as-deposited (a) and post-annealed at 600 °C (b) 1 μm boron carbide films on a Si substrate. In the case of the as-deposited film, the sample began delaminating during the experiment, which was therefore conducted only for about 2 minutes, resulting in fewer data points. (Note that the annealed film also delaminated about 1 year after the measurement. A possible reason for the delamination is that these two films were cut from 3 inch circular samples using a diamond cutter. Since the cut is not perfectly clean, the films start delaminating at the edges because there is a component of stress that can act more effectively at the edge, where cutting may have started interfacial cracking.)

As shown in figure 3.4, the elemental composition varies near the surface slightly for the as-deposited film and significantly changes for the post-annealed film. Both films show stoichiometries converging to constant elemental ratios as the depth increases. As seen from RBS, the boron carbide films are contaminated by oxides but the ERDA data show that the oxygen contamination is only on the top surface and disappears at an areal density of 1000×10^{15} atoms/cm^2 for the both films. Therefore, we infer that oxygen contamination arises from contact with air.

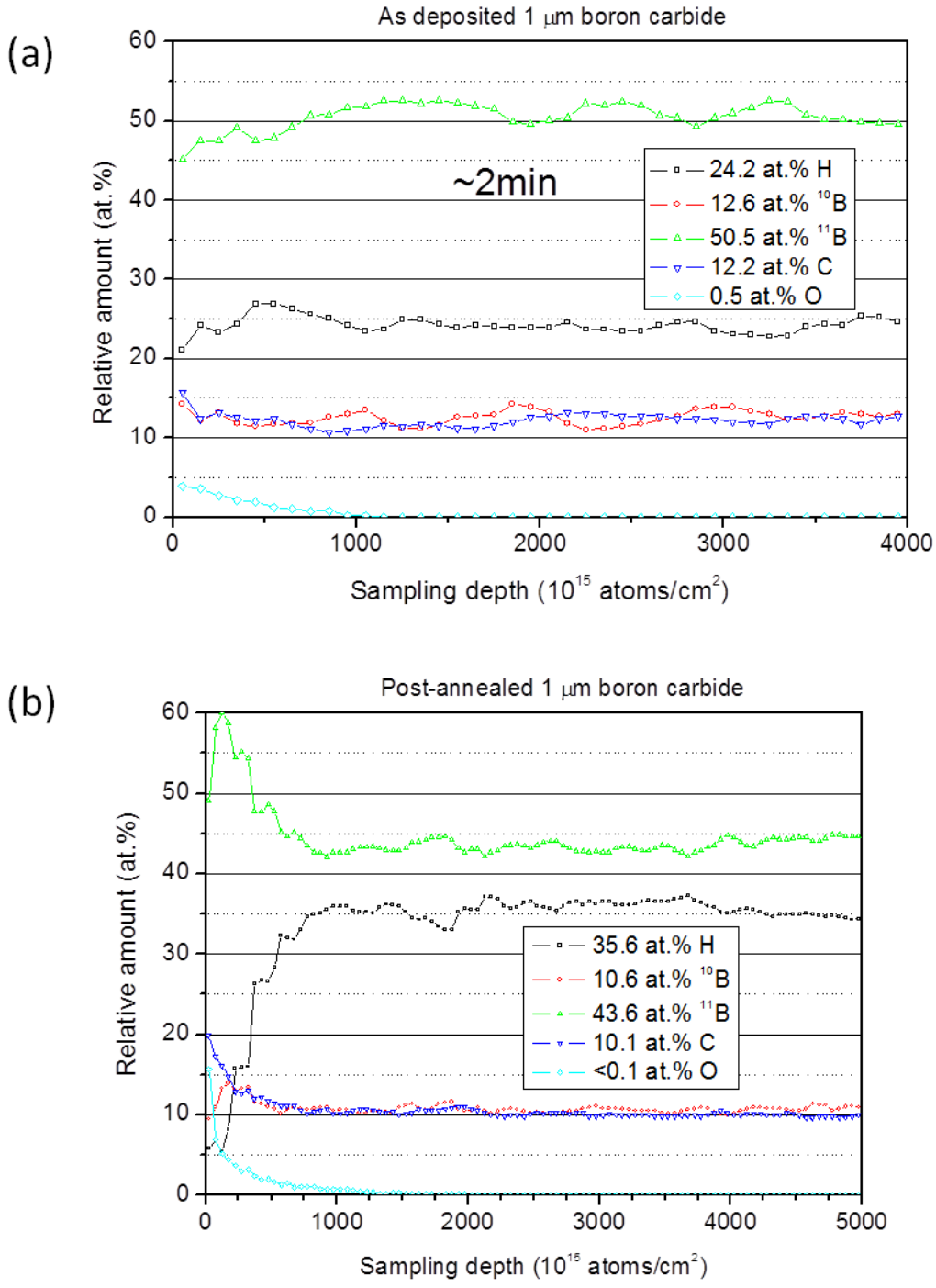

Figure 3. 4 Relative amount (at. %) for each element is shown as a function of sampling depth in units of 10^{15} atoms/cm^2 for the as-deposited (a) and post-annealed (b) boron carbide films obtained from ERDA.

The sampling depth in terms of the areal density can be converted to a depth in nanometers by the following equation where t is the depth, x is the areal atomic density (atoms/cm^2), M is the relative mass (g/mol) (the relative mass is the material mass and depends on the elemental composition), ρ is the gravimetric density (g/cc) and N_A is Avogadro's number (atoms/mol) [11].

$$t = \frac{x \cdot M}{\rho \cdot N_A} \tag{3.4}$$

The corresponding depth profiles are shown in figure 3.5. The step size for the depth is ~6.6 nm and ~3.3 nm with a total scan depth of 215 nm and 345 nm for the as-deposited (a) and post-annealed (b) film, respectively.

The oxygen contamination range is the same for both films, arising only from the top 50 nm of the film. There is a negligible amount of oxygen within the bulk of the film. The hydrogen surface concentration (~ 50 nm from the surface) drops rapidly after the post-annealing treatment. However, the post-annealed film contains a higher hydrogen concentration at larger depths as compared with the as-deposited one. Consequently, we infer that the hydrogen diffuses into the film due to the post-annealing treatment. We speculate that previous data on the IR spectrum that revealed a much weaker boron-hydrogen bond [10] on annealing is because IR spectroscopy is surface sensitive [12].

The elemental compositions are constant beyond a certain depth from the surface and the corresponding average atomic concentrations for each element are tabulated in the boxes in figure 3.5. As with the thinner films, we show the elemental stoichiometry for the thick films (where the carbon concentration is assumed to be unity) in table 3.3. For these thick boron carbide films, the boron to carbon ratio is about 5 to 1, the same as for the source molecule. Post-annealing does not change the relative ratio between the boron and carbon concentrations.

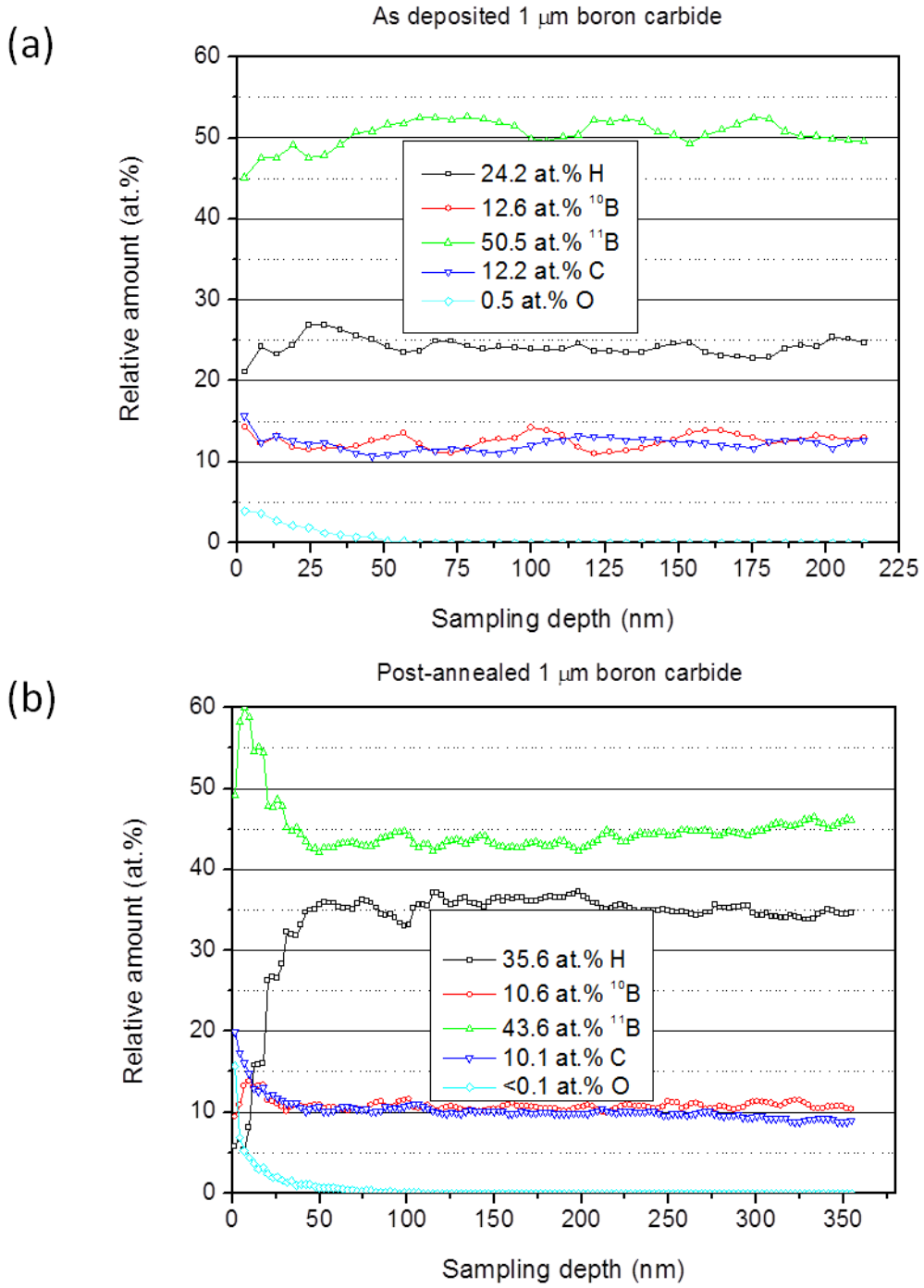

Figure 3. 5 Relative amount (at. %) for each element is shown as a function of sampling depth in nm for the as-deposited (a) and post-annealed (b) boron carbide films obtained from ERDA.

Table 3. 3 Relative compositional ratios of the as-deposited and the post-annealed 1 μm boron carbide films obtained from ERDA.

	B	C	H	O
As-deposited film	5.17	1.00	1.98	0.04
Post-annealed film	5.37	1.00	3.53	< 0.01

ERDA measurements allowed us to define the composition of these films as $B_5C_1H_2$, which we used in our simulation and calculations for neutron detection efficiency. The RBS results on the thin (50 nm) boron carbide films show a compositional ratio of about 3 to 1 for the boron to carbon concentrations. In order to resolve the discrepancy between the RBS and ERDA measurements, we plot the relative concentrations of boron and hydrogen with respect to carbon (a and c), and carbon and hydrogen with respect to boron (b and d) in figure 3.6 for both thick films as a function of scan depth. (a) and (c) indicate that the boron/carbon ratio drops to 3.8 and 3.0 at the top surface. With increasing depth, the boron to carbon ratio saturates at 5 to 1. Since the RBS experiments did not perform a depth profile, the overall elemental compositions for the thin films was dominated by the surface signal and the relatively low boron concentration for the thin boron carbide films in table 3.2 is a surface effect.

IBA is an excellent technique for investigating the exact atomic composition, but cannot give us information regarding the chemical structure. Here, the IBA results for the thin and thick boron carbide films indicate compositional changes as a function of film depth and thickness. Our results are consistent with preservation of the icosahedral cage of the source molecule in the deposited films but to confirm this we performed both IR and Raman spectroscopy, as detailed in Chapter 4.

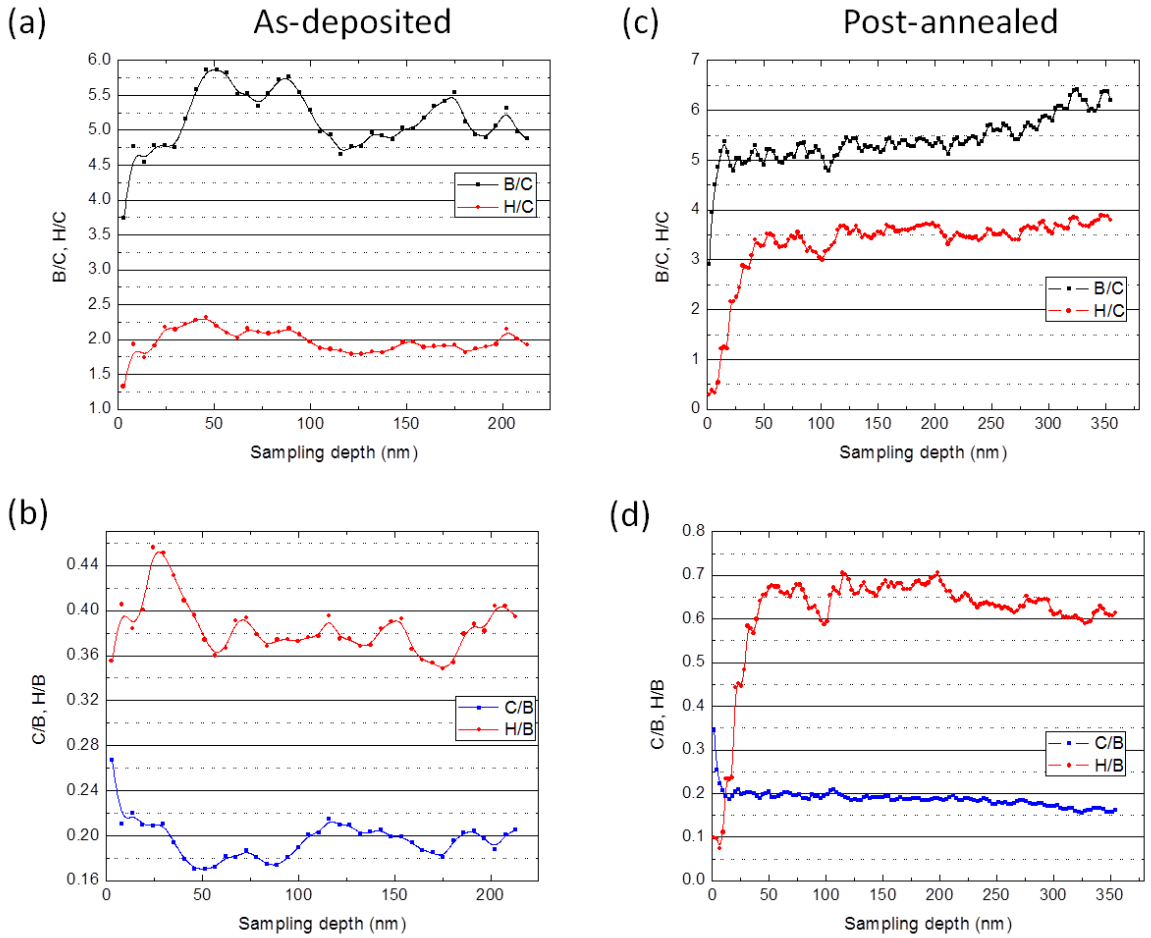

Figure 3. 6 Relative concentration of each element with respect to carbon (a and c) and with respect to boron (b and d) as a function of film depth in nm obtained from ERDA. Left-hand side shows the plots for as-deposited and right-hand side for post-annealed thick boron carbide films.

REFERECES

1. Zhang, D., et al., *The chemical composition of as-grown and surface treated amorphous boron carbon thin films by means of NEXAFS and XPS.* Surface Science, 2000. **461**: p. 16-22.
2. Lee, S., et al., *Characterization of boron carbide thin films fabricated by plasma enhanced chemical vapor deposition from boranes.* Journal of Applied Physics, 1992. **72**(10): p. 4925-4933.
3. *Evans Analytic Group, www.eaglabs.com.*
4. *Ion Beam Materials Laboratory.* 2006: p. LALP-06-036.
5. Ziegler, J.F., J.P. Biersack, and U. Littmark, *The stopping and range of ions in solids*. 1985: New York: Pergamon.
6. *James Ziegler - SRIM & TRIM, www.srim.org.*
7. Hong, N., et al., *Ni doping of semiconducting boron carbide.* Journal of Applied Physics, 2010. **107**(2): p. 024513.
8. Feldman, L.C. and J.W. Mayer, *Fundamentals of Surface and Thin Film Analysis*. 1986: Amsterdam: North-Holland.
9. Bik, W.M.A. and F.H.P.M. Habraken, *Elastic recoil detection.* Reports on Progress in Physics, 1993. **56**(7): p. 859.
10. Billa, R.B., et al., *Annealing effects on the optical properties of semiconducting boron carbide.* Journal of Applied Physics, 2009. **106**(3): p. 033515.
11. Höglund, C., *Growth and Phase Stability Studies of Epitaxial Sc-Al-N and Ti-Al-N Thin Films*, in *Ph.D. dissertation, Linköping University Institute of Technology*. 2010.
12. Walls, J.M. and R. Smith, *Surface science techniques*. 1994: Pergamon, 1st edition.

Chapter 4 Vibrational and Rotational Spectra of PECVD Grown Boron Carbide

Part of the work reported in this chapter on IR and Raman spectroscopy was performed in collaboration with Orhan Kizilkaya of Center for Advanced Microstructures and Devices (CAMD), Louisiana State University, Baton Rouge, Louisiana, U.S.A. and Wei Xiong of Laser-Assisted Nano Engineering Lab., Department of Electrical Engineering, University of Nebraska-Lincoln, Lincoln, NE, U.S.A.

4.1 Introduction

Covalently bonded boron rich carbon compounds have drawn attention for their use as armor ceramics due to their ultra hardness against high-pressure impact [1-4]. B_4C (or $B_{12}C_3$) is generally accepted to be the most stable crystal structure in this family, but a wide range of stable compositions (~8-20 at. % C) exists [5, 6] with different distributions of boron and carbon atoms. Approaches to investigation of the crystal structure of the various boron carbides have been based on the composition B_4C [7-10], with changes in the stoichiometry being modeled by various disorder (mixing) mechanisms [11-14]. Attempts to interpret the diffraction data of the crystal structure of B_4C to assign elemental placements of the boron and carbon atoms remained elusive because the x-ray form factors of B and C are nearly equal, and because the neutron scattering lengths for ^{11}B and ^{12}C are so similar [15]. In addition, neutron diffraction experiments have to contend with the high absorption of neutrons by the ^{10}B isotope, which occurs at a 19% fraction in naturally occurring boron.

In the investigation of semiconducting PECVD grown boron carbide, the structure plays an important role because it enables identification of the material with the best semiconducting

properties. The simultaneous presence of multiple polytypes results in defects, states in the gap, lower mobilities and trapped charge. Knowledge of the structure enables us to vary growth parameters to correlate improved semiconducting properties with structural changes and hence to make the material with the desired properties. X-ray diffraction (XRD) measurements of the PECVD grown boron carbides ($B_5C_1H_2$ and Ni-doped $B_5C_1H_2$, discussed in Chapter 5) did not enable us to predict the constituents of the icosahedral cages and the linear chains which connect the icosahedral cages in the rhombohedral crystal structure generally assigned to the boron carbides. In fact, both XRD and electron diffraction measurements show no clear indication of long range order. Instead in this chapter we will consider the interaction of electromagnetic radiation with molecular vibrations and rotations using two complimentary techniques, infrared (IR) spectroscopy and Raman scattering, to investigate the molecular structure of the PECVD grown boron carbide films.

Lazzari *et al.* [7] predicted the atomic structure of icosahedral B_4C by comparing existing IR absorption and Raman measurements with the results of accurate *ab initio* lattice-dynamical calculations. They take into account three ordered configurations of B_4C 1) the *chain* configuration: B_{12} icosahedra + C-C-C intericosahedral chains 2) the *polar* configuration: $B_{11}C$ icosahedra wherein a C is placed in one of the polar sites + C-B-C chains 3) the *equatorial* configuration: $B_{11}C$ icosahedra wherein a C is placed in one of the equatorial sites + C-B-C chains. Figure 4.1 shows the atomic structure of B_4C and descriptions of each site. Their theoretical model showed that the lowest energy was for the *polar* configuration of B_4C. Here we discuss our IR and Raman measurements and fingerprint the vibrational modes from existing data. A more in depth analysis will require extensive theoretical computations.

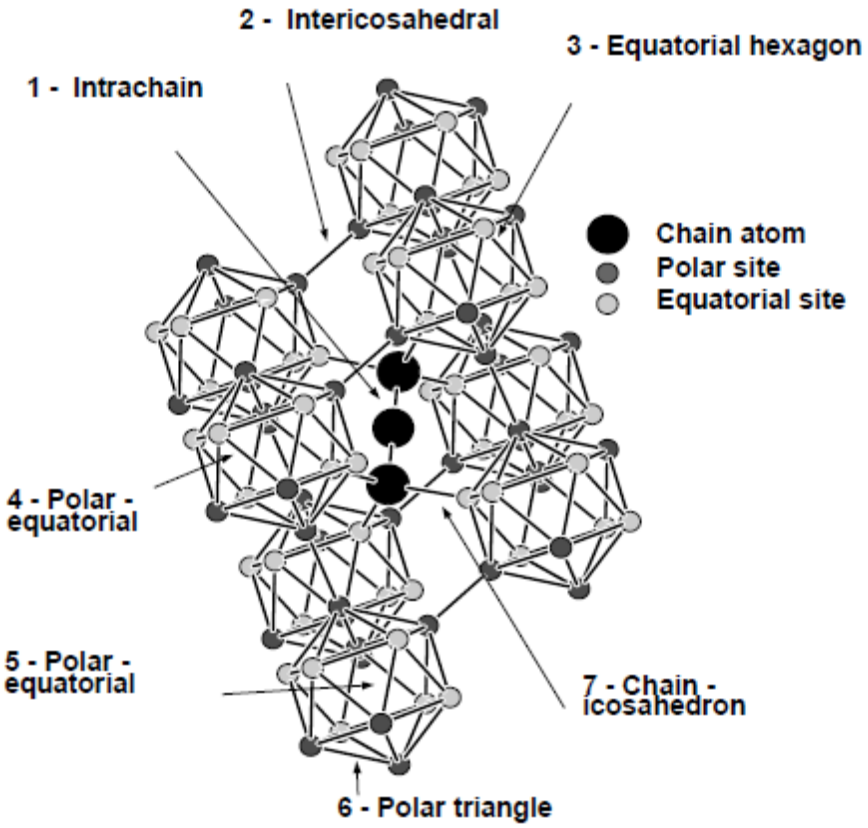

Figure 4. 1 Atomic structure of B_4C. Depending on the configuration, each site may contain either B or C atoms. Figure adapted from Ref. [7].

Figure 4.2 shows the icosahedral cage of the orthocarborane precursor ($C_2B_{10}H_{12}$) used in PECVD growth of boron carbide films. The boron and carbon atoms are on the vertices of the icosahedra, with two nearest neighbor carbon atoms. Hydrogen atoms are bonded to the B and C atoms on all twelve vertices. The ERDA results in Chapter 3 show an elemental ratio of $B_5C_1H_2$ for the as-deposited thick boron carbide film. If we assume that the icosahedral cage remains intact during deposition, we might guess that 8 hydrogen bonds to either boron or carbon are broken during the PECVD process. Because neither XRD nor TEM have shown the existence of long range order in the thin films, this elemental composition is at best an average over the film.

From the results of IR and Raman, we investigated the major chemical bonds which exist both 1) within the icosahedral cage and 2) outside the icosahedral cages, for example in chains that connect the icosahedrons.

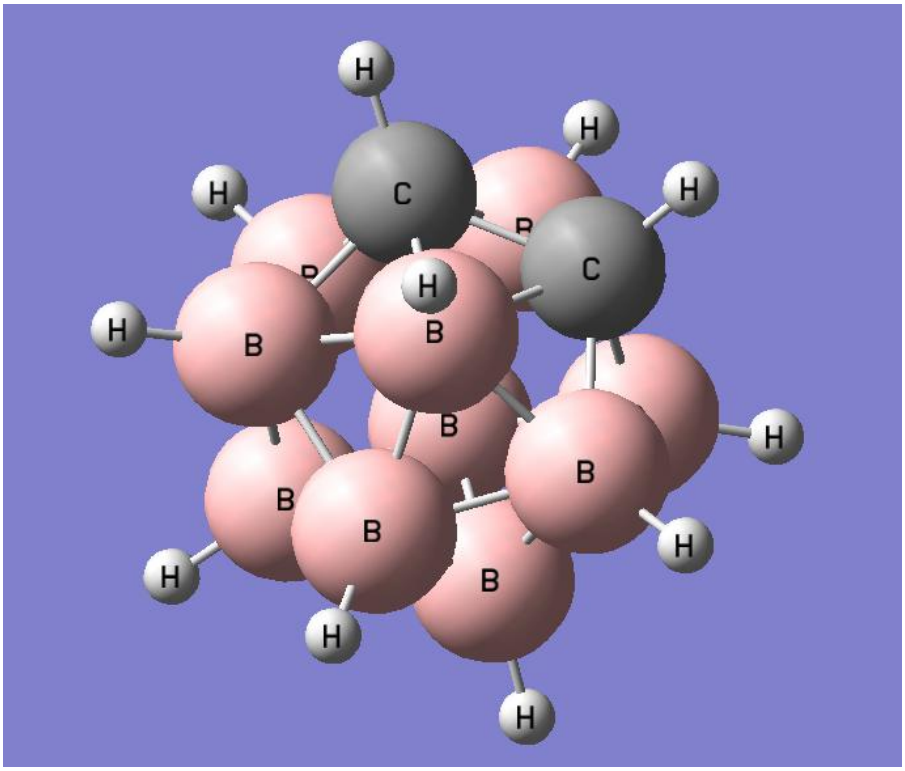

Figure 4. 2 Orthocarborane molecular structure. This figure is obtained from a Gaussian 03 simulation.

4.2 Experimental details

Fourier transform infrared (FT-IR) spectroscopy was performed using the IR microspectroscopy beamline at the Center for Advanced Microstructures & Devices (CAMD) [16]. The IR synchrotron radiation at CAMD [17] measured a ~1 μm thick undoped and a Ni-doped $B_5C_1H_2$ film on Si wafers grown using PECVD with a substrate temperature of 330 ℃

[18]. The Ni-doped $B_5C_1H_2$ was deposited using 1 SCCM of Ar carrier gas through the orthocarborane vial and 9 SCCM of Ar carrier gas through the nickelocene vial leading to a heavily Ni doped sample, designated as Ni(9)-$B_5C_1H_2$ in Chapter 5. The orthocarborane source compound was also examined by FT-IR using the globar source at CAMD [17]. The source molecule was mixed with KBr powder and pressed to make a KBr disc. The Thermo Nicolet Nexus 670 FT-IR spectrometer is used for the both IR beam sources, in reflection mode for the boron carbide film samples and in transmission mode for the orthocarborane disc sample.

Raman spectroscopy of an ~1 μm thick undoped $B_5C_1H_2$ film on Si and an ~1 μm Ni-doped $B_5C_1H_2$ film on Si was conducted using a Renishaw Raman spectrometer. The films were deposited under the same conditions as the films used for the IR measurements, albeit in separate deposition runs. A diode laser with a wavelength of 785 nm and a power of 12.5 mW was used as the excitation source (1.58 eV). The beam was focused to a spot diameter of approximately 5 μm. Two independent scans, one was centered at 400 cm^{-1} and the other centered at 980 cm^{-1}, were performed in static-mode to cover an extensive range from low to high frequencies. One Raman mode was selected to map a wide area of 90×70 μm^2 to investigate the homogeneity of a particular chemical bond in the undoped $B_5C_1H_2$ film.

4.3 Results and discussion

We first simulated the structure of orthocarborane ($C_2B_{10}H_{12}$) using an electronic structure modeling tool (Gaussian 03[19]) to understand the chemical structure and possible vibration modes. Table 4.1 shows a summary of the calculation conditions including the calculation method and the basis set. The distance matrix of $C_2B_{10}H_{12}$ obtained from the calculation (shown in table 4.2) is compared with the result of XRD measurements for

orthocarborane powder in figure 4.3. Since there are 24 atomic sites in the orthocarborane molecule, the distance matrix shows 552 possible distances between each atom. Because x-rays are nearly insensitive to hydrogen, this is reduced to 132 possible atom to atom distances that we expect to see in x-rays. Table 4.3 shows the various atom to atom distances for H, B, C. The B-B distance varies from 1.78 Å to 2.9 Å, B-C from 1.70 Å to 3.23 Å, and the C-C distance is 1.63 Å. The XRD results show 6 separate peaks corresponding to distances that range from 1.9 Å to 2.98 Å. Although we cannot definitively assign the XRD peaks to particular atom to atom distances obtained from Gaussian 03, the range of atom to atom distances is comparable. The lack of a discernible peak at or close to the C-C distance may be attributed to the low expected amplitude of this peak.

Table 4. 1 A summary of the Gaussian 03 calculation conditions used to obtain the stationary molecular geometry and the vibrating modes.

Calculation type	Freq	A calculation of the vibrational frequencies of the molecule.
Calculation method	RB3LYP	A restricted calculation of a closed shell configuration
Basis Set	6-31G(d,p)	A polarized basis set which adds p functions to hydrogen atoms in addition to the d functions on heavy atoms.

Table 4. 2 Distance matrix of the icosahedra shown in figure 4.2 simulated by Gaussian 03 with the calculation conditions in table 4.1. Distances are in Å .

		1	**2**	**3**	**4**	**5**
1	B	0				
2	B	1.784664	0			
3	B	2.891901	1.779832	0		
4	B	1.777649	1.777645	2.877888	0	
5	B	2.880545	2.880334	2.877743	1.783161	0
6	B	3.388815	2.880663	1.779784	2.880355	1.777463
7	B	2.89133	1.780582	1.764748	1.792546	1.792533
8	B	1.780954	2.891336	3.402642	1.792361	1.792493
9	H	4.562346	3.940884	2.554752	3.993296	2.682914
10	H	3.952971	2.602613	2.569881	2.635754	2.635552
11	H	3.94492	3.94467	3.930072	2.622771	1.1852
12	H	2.59189	2.591662	3.93011	1.185202	2.622824
13	H	2.602658	3.952935	4.587224	2.635718	2.635961
14	H	2.585116	1.182684	2.554552	2.683289	3.993297
15	H	1.18267	2.58522	3.891948	2.682884	3.993289
16	H	3.907331	2.634696	1.180523	3.986359	3.986173
17	H	2.634497	3.907196	3.869558	3.986098	3.986286
18	C	1.69855	1.69866	1.719468	2.739229	3.225172
19	H	2.44693	2.447127	2.392042	3.730999	4.303443
20	H	3.94087	4.562318	3.891832	3.993251	2.683222
21	H	3.663222	3.663183	2.391929	4.303452	3.730888
22	B	2.880814	3.388774	2.891908	2.880396	1.777716
23	C	2.750985	2.750976	1.719428	3.225171	2.739184
24	B	1.779645	2.891816	2.911123	2.877583	2.877776
		6	**7**	**8**	**9**	**10**
6	B	0				
7	B	1.780779	0			
8	B	2.891286	2.907366	0		
9	H	1.182684	2.668734	3.965926	0	
10	H	2.602531	1.184796	3.977887	3.116876	0
11	H	2.591607	2.620001	2.619986	3.128002	3.06891
12	H	3.944639	2.619833	2.620047	4.9845	3.06894
13	H	3.952965	3.978142	1.184803	4.939605	4.960107
14	H	3.940733	2.668409	3.966135	4.905548	3.116851
15	H	4.562407	3.965977	2.668603	5.729988	4.939616
16	H	2.634602	2.701867	4.567689	3.000833	3.150509
17	H	3.907374	4.567612	2.701954	4.77673	5.750086
18	C	2.751009	2.74803	2.748102	3.760837	3.811567

19	H	3.663201	3.707566	3.707626	4.542726	4.676894
20	H	2.585403	3.966306	2.66846	2.960984	4.939814
21	H	2.447036	3.707581	3.707635	2.82513	4.676762
22	B	1.784803	2.891507	1.780737	2.585092	3.952999
23	C	1.698703	2.748108	2.748067	2.48389	3.811546
24	B	2.892014	3.402611	1.764653	3.891811	4.587197
		11	**12**	**13**	**14**	**15**
11	H	0				
12	H	3.070034	0			
13	H	3.069554	3.06951	0		
14	H	4.98458	3.128337	4.939769	0	
15	H	4.984531	3.128017	3.116525	2.960988	0
16	H	4.9625	4.962572	5.750136	3.000613	4.777047
17	H	4.962712	4.962606	3.15011	4.776542	3.000889
18	C	4.410246	3.802643	3.811368	2.483776	2.484163
19	H	5.487812	4.711411	4.676576	2.825162	2.825621
20	H	3.128444	4.984644	3.11656	5.729851	4.905577
21	H	4.711303	5.487822	4.676661	4.542531	4.543064
22	B	2.5919	3.94485	2.602563	4.562288	3.94095
23	C	3.802621	4.410245	3.811381	3.760668	3.761033
24	B	3.930146	3.930025	2.569386	3.891613	2.554716
		16	**17**	**18**	**19**	**20**
16	H	0				
17	H	4.665085	0			
18	C	2.497604	2.49737	0		
19	H	2.732763	2.7324	1.082357	0	
20	H	4.776851	3.000662	3.760754	4.542565	0
21	H	2.732575	2.732768	2.316176	2.579533	2.825243
22	B	3.907319	2.634591	2.750945	3.663084	1.182675
23	C	2.497536	2.497495	1.625472	2.316082	2.483911
24	B	3.869764	1.180528	1.719436	2.391987	2.554645
		21	**22**	**23**	**24**	**25**
21	H	0				
22	B	2.446957	0			
23	C	1.082354	1.69858	0		
24	B	2.392297	1.779798	1.719593	0	

Based on the stationary molecular geometry calculated with Gaussian 03, we obtained the vibration frequencies for the orthocarborane icosahedron and compared the simulation results with the IR spectrum for the orthocarborane condensed phase measured by the manufacturer (Sigma-Aldrich [20]). As can be seen from figure 4.4, the vibrational modes arise in two regions 1) a low frequency range from 500 cm^{-1}– 1500 cm^{-1} and 2) a high frequency range from 2400 cm^{-1}-3500 cm^{-1}. Although the two spectra do not match exactly, the regions of the peaks show fairly good agreement. According to the Gaussian 03 results, the peaks in the low frequency range are due to the various vibrations of B-B, B-C bonds, the peaks at ~2700 cm^{-1} are due to B-H bonds, and the peak at 3250 cm^{-1} is due to C-H bonds.

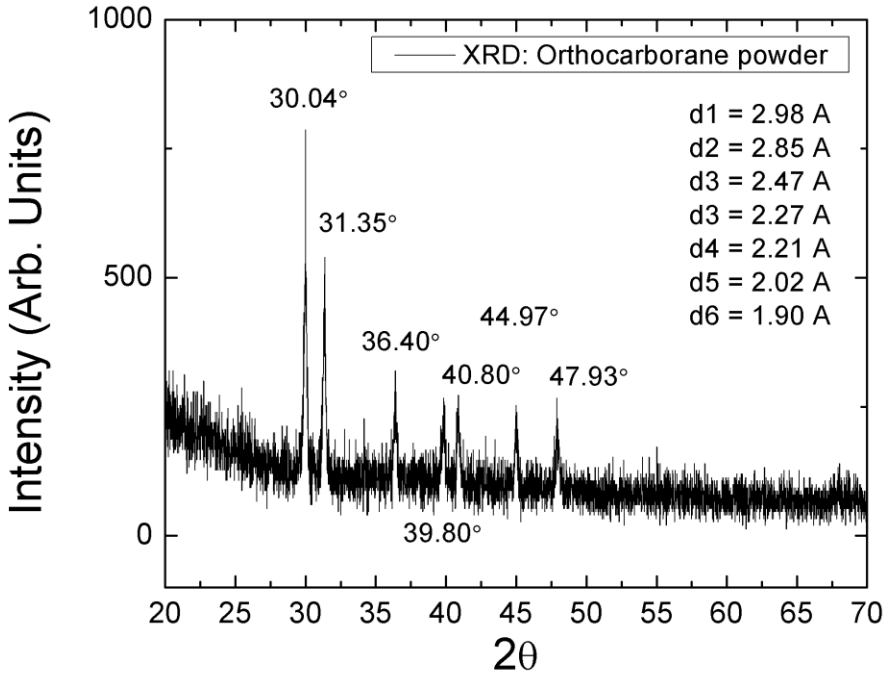

Figure 4. 3 XRD results obtained from orthocarborane powder showing 6 diffraction peaks. d1-d6 indicate the atomic distance for each diffraction peak.

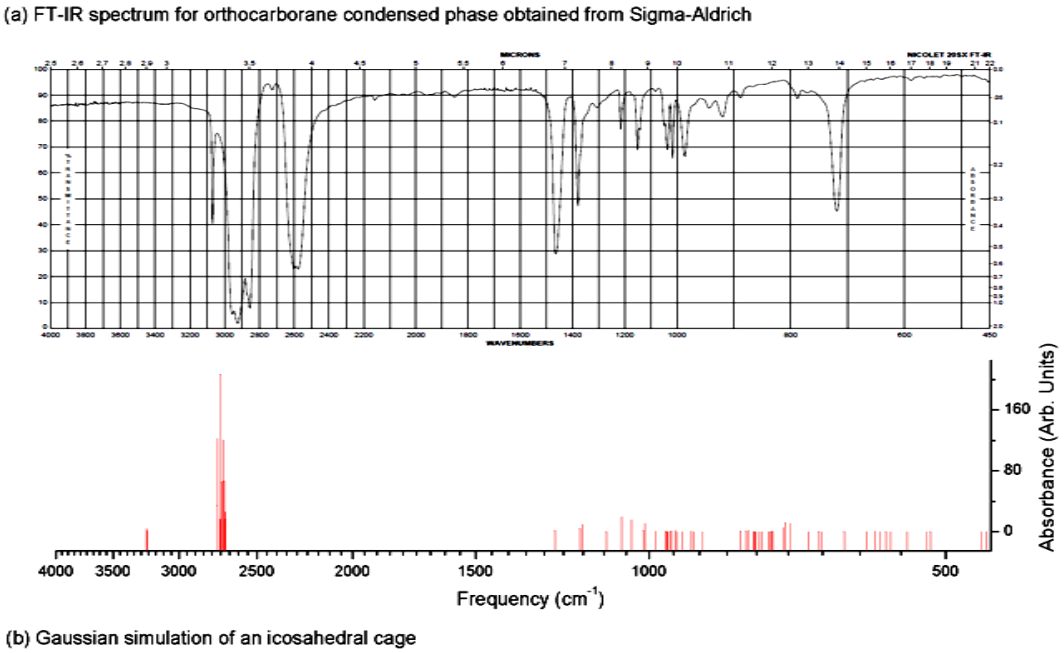

Figure 4. 4 (a) FT-IR spectrum for the orthocarborane condensed phase obtained from Sigma-Aldrich, (b) Vibrational modes for an orthocarborane icosahedron calculated by Gaussian 03.

Similar to figure 4.4, the IR spectrum of the orthocarborane KBr disc serves as an indicator of the IR active modes for the icosahedral cage of the boron carbide films. Figure 4.5 (c) shows the FT-IR spectrum of the orthocarborane and (a) the undoped $B_5C_1H_2$ film on Si and (b) the Ni-doped $B_5C_1H_2$ film on Si. The interference fringes in figure 4.5 (a) and (b) indicate identical thicknesses of the two films. The strongest two peaks in the high frequency range for orthocarborane are the B-H stretch mode (2590 cm^{-1}) and C-H stretch mode (3070 cm^{-1}) [21-23]. The width of the B-H stretch mode arises from the various resonant frequencies of each B-H bond at different sites of the slightly distorted icosahedron. The two films, undoped and Ni-doped $B_5C_1H_2$ films show B-H stretch modes at the same frequency (2590 cm^{-1}) whereas the C-H frequency is absent for both. Hence, hydrogen appears to be preferentially bonded to B after deposition. The numerous low frequency peaks in the orthocarborane IR spectrum (1300 cm^{-1}–

700 cm^{-1}) are due to the icosahedral cage vibrations of the B-B bonds, the B-C bonds or the "breathing" mode [23, 24]. The spectrum for the undoped film in figure 4.5 (a) shows two distinct peaks at 770 cm^{-1} and 1060 cm^{-1} within this frequency range, but these peaks are absent in the Ni doped film. The vibration peaks near the frequency of 770 cm^{-1} appear in many boron rich carbon films including amorphous/crystalline pure boron films, arising from the B-B bonds in the icosahedra [22, 25, 26]. The other vibration peak at 1060 cm^{-1} is assigned to B-C vibrations within the icosahedra [22, 25, 26]. Therefore, the FT-IR results in figure 4.3 indicate that the icosahedral structure is preserved in the undoped $B_5C_1H_2$ film, but is either completely or partially destroyed in the Ni-doped $B_5C_1H_2$ film leading to the disappearance or attenuation of the IR absorption mode. The two peaks at 1524 cm^{-1}, 1640 cm^{-1} (a) and 1545 cm^{-1}, 1660 cm^{-1} (b) are related to the presence of carbon contaminants [22, 25] and a similar two peak feature is assigned to the presence of CO_2 as a result of carbon contamination on the surface oxide layer [27]. The expected IR absorption frequency of B-C bonds associated with the intericosahedral C-B-C chains lies near 1500 cm^{-1} [13, 26, 28, 29] which cannot be distinguished from the carbon peaks. Hence from the IR data, we deduce that the icosahedral structure remains intact for the undoped boron carbide film, is greatly diminished in the highly doped boron carbide film and that the hydrogen is preferentially bonded to B rather than C. There is no evidence for interiscosahedral bonding because the expected chain absorption lines are overshadowed by the peaks from carbon contamination.

Figure 4.6 shows the Raman spectra, after background subtraction, for the undoped and Ni-doped $B_5C_1H_2$ films on Si substrates. The low frequency range from 200 cm^{-1}-800 cm^{-1} is displayed on the left and the higher frequency range from 700 cm^{-1}-1200 cm^{-1} is on the right. The negative intensity shown in (c) is due to the background subtraction. The lowest frequency

Raman peak that is visible is at 302 cm^{-1}. Theoretical predictions [28, 30] and previous experiments [31-33] on boron rich carbon compounds reveal two peaks at 270 cm^{-1} and 320 cm^{-1} near the peak at 302 cm^{-1}. These peaks are attributed to bond bending between the three-chain atoms and equatorial atoms in the icosahedra due to chain rotation and icosahedra wagging [31, 32]. The two Raman modes are separately assigned to either the C-B-B or the C-B-C chain [31] since the vibration mode is highly dependent on the specific chain end (B or C) and the equatorial atom. The existence of only one peak in this range for the PECVD grown boron carbide films reveals the existence of one type of chain configuration. This is the first evidence that PECVD grown boron carbide film might contain center chains. However Raman spectra reveal local chemical bonds rather than long-range order and so the crystal structure of the PECVD grown boron carbide films remains ambiguous. The other three peaks (435 cm^{-1}, 620 cm^{-1}, and 670 cm^{-1}) in figure 4.4 (a) and (c) have not been identified yet due to the lack of fingerprints at those frequencies for boron carbon compounds. Figure 4.6 (b) and (d) show the Raman spectra in the high frequency range. The peaks in this range are related to the icosahedral cages, including hydrogen bonds. The first weak peak at 820 cm^{-1} is assigned to B-B bonds but it is not clear whether the bonds are intraicosahedral or intericosahedral [32]. The Raman spectrum of orthocarborane shows multiple peaks for the B-B stretching mode of icosahedrons at this position [23], indicating that our peak at 820 cm^{-1} might be due to intraicosahedral B-B bonds. The two peaks at 940 cm^{-1} and 981 cm^{-1} are related to stretching and rotating modes of the C-B-C chains [32, 34]. The weak and broad peak at the highest frequency at 1022 cm^{-1} is assigned to a breathing mode of the icosahedrons [32, 34]. Previous IR experiments have reported a significant enhancement of this mode for high temperature vacuum annealed PECVD grown boron carbide films [35] perhaps due to increased crystallization.

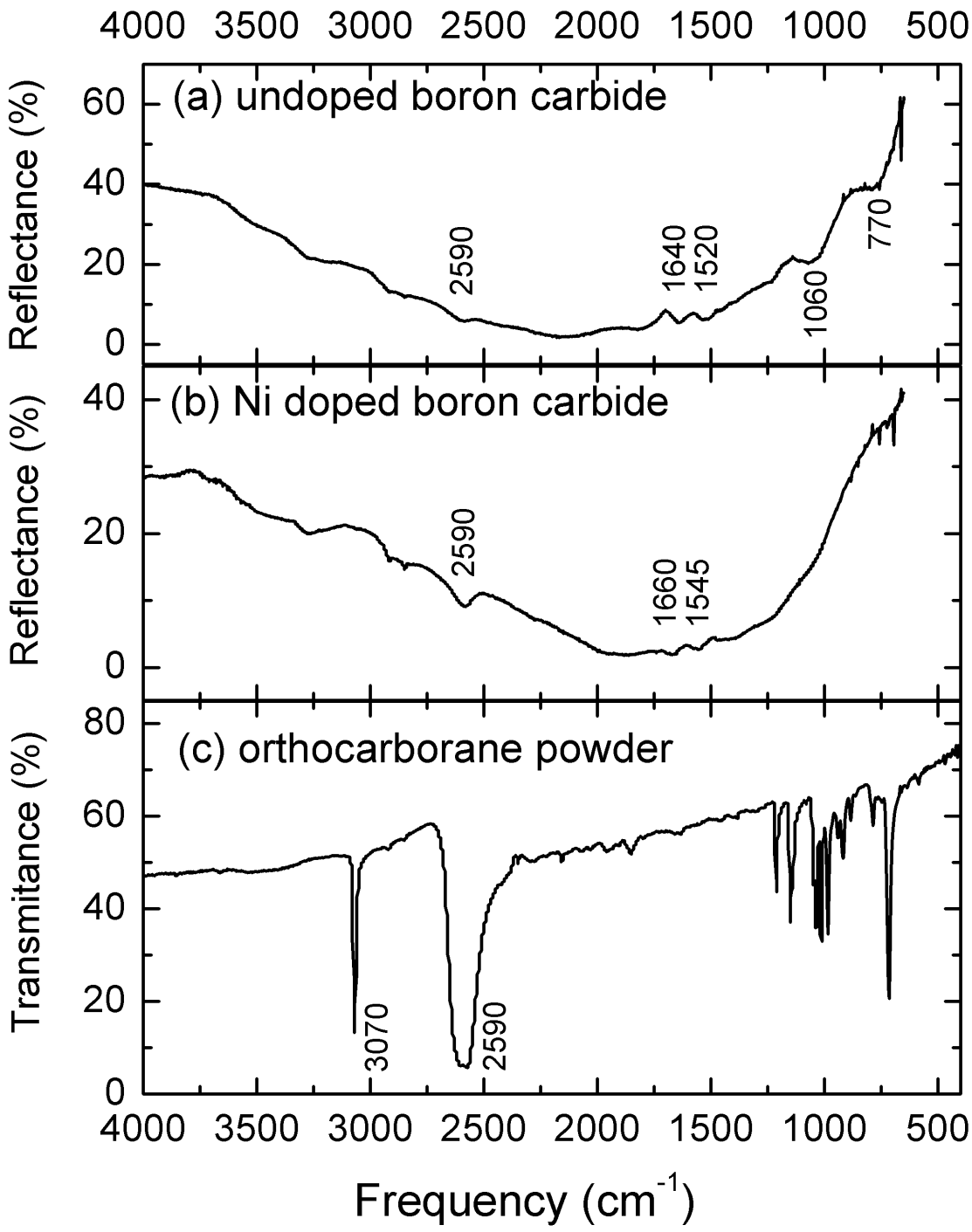

Figure 4. 5 FT-IR spectra for undoped $B_5C_1H_2$ on Si (a) Ni-doped $B_5C_1H_2$ on Si and orthocarborane powder (c).

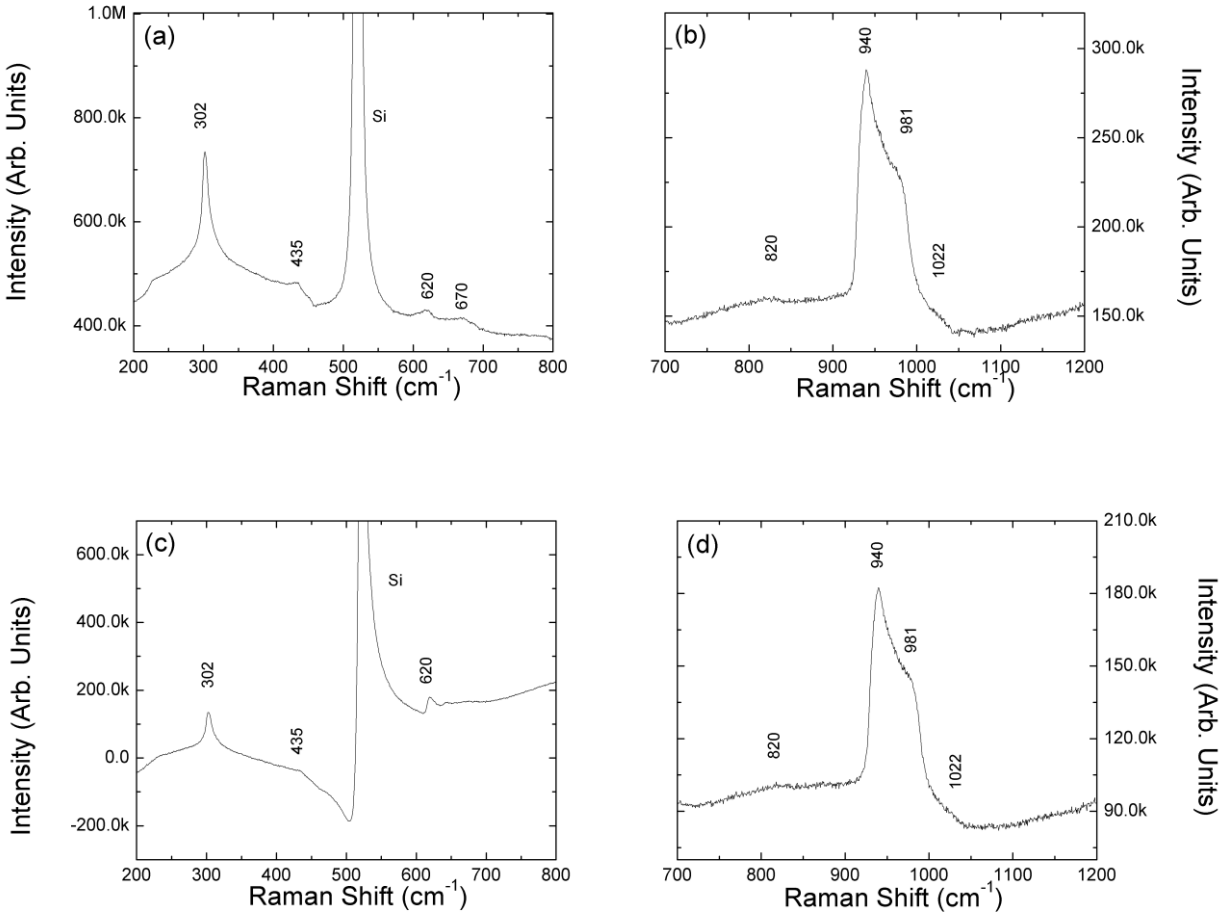

Figure 4. 6 Raman spectra for the low frequency range 200 cm^{-1} to 800 cm^{-1} on the left and for the high frequency range 700 cm^{-1} to 1200 cm^{-1} on the right. (a) and (b) are the spectra for the undoped $B_5C_1H_2$ film on a Si substrate, and (c) and (d) are for the Ni-doped $B_5C_1H_2$ film on a Si substrate.

To investigate the homogeneity of the undoped $B_5C_1H_2$ film, we performed a mapping of the peak area of the 302 cm^{-1} Raman mode, which is assigned to the chain to equatorial atom bond, with >500 scans over an area of 90×70 μm^2, with a resolution defined by the 5 μm area of the beam. The optical image of the unscanned area shows that the film surface does not have any large scale surface contaminants or scratches. The inset in figure 4.7 shows the scale of the color brightness. The lowest limit (the darkest color) is for a peak area of 121500 (Arb. Units),

and the highest limit (the brightest color) is for a peak area of 147200 (Arb. Units). The red curve in the inset shows the distribution of the peak area over the entire scanned area. The scanned image indicates that the maximum variation of the chemical homogeneity of the film is 17.5% within the scanned area with a resolution of 5 μm.

Both IR and Raman spectra for the PECVD deposited undoped and Ni-doped $B_5C_1H_2$ films show the presence of icosahedral bonds. This is the first evidence that the icosahedral cages in the thin films remain intact while the hydrogen bonds are greatly reduced. In addition, the Raman spectra showed the first evidence of intericosahedral chains, which may be evidence of the formation of nanoscale crystals. However, as indicated by the areal mapping of a particular Raman mode, there are large-scale inhomogeneities within the film, which will complicate the interpretation of diffraction data.

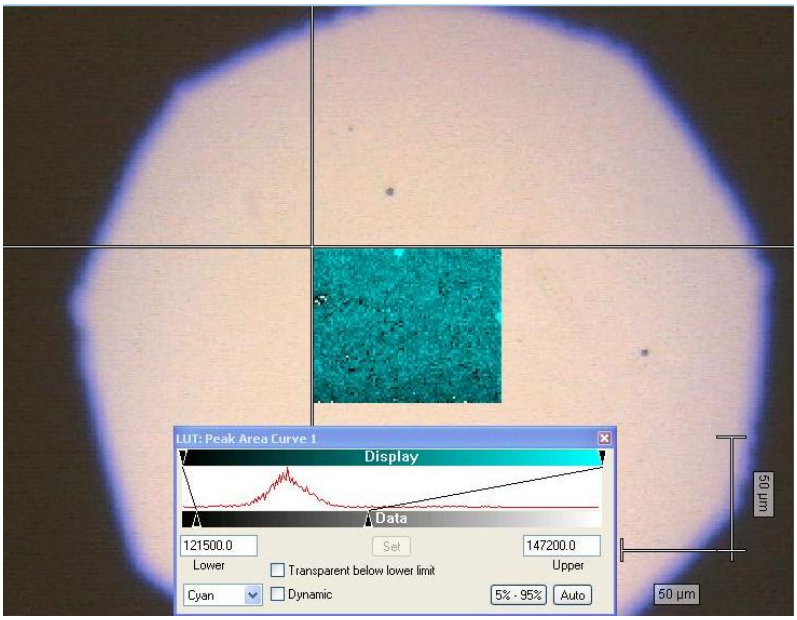

Figure 4. 7 A mapping of 302 cm^{-1} Raman mode for the undoped $B_5C_1H_2$ film over an area of 90×70 μm^2.

REFERENCES

1. Thévenot, F., *Boron carbide- comprehensive review.* Journal of the European Ceramic Society, 1990. **6**(4): p. 205-225.
2. Hall, H.T. and L.A. Compton, *Group IV Analogs and High Pressure, High Temperature Synthesis of B_2O.* Inorganic Chemistry, 1965. **4**(8): p. 1213-1216.
3. Chen, M., J.W. McCauley, and K.J. Hemker, *Shock-Induced Localized Amorphization in Boron Carbide.* Science, 2003. **299**(5612): p. 1563-1566.
4. Chen, M.W., et al., *Microstructural Characterization of Commercial Hot-Pressed Boron Carbide Ceramics.* Journal of the American Ceramic Society, 2005. **88**(7): p. 1935-1942.
5. Wood, C. and D. Emin, *Conduction mechanism in boron carbide.* Physical Review B, 1984. **29**(8): p. 4582-4587.
6. Bouchacourt, M. and F. Thevenot, *Analytical investigations in the B-C system.* Journal of the Less Common Metals, 1981. **82**(0): p. 219-226.
7. Lazzari, R., et al., *Atomic Structure and Vibrational Properties of Icosahedral B_4C Boron Carbide.* Physical Review Letters, 1999. **83**(16): p. 3230-3233.
8. Mauri, F., N. Vast, and C.J. Pickard, *Atomic Structure of Icosahedral B_4C Boron Carbide from a First Principles Analysis of NMR Spectra.* Physical Review Letters, 2001. **87**(8): p. 085506.
9. Armstrong, D.R., et al., *The nature of the chemical bonding in boron carbide. IV. Electronic band structure of boron carbide, $B_{13}C_2$, and three models of the structure $B_{12}C_3$.* Acta Crystallographica Section B, 1983. **39**(3): p. 324-329.
10. Masatoshi, Y., *Electronic Band Structure of Boron Carbide.* The Journal of Chemical Physics, 1957. **27**(3): p. 746-751.

11. James, E.S., S. Shunli, and L. Zi-Kui, *The structural evolution of boron carbide via ab initio calculations.* Applied Physics Letters, 2007. **91**(23): p. 231915.

12. Kwei, G.H. and B. Morosin, *Structures of the Boron-Rich Boron Carbides from Neutron Powder Diffraction: Implications for the Nature of the Inter-Icosahedral Chains.* The Journal of Physical Chemistry, 1996. **100**(19): p. 8031-8039.

13. Kuhlmann, U., H. Werheit, and K.A. Schwetz, *Distribution of carbon atoms on the boron carbide structure elements.* Journal of Alloys and Compounds, 1992. **189**(2): p. 249-258.

14. Aselage, T.L., D. Emin, and S.S. McCready, *Conductivities and Seebeck coefficients of boron carbides:Softening bipolaron hopping.* Physical Review B, 2001. **64**(5): p. 054302.

15. Morosin, B., et al., *Neutron powder diffraction refinement of boron carbides nature of intericosahedral chains.* Journal of Alloys and Compounds, 1995. **226**: p. 121-125.

16. *Center for Advanced Microstructures & Devices (CAMD), www.camd.lsu.edu*.

17. Orhan, K., et al., *Performance of the infrared microspectroscopy beamline at CAMD.* Review of Scientific Instruments, 2005. **76**(1): p. 013703.

18. Hong, N., et al., *Ni doping of semiconducting boron carbide.* Journal of Applied Physics, 2010. **107**(2): p. 024513.

19. *Gaussian 03, www.gaussian.com*.

20. *Sigma-Aldrich, http://www.sigmaaldrich.com.*

21. Tillekaratne, A., D. Siap, and M. Trenary, *Adsorption and Dehydrogenation of Ortho-Carborane on the Pt(111) Surface.* The Journal of Physical Chemistry C, 2008. **112**(23): p. 8682-8689.

22. Shirai, K., et al., *Infrared study of amorphous $B_{1-x}C_x$ films.* Journal of Applied Physics, 1995. **78**(5): p. 3392-3400.

23. Paroli, R.M., et al., *Variable-temperature and -pressure vibrational spectra of o-carborane.* Inorganic Chemistry, 1989. **28**(10): p. 1819-1823.

24. Leites and A. L, *VIBRATIONAL SPECTROSCOPY OF CARBORANES AND PARENT BORANES AND ITS CAPAILITIES IN CARBORANE CHEMISTRY*. Vol. 92. 1992, Washington, DC, ETATS-UNIS: American Chemical Society. 45.

25. Blum, N.A., C. Feldman, and F.G. Satkiewicz, *Infrared absorption of amorphous boron films containing carbon and hydrogen.* physica status solidi (a), 1977. **41**(2): p. 481-486.

26. Jacobsohn, L.G., et al., *Role of intericosahedral chains on the hardness of sputtered boron carbide films.* Applied Physics Letters, 2004. **84**(21): p. 4173-4175.

27. van den Brand, J., et al., *Interaction of Anhydride and Carboxylic Acid Compounds with Aluminum Oxide Surfaces Studied Using Infrared Reflection Absorption Spectroscopy.* Langmuir, 2004. **20**(15): p. 6308-6317.

28. Shirai, K. and S. Emura, *Lattice vibrations and the bonding nature of boron carbide.* Journal of Physics: Condensed Matter, 1996. **8**(50): p. 10919.

29. Herman, S., A. Terry, and E. David, *Infrared absorption in boron carbides: Dependence on isotopes and carbon concentration.* AIP Conference Proceedings, 1991. **231**(1): p. 322-325.

30. Shirai, K. and S. Emura, *Lattice Vibrations of Boron Carbide.* Journal of Solid State Chemistry, 1997. **133**(1): p. 93-96.

31. Werheit, H., et al., *FT-Raman spectra of isotope-enriched boron carbide.* Journal of Solid State Chemistry, 2004. **177**(2): p. 569-574.

32. Guo, J., et al., *Pressure-induced depolarization and resonance in Raman scattering of single-crystalline boron carbide.* Physical Review B. **81**(6): p. 060102.

33. Chaudhari, P., et al., *Hot wire chemical vapour deposition (HWCVD) of boron carbide thin films from ortho-carborane for neutron detection application.* Thin Solid Films. **519**(14): p. 4561-4564.

34. Werheit, H., et al., *Some properties of single-crystal boron carbide.* Journal of Solid State Chemistry, 2004. **177**(2): p. 575-579.

35. Billa, R.B., et al., *Annealing effects on the optical properties of semiconducting boron carbide.* Journal of Applied Physics, 2009. **106**(3): p. 033515.

Chapter 5 Ni Doping of Semiconducting Boron Carbide

*This chapter is taken from my journal publication, Journal of Applied Physics **107**, 024513 (2010), with some supplemental results.*

5.1 Introduction

In the development of a semiconductor, the ability to control both n- and p- type doping is of paramount importance for device applications [1]. The development of a semiconducting form of boron carbide has resulted in heterojunction diodes [2-6], a junction gate field-effect-transistor (JFET) [2], Esaki-type tunnel diodes [3,7,8], homojunction diodes [3], heterojunction neutron detector [9-10], a high temperature heterojunction diode with SiC [4], and a homojunction neutron detector. Semiconducting boron carbide devices have been found to be valuable in a variety of unique device applications. Chief among them are solid state neutron detectors due to the high cross section of ^{10}B for thermal neutrons [13, 14] and the ability to both capture neutrons and sweep out charge in the same material. In addition, the high resistivity and dielectric constant of boron carbide (~8) make it eminently suitable as a tunneling barrier for magnetic tunnel junctions [15]. Photoemission studies of boron carbide/Co interfaces show no quenching of the Co magnetic moment at the interface, an important consideration for spintronic applications [16]. Controlled doping of the boron carbide barrier layer will allow for precise positioning of the Fermi level, hence changing the tunneling characteristics.

In the absence of intentional doping, boron carbide is a p-type semiconductor with resistivity of $\sim 10^{10}\ \Omega cm$ at room temperature. Ni has been found to be an excellent n-type dopant [3,7,8], and boron carbide homojunction diodes have been made using Ni doped n-type and undoped p-type boron carbide. The correlation between increasing Ni concentration and n-

type semiconducting characteristics are confirmed by XPS and I-V measurement. Ni doping results in a significant upward shift of the Fermi level and does not lead to significant changes in the surface quality; however x-ray diffraction results indicate a change in the crystallinity.

5.2 Experimental details

The PECVD growth of semiconducting boron carbide films has been well-documented [4]. PECVD lends itself quite easily to good control of the dopant density, if a suitable precursor molecule can be found. $C_2B_{10}H_{12}$ (orthocarborane) [17] is used as the precursor molecule for boron carbide deposition, and $Ni(C_5H_5)_2$ (nickelocene) [17] as the source molecule for introduction of the Ni dopant [3,7,8]. A vial of nickelocene in parallel with the orthocarborane vial (at a temperature of 90 ℃) is inserted into the gas handling system and maintained at a temperature of 27 ℃. The argon gas flow through the two vials is varied as shown in table 5.1. The ratio of the two precursors in the mix will depend on the respective vapor pressures and inlet and outlet tube geometries and must be a monotonic function of the relative gas flows, since all other variables remain unchanged. The vapor pressures of nickelocene and orthocarborane as a function of temperature are well known [18, 19], giving a ratio of 0.001135 atoms of Ni per molecule of orthocarborane (~0.11%) for a dilution ratio of 1. For all other dilution ratios, the proportion of Ni in the gas mix will rise in proportion to the Argon gas flow. Hence for the 9:1 dilution ratio, the incoming gas will contain 1% of Ni. Two series of samples were made, one on n-type Si with a measured resistivity of 100 Ωcm corresponding to a dopant density of $4.5\times10^{13}\ cm^{-3}$ and one on p-type Si with a resistivity of 16 Ωcm corresponding to a dopant density of $1\times10^{15}\ cm^{-3}$. At each dilution ratio, the samples on the n-type and p-type Si were grown simultaneously in the same chamber; hence we expect the film compositions on the two different substrates to be identical. X-ray reflectivity data, which is not shown, indicated the

same growth rate (~ 10 nm/min) for each sample when the Ar flow rate through the orthocarborane vial is fixed. Substrates were cleaned using acetone, methanol, deionized water, and 5 % HF before insertion into the PECVD reactor. Inside the reactor, a 30 min Ar ion etch was performed prior to deposition. All samples were deposited at a substrate temperature of 330 ℃ for 1 hour, leading to films that are 600 nm thick.

The structural properties of undoped and doped boron carbide were compared by atomic force microscope (AFM) and theta-two theta x-ray diffraction (XRD) scans using Cu Kα radiation (λ=1.54 Å) at room temperature. The relative Ni concentrations as a function of the Ni source molecule's flow rate were investigated by XPS measurements using a Physical Electronics 04-548 dual x-ray anode with unmonochromatized Mg Kα radiation. The photoemission was energy analyzed with an Omnicron EA 125 concentric hemispherical analyzer operating at a constant pass energy of 15 eV for carbon, boron and oxygen, and 50 eV for nickel. The spectra were taken in 0.1 eV increments and were averaged for 25-50 scans. Binding energies were calibrated to adventitious carbon, with C1s taken to be 284.6 eV. *In situ* surface treatment could be performed with inert ion bombardment with a Physical Electronics 04-303 differentially pumped ion source. Ion sputtered substrates were treated using 3 kV Ar^+ in normal incidence mode for 40 min leading to the removal of ~ 20 nm of surface material. The x-ray absorption near edge structure (XANES) spectra were undertaken at the double crystal monochromator (DCM) beamline at the Center for Microstructures and Devices (CAMD). Monochromatic light was obtained by using a double crystal monochromator of Lemonnier type [20], equipped with Ge(220) crystal pair with overall resolution of ~2 eV. The fluorescence yield mode utilizing a Canberra 13-element high purity germanium diode array detector was

used to collect the XANES data. The monochromator was calibrated at the Ni K edge at 8333 eV using a Ni foil.

The variations in semiconducting properties were established from the I-V curves of each heterojunction diode. Circular ohmic Cr/Au contacts with diameters ranging from 1 to 5 mm were sputter deposited on both sides of the boron carbide/Si heterojunction.

Table 5. 1 Ar gas flow through the orthocarborane and nickelocene vials for all samples. The dilution ratio is defined as the ratio of Ar gas flow through the nickelocene vial to Ar gas flow through the orthocarborane vial. The Ni concentration in the gas phase increases with increasing dilution ratio.

Sample name	$B_5C_1H_2$	Ni(1)- $B_5C_1H_2$	Ni(3)- $B_5C_1H_2$	Ni(5)- $B_5C_1H_2$	Ni(7)- $B_5C_1H_2$	Ni(9)- $B_5C_1H_2$
Orthocarborane	1 SCCM	1 SCCM	1 SCCM	1 SCCM	1 SCCM	1 SCCM
Nickelocene	0 SCCM	1 SCCM	3 SCCM	5 SCCM	7 SCCM	9 SCCM
Dilution ratio	0	1	3	5	7	9

5.3 Characterization of undoped $B_5C_1H_{12}$ films

We began by characterizing the semiconducting properties of the undoped film. A typical I-V curve of undoped $B_5C_1H_2$ films (~1 μm) with Cr contacts on a sapphire substrate is shown in figure 5.1. After deposition of the $B_5C_1H_2$ layer, at 330 C, the sample is post-annealed *in-situ* at 600 ℃ in an Ar atmosphere to prevent film delamination (refer to Chapter 2). The Cr electrodes were grown directly on the sample without breaking vacuum, so as to minimize contamination of the interface between the $B_5C_1H_2$ film and the Cr electrode. The I-V curve in figure 5.1 is ohmic and indicates a resistivity of 10^8-10^{10} Ωcm (obtained from multiple samples)

for the undoped $B_5C_1H_2$ film. We were not able to deposit a good Ni-doped $B_5C_1H_2$ film on either a sapphire or a glass substrate even with post-deposition annealing. Even a small amount of Ni doping reduced the film lifetime on the insulating substrates resulting in a short circuit in the resistive layer due to film delamination.

The resistivity for p-type undoped $B_5C_1H_2$ can be written as a function of the corresponding hole mobility as given by equation (5.1), where ρ is the resistivity, N_A the density of holes, and μ_h the hole mobility. The density of holes, N_A, is obtained from C-V measurements.

$$\rho = 1/eN_A\mu_h \tag{5.1}$$

The calculated hole mobility is between 10^{-4} and 10^{-2} $cm^2/V\,s$. This low value of mobility has implications for charge capture in boron carbide neutron detectors, which we explore in Chapter 7.

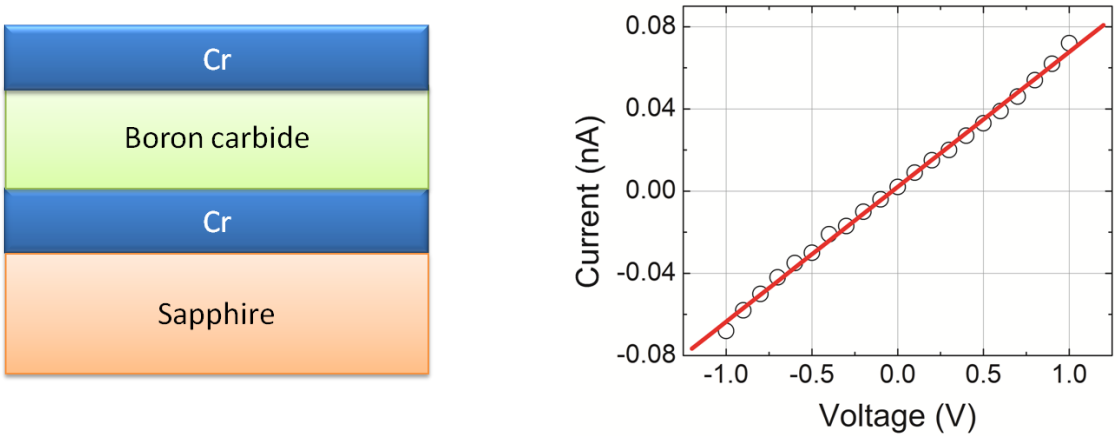

Figure 5. 1 (Left) A schematic diagram of the resistive layer consisting of Cr metal contacts and an 1 μm undoped $B_5C_1H_2$ film on a sapphire substrate. (Right) I-V curve for the resistive layer showing ohmic behavior, resulting in a resistivity of (10^8-10^{10} Ωcm) for the undoped $B_5C_1H_2$ film. The red line is a linear fit to the I-V plot.

Energy band gap measurements were performed using UV-VIS spectroscopic ellipsometry (SE) and indicate an optical band gap of 2.2 eV, which is consistent with extensive investigation of the band gap by Ravi Billa [21].

P-n diodes are the most commonly used devices for boron carbide based neutron detectors because the depletion region at the interface results in an internal electric field that sweeps out the charge produced following each neutron capture. The width of the depletion region, together with the magnitude of the reverse leakage current, which results in increased noise levels [9-11], are important parameters in the investigation and understanding of the pulse height spectra and neutron detection efficiency of these devices. Figure 5.2 shows typical I-V curves of the undoped $B_5C_1H_2$ (~500 nm)/Si p-n diode at room temperature. Here we are specifically interested in the leakage currents in the reverse bias region as a function of the diameter of the Cr/Au electrode. (the forward bias region shows little change with an almost constant turn on at ~0.7 V).

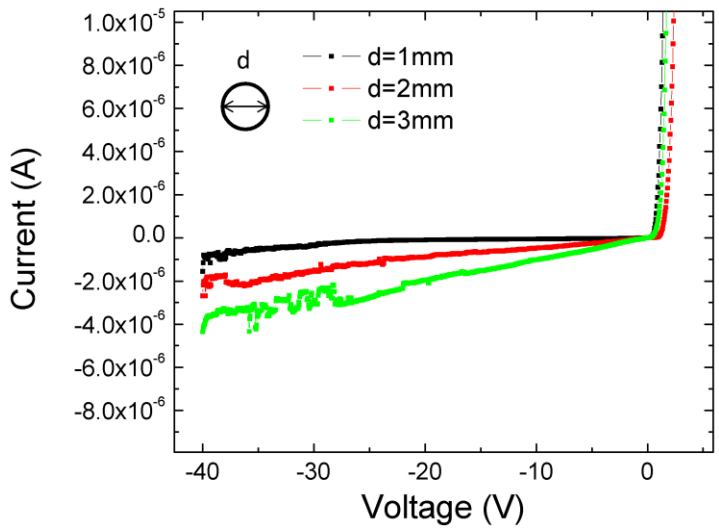

Figure 5. 2 I-V curves for three different diameters (d) of the electrodes; d=1mm (black), d=2 mm (red), and d=3 mm (green). The leakage current increases with area faster than expected.

Table 5. 2 Leakage current (A) vs. bias voltage (V) for the three electrodes (d=1 mm, 2mm, and 3mm).

Leakage Current (A) / Bias (V)	d=1 mm	d=2 mm	d=3 mm
0	3.82015×10^{-11}	6.63008×10^{-12}	1.16543×10^{-11}
-5	-3.60688×10^{-8}	-2.60796×10^{-7}	-5.35759×10^{-7}
-10	-5.72432×10^{-8}	-4.78646×10^{-7}	-1.00658×10^{-6}
-15	-7.72405×10^{-8}	-6.90868×10^{-7}	-1.52128×10^{-6}
-20	-1.02143×10^{-7}	-8.97725×10^{-7}	-1.9748×10^{-6}
-25	-1.53738×10^{-7}	-1.18876×10^{-6}	-2.77668×10^{-6}
-30	-3.66589×10^{-7}	-1.57489×10^{-6}	-2.99874×10^{-6}
-35	-5.37086×10^{-7}	-2.03641×10^{-6}	-3.46135×10^{-6}
-40	-1.56217×10^{-6}	-2.69216×10^{-6}	-4.35617×10^{-6}

The depletion region was investigated by measuring the capacitance as a function of bias voltage as shown in figure 5.3. The plots in figure 5.3 (b) shows the $1/\sqrt{V}$ dependence of the capacitance as would be expected from a step junction [22]. We calculate the doping concentration from the C-V measurement using a heterostructure p-n diode model [22]. We first assume that for reverse bias voltages greater than 10 V, the $B_5C_1H_2$ layer is fully depleted, so that increasing the reverse bias beyond this results in increases in the depletion width only on the Si side. This assumption is realistic because 1) the thickness of $B_5C_1H_2$ layer is so low (~1 μm) and 2) the doping concentration in the undoped $B_5C_1H_2$ layer is much smaller than in the n-type

Si, resulting in larger fractions of the depletion region in the Si. The depletion width of each layer is given by

$$W_{D_1} = [\frac{2N_{A2}\varepsilon_1\varepsilon_2(V_{bi}-V)}{qN_{D1}(\varepsilon_1 N_{D1}+\varepsilon_2 N_{A2})}]^{\frac{1}{2}}, \quad W_{D_2} = [\frac{2N_{D1}\varepsilon_1\varepsilon_2(V_{bi}-V)}{qN_{A2}(\varepsilon_1 N_{D1}+\varepsilon_2 N_{A2})}]^{\frac{1}{2}}, \quad C_{D_{1(2)}} = \frac{\varepsilon_{1(2)}}{W_{D_{1(2)}}} \tag{5.2}$$

where, W_D is a depletion width, $C_D$is the capacitance per unit area of the junction, $N_A(N_D)$ is the acceptor (donor) impurity concentration, ε is permittivity, $V_{bi}$is the built-in potential (=0.7 V), V is the applied bias voltage, and 1(2) denotes the $B_5C_1H_2$ (Si) layer. Therefore, the slope of the C^2 vs. $1/(V_{bi}-V)$ line beyond 10 V is entirely due to increasing depletion in the Si. The dopant concentration of the n-type Si is known and is equal to 4.5×10^{13} cm^{-3}, and the dielectric constant of the $B_5C_1H_2$ layer is ~8. Using the parameters, we obtain a dopant concentration of 4.5×10^{12} $cm^{-3}$for the undoped $B_5C_1H_2$ layer.

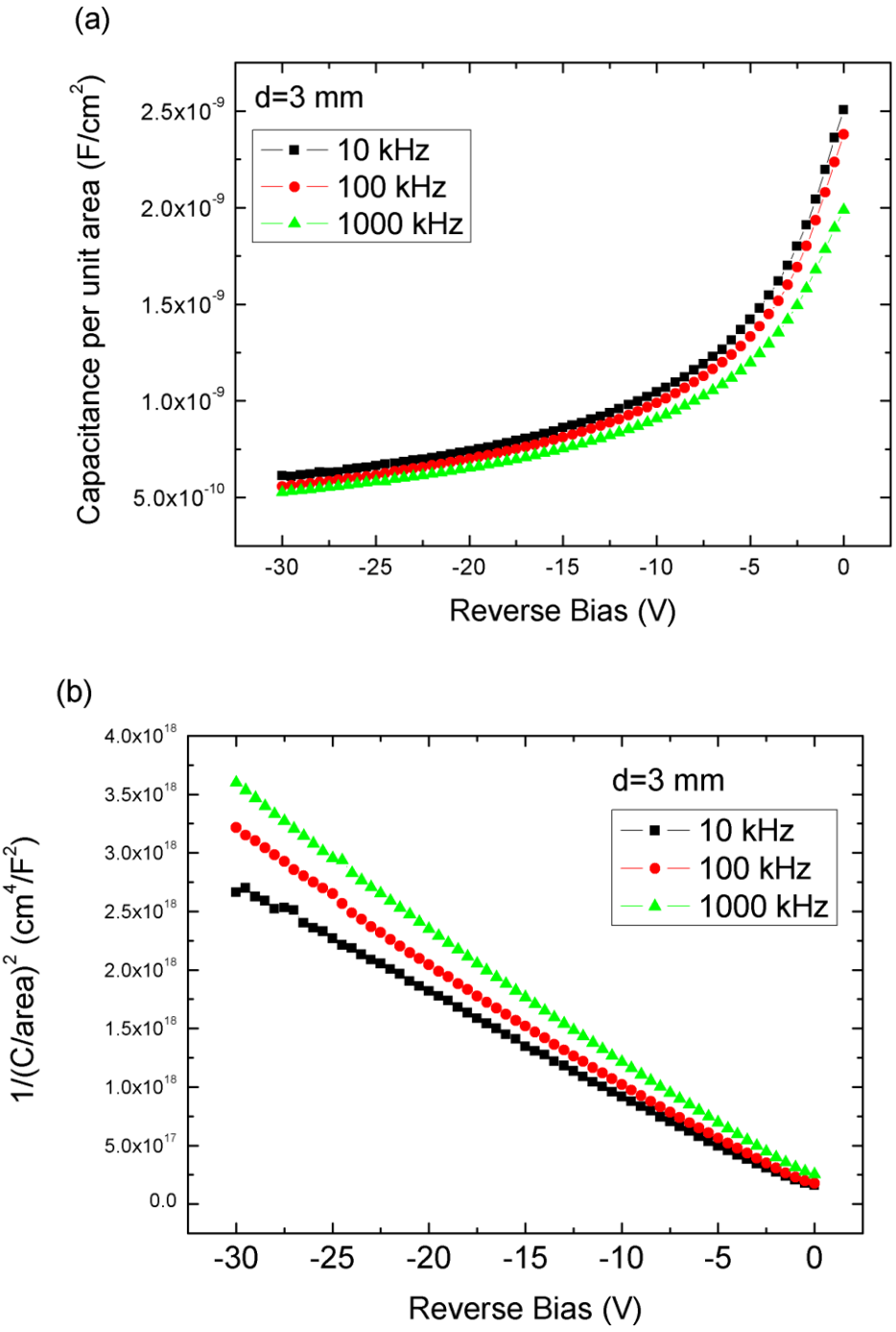

Figure 5. 3 C-V curves for a 3 mm diameter electrode as a function of bias voltage at three different frequencies at room temperature.

5.4 Ni doping

The structure of the interface is an important parameter in the development of tunnel junctions and homojunction diodes. The AFM images of undoped (left) and highly doped (right) boron carbide films on Si substrates in figure 5.4 indicate an rms roughness of 2.1 nm and 2.5 nm respectively. High dopant concentrations have no discernible effect on the surface roughness, leading us to conclude that PECVD is a viable method for the growth of homojunction diodes and highly doped tunnel junctions.

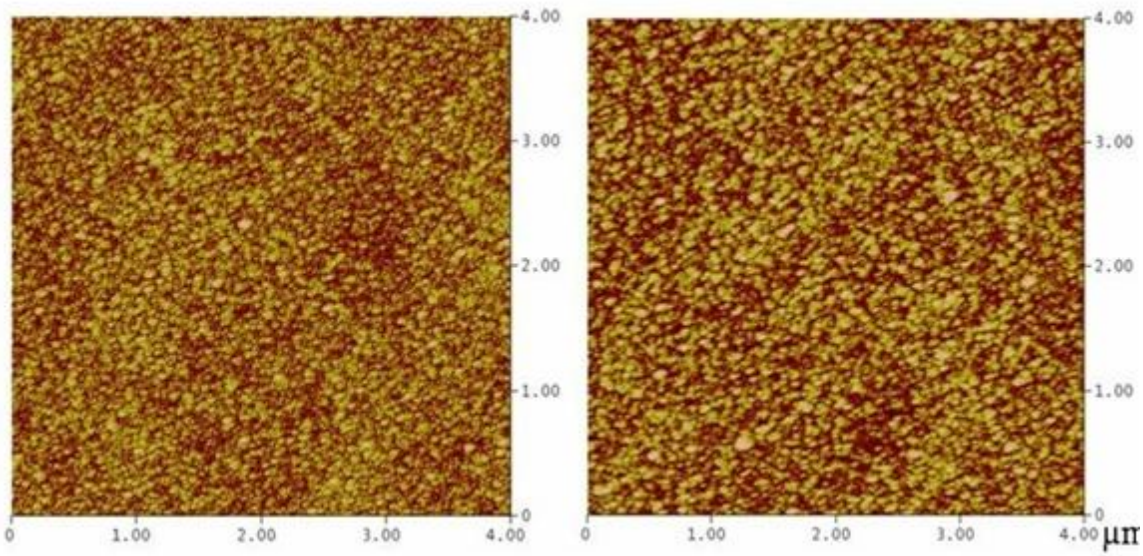

Figure 5. 4 AFM images for undoped $B_5C_1H_2$ (left) and Ni(9)-$B_5C_1H_2$ (right) on Si substrates, showing no significant change in the surface quality. Rms roughness values are 2.1 nm for $B_5C_1H_2$ and 2.5 nm for Ni(9)- $B_5C_1H_2$. The z range is 15 nm.

XRD scans are shown in figure 5.5 for a subset of the samples. The undoped and lightly doped films show x-ray peaks at 2ϑ ~23.5^o and 43^o and typical crystallite sizes of ~ 10 nm, substantially less than the film thickness of 600 nm [4]. Two key differences between these two films are observed: in the undoped film, the peak at 43^o consists of two barely resolved peaks at

42.7^{o} and 43^{o}, whereas in the lightly doped sample, only a single peak at 43.59^{o} is seen. The ratio of the intensities of the two peaks (at 43^{o} and 23^{o}) changes from ~7.5 for the undoped sample to 17 for the lightly doped sample. The more highly doped $B_5C_1H_2$ films show no x-ray diffraction peaks, implying that the addition of Ni leads to yet further disruption of any crystalline structure. Similar effects have been seen in sputtered semiconducting thin films and have been attributed to decreasing crystallite size with increasing dopant concentration [23]. Identification of the crystal structures of boron carbide based on x-ray data is fraught with difficulty, owing to the plethora of similar crystal structures that may differ only in the placement of C atoms and/or small differences in the size of the unit cell (and hence the position of the diffraction peak). All are based on the structure of icosahedral B, with the icosahedra at the corners and/or faces of rhombohedral and tetrahedral unit cells. Restricting ourselves to a single polytype, the positions of the split peak at 43^{o} for the undoped sample and the peak at 23^{o} indicate a structure similar to the crystal structure for orthorhombic B_8C [24]. Differences in the relative intensities as compared to the powder pattern may be attributed either to a preferential growth direction or to the presence of 2 C atoms in the icosahedra from the precursor molecule. At low levels of Ni doping, the crystallite sizes are not reduced, but the change in the relative intensities may imply a change in the preferred orientation. N-type doping of rhombohedral boron with transition metal elements [25] in powder samples indicate that the transition metal elements enter interstitial sites, while maintaining the overall crystal structure, at concentrations far higher than in the present samples. EXAFS and XANES measurements of Co doped boron carbide at concentrations of ~1% [26] are consistent with Co atoms replacing one of the icosahedral atoms. As we shall show below, the Ni atom concentrations in the present samples

are well below this range, and hence structural information on the position of the Ni atoms is hard to obtain.

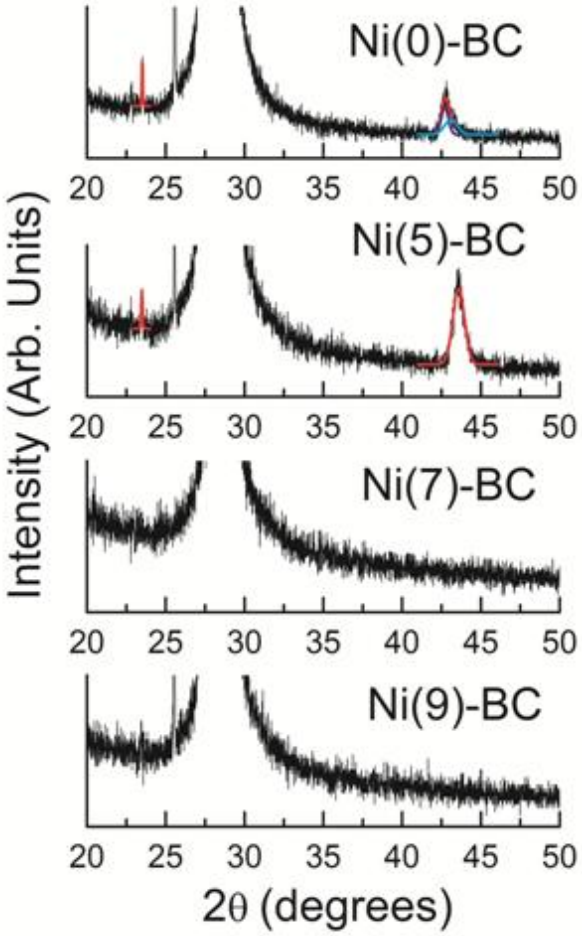

Figure 5. 5 XRD data for Ni(0, 5, 7, and 9)-$B_5C_1H_2$ films on Si substrates over a selective region (20°-50°) chosen to optimally display the $B_5C_1H_2$ peaks. The Si (111) and SiO_2 peaks are at 28.5° and 25.5°, respectively. Undoped $B_5C_1H_2$ and Ni(5)-$B_5C_1H_2$ show diffraction peaks at 23.5° and 43°. The peak at 43° in the undoped sample consists of two peaks at 42.7° and 43° with almost equal intensities. In the Ni(5)-$B_5C_1H_2$ sample, a single peak at 43.59° is seen. The relative intensities of the x-ray peaks are obtained from Gaussian fits shown. No peaks are seen for Ni(7)- $B_5C_1H_2$ and Ni(9)- $B_5C_1H_2$.

To investigate the presence of Ni atoms in the semiconducting thin film, both XPS and XANES measurements are shown in figure 5.6. The Ni2p region shown in figure 5.6 (b) was

obtained after Ar ion sputtering, showing peaks that are characteristic of metallic Ni with low satellite structure and binding energies of $2p_{3/2}$ = 852.1 eV and $2p_{1/2}$ = 869.5 eV comparable to literature spectra for the metal [27], consistent with the interstitial sites shown previously for transition metal dopants [25, 28]. Similar measurements taken before surface sputtering (figure 5.6 (a)) showed the existence of NiO with $2p_{3/2}$ = 854.5 eV and $2p_{1/2}$ = 872.2 eV and strong, characteristic satellite structure, indicating the presence of surface oxides. To calculate relative concentrations, the Ni$2p_{3/2}$ peak in the sputtered samples is normalized by the total area of the B1s peak intensity obtained on the same sample and this normalized peak intensity is shown in figure 5.6 (c) as a function of the nickelocene flow rate. Since a fixed Ar flow rate through the orthocarborane vial was used (resulting in the same growth rate for each sample), we assume a constant quantity of boron within the film. The undoped sample shows Ni peak intensities barely above the noise level. As the nickelocene ratio increases, so too does the relative Ni concentration, leading us to conclude that the atomic ratios in the thin film are essentially proportional to the gas phase ratios. XANES measurements of the characteristic absorption edge of nickel at a value close to the expected 8333 eV of the Ni K-edge, are shown in the inset to figure 5.6 (c) on the 7:1 sample, providing additional confirmation of the presence of Ni within the film. The shape of the signal is distinct from that of pure Ni, indicating hybridization of the Ni atoms. Exact details of the hybridization will require samples with much higher doping levels. The detection limit for this XANES set up is 10 p.p.m. and an order of magnitude estimate of the amount of Ni in the sample indicates a level of ~0.1%, significantly reduced from the proportion of Ni atoms in the precursor gas mix, which is calculated at close to 0.8%. These minute quantities of dopant atoms have a significant effect on the electronic properties, a characteristic

of doping, quite distinct from the Co and Fe doped $B_5C_1H_2$ films, with far higher impurity concentrations of ~ 1% within the film.

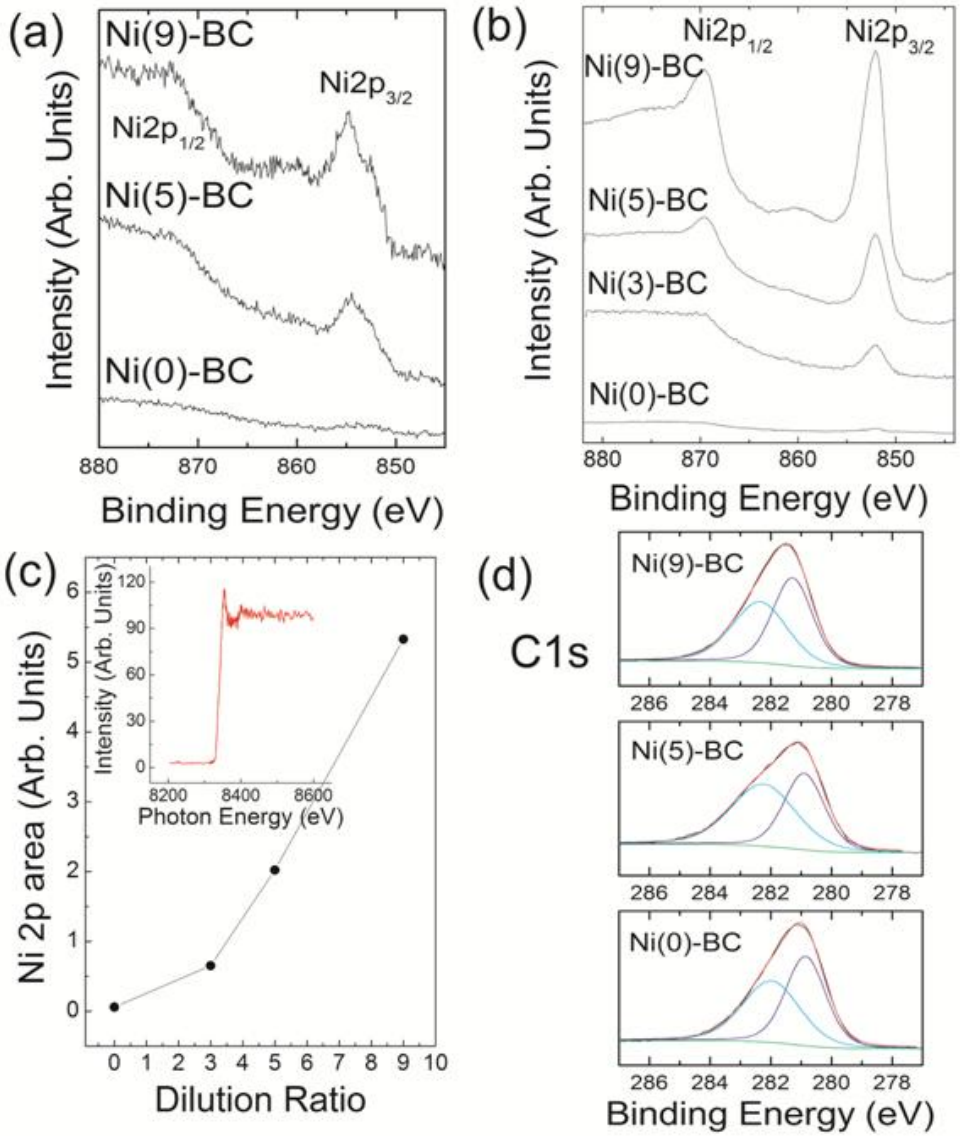

Figure 5. 6 Ni 2p XPS spectrum (a) before and (b) after sputtering to remove surface contaminants. Measurements of the surface before sputtering indicate the presence of NiO. After sputtering, the peak shape is similar to that of metallic Ni. (c) Plot of Ni 2p peak area as a function of dilution ratio. The Ni peak intensity is normalized to the area under the corresponding B1s peak. Increasing the ratio of Ni in the gas phase leads to a corresponding increase of Ni concentration in the thin films. The inset shows the XANES data of a Ni(7)-$B_5C_1H_2$ thin film, showing the Ni edge close to the expected energy of 8333 eV. (d) C1s XPS spectrum after sputtering showing the absence of graphitic carbon in both undoped and Ni doped boron carbide.

Concerns regarding the C content of the nickelocene precursor molecule and its effects on the $B_5C_1H_2$ structure were probed by XPS measurements of the C1s peak as a function of Ni doping. We looked for both an increase in graphitic carbon as well as changes in the icosahedral cage. Figure 5.6 (d) shows C1s peaks for the Ni(0, 5, 9)- $B_5C_1H_2$ samples after Ar+ ion sputtering. Each peak was fit (using a 25% Lorentzian-Gaussian function) to two separate peaks. The blue peak at 281.0 eV corresponds to the C-B-C chain and the cyan peak at 282.2 eV corresponds to the $B_{11}C$ icosahedral cage [29, 30]. There is no substantial change in the ratio or position of the two peaks on increasing the Ni concentration from 0 to the highest doped 9:1 sample. Moreover, unlike sputter deposited $B_5C_1H_2$ films [29, 30], these PECVD grown boron carbide films do not show the presence of the characteristic graphite peak at ~ 284.4±0.2 eV, either with or without the addition of Ni. This is consistent with the much higher resistivity of the PECVD [31] grown samples as compared to hot-pressed [32] and sputter deposited [29, 30] $B_5C_1H_2$ samples.

With increased concentrations of dopant atoms, distinct changes in the electronic properties are apparent in the room temperature I-V curves of the complete series of heterojunction diodes, shown in figure 5.7. Positive voltage is applied to the p-type layer, i.e. boron carbide layer (p-type Si layer) in the left (right) panel. The figure dramatically illustrates the effect of increased doping. Undoped boron carbide on n-type Si forms excellent diodes. Looking from top to bottom in the left panel for n-type Si substrates, the diode quality worsens with increased Ni doping, until at a dilution ratio of 1:9, the I-V curve reverses. In contrast, in the right panel for p-type Si substrates, the diode properties *improve* with increased Ni doping. Clearly, increasing the concentration of Ni results in a substantial increase of n-type character.

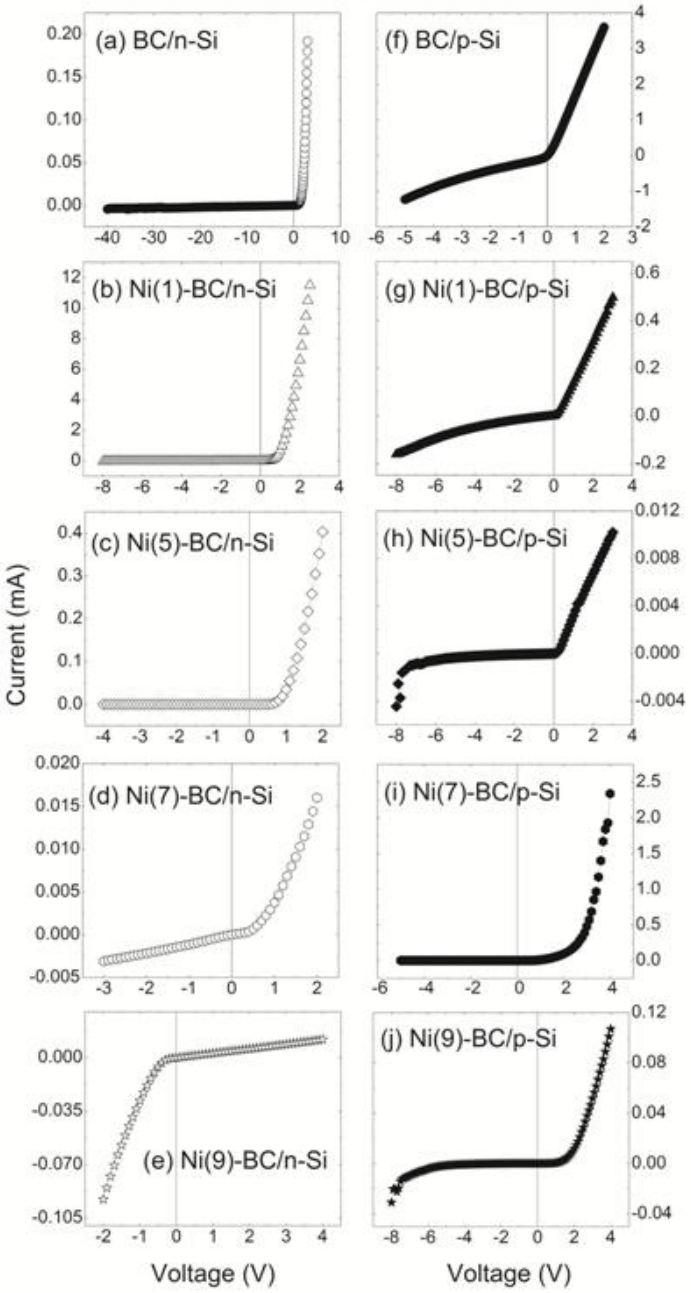

Figure 5. 7 Current-Voltage (I-V) curves of Ni(X)-$B_5C_1H_2$ (X=0, 5, 7, and 9) on n-type Si (left hand column, figures a-e) and on p-type Si (right hand column, figures f-j) at room temperature showing clear evidence for the trend towards n-type behavior at higher doping concentrations.

The forward biased turn on voltage, V_{bi}, is a measure of the difference in Fermi levels between two isolated semiconductors, in our case, Si and $B_5C_1H_2$ – changes in V_{bi} reflect a change in the Fermi level, a signature of doping. The net increase in V_{bi} in going from the undoped, p-type $B_5C_1H_2$ to the highest Ni doping concentration is 0.8 V, raising the Fermi level by 0.8 eV, a significant fraction of the optically measured band gap of 2.2 eV in $B_5C_1H_2$. In terms of energies,

$$qV_{bi}=q\chi^{B_5C_1H_2}+(E_c^{B_5C_1H_2}-E_F^{B_5C_1H_2})-[q\chi^{Si}+(E_c^{Si}-E_F^{Si})] \quad (5.3)$$

where χ, E_C, and E_F are the electron affinities, the conduction band energies, and the Fermi levels in each semiconductor.

Although the electron affinity and the position of the Fermi level are not known for the $B_5C_1H_2$ film, we can tentatively draft a possible band structure for the Si/ $B_5C_1H_2$ heterojunction diodes if we assume that the electron affinity and band gap do not change with doping i.e. that we are in the non-degenerate limit. For $B_5C_1H_2$ on n-type Si - corresponding to the I-V curves in the left column – the diode curve reverses at the highest doping concentration studied, providing an important quantifiable piece of evidence for placement of the energy bands. The Fermi level for the n-type Si substrate is 0.337 eV below the conduction band. The Fermi level for the $B_5C_1H_2$ film is below this level until a doping concentration corresponding to a dilution ratio of >7 is reached. At a dilution ratio of 9, the I-V curve reverses, implying that it is now easier for electrons to diffuse from the $B_5C_1H_2$ to the Si. Together with the knowledge of the band gap of $B_5C_1H_2$ and the shift of the Fermi level upward by 0.8 eV, the final Fermi levels are tightly constrained and are shown graphically in figure 5.8 for the $B_5C_1H_2$/Si heterojunction. At equilibrium, the Fermi levels are constant across the heterojunction. The I-V curve indicates that $E_c^{B_5C_1H_2}$ is higher than E_c^{Si} until a dilution ratio of 9 is reached, at which point the Fermi level in

the $B_5C_1H_2$ has shifted upwards towards the conduction band by 0.8 eV and E_C ^{B_5C_1H_2} is lower than E_c^{Si}. Algebraically, we can express this as

$$(E_c\text{-}E_F)_{\text{ for undoped } B_5C_1H_2} \text{ -0.8 eV} < (E_c\text{-}E_F)_{\text{ for the given n-type Si.}} \quad (5.4)$$

which implies that for undoped $B_5C_1H_2$ the Fermi level can be *at most* 0.037 eV below mid-gap, very close to intrinsic (Note that we have neglected the effects of the interface dipole potential, a correction which amounts to ~0.1 eV for most heterojunctions [33]). A similar structure for the p-type Si substrate, in which the Fermi level is 0.245 eV above the valence band, may also be constructed.

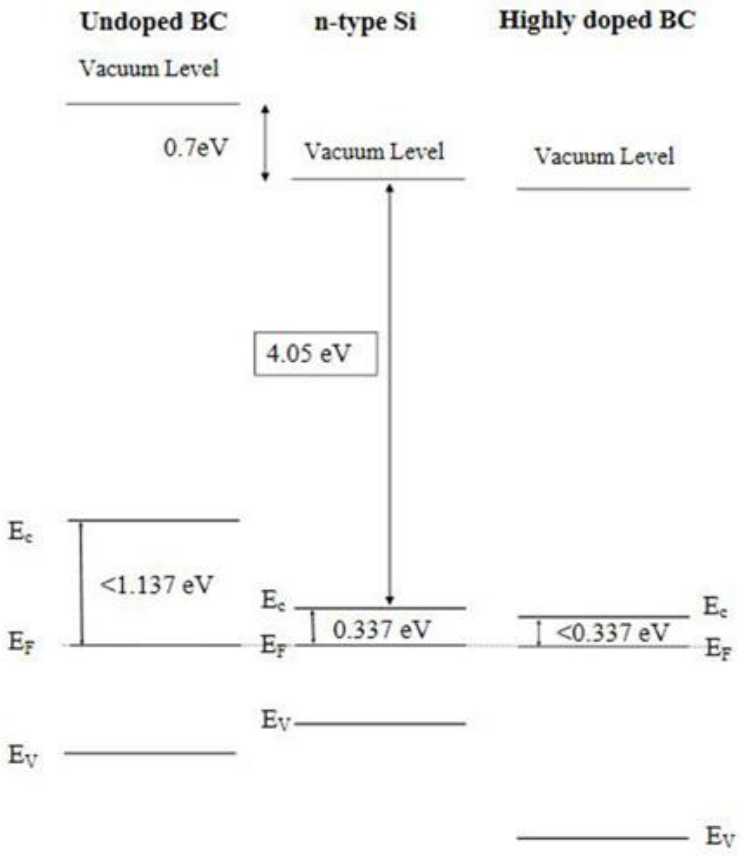

Figure 5. 8 Energy band diagram of undoped $B_5C_1H_2$, n-type Si, and highly Ni doped $B_5C_1H_2$. The electron affinity for $B_5C_1H_2$ is unknown. The constraints on the positions of the Fermi level in the $B_5C_1H_2$ arise from the behavior of the I-V curves with increased doping. All quantities for the Si substrate are well known. For details see text.

For crystalline heterojunction diodes in the non-degenerate limit, the relationship between the energy levels and doping concentrations is straightforward and V_{bi} is given by

$$V_{bi} = \Delta\chi + \frac{kT}{q}\ln\left[\frac{n_n N_{c,p}}{n_p N_{c,n}}\right]. \tag{5.5}$$

where $\Delta\chi$ is the difference in electron affinity values, n_n (n_p) are the electron carrier concentrations and $N_{c,n}$($N_{c,p}$) are the effective density of states at the conduction band edge on the n(p) sides of the junction. A similar expression exists for the hole concentration and the density of states at the valence band. The relative increase in carrier concentration is apparent in figure 5.9, a plot of V_{bi} versus the log of the relative Ni concentration (as obtained from XPS) normalized to the Si carrier density.

For the junctions on n-type Si, we can rewrite equation (5.4) as

$$V_{bi} = -\Delta\chi - \frac{kT}{q}\ln\left[\frac{N_{c,Si}}{N_{c,BC}}\right] - \frac{kT}{q}\ln\left[\frac{n_{BC}}{n_{Si}}\right]. \tag{5.6}$$

and, for junctions on p-type Si, as

$$V_{bi} = \Delta\chi + \frac{kT}{q}\ln\left[\frac{N_{c,Si}}{N_{c,BC}}\right] + \frac{kT}{q}\ln\left[\frac{n_{BC}}{n_{Si}}\right]. \tag{5.7}$$

V_{bi} is plotted against the natural log of the relative Ni concentration obtained from XPS, normalized to the electron carrier concentration of n or p-type Si. Assuming that Ni doping leaves both the electron affinity and the density of states unchanged and that the n-type carrier concentration in $B_5C_1H_2$ is a linear function of the Ni concentration, both sets of data should lie on straight lines with a negative slope for the diodes on n-type Si and a positive slope for those on p-type Si. Clearly, this is not the case, leading to the conclusion of a more complex relationship between the Fermi level and doping concentration. Even in the case of purely

crystalline semiconductors, N_D=n is only true when $N_D >> N_A$. In the case of doped $B_5C_1H_2$, in which the undoped material has p-type characteristics, there must be doping concentrations at which $N_D \approx N_A$, in which case the entire expression for

$$n = \frac{N_D^+ - N_A^-}{2} + \sqrt{\left(\frac{N_D^+ - N_A^-}{2}\right)^2 + n_i^2}. \quad (5.8)$$

is necessary. In the case of amorphous and micro-crystalline semiconductors in which there exists a small, albeit finite, density of states in the gap, the shift in the Fermi level due to doping is dominated by the expression

$$N_D^+ = \int \frac{g(\varepsilon)}{1 + e^{(\varepsilon - \varepsilon_F)}} d\varepsilon. \quad (5.9)$$

where N_D^+ is the density of fully ionized dopants in the semiconductor [34] and the limits of integration extend from the Fermi level of the undoped semiconductor to the conduction band edge. In these semiconductors, changes in the electronic properties arise from changes in the occupation of states within the gap. Paradoxically, as elucidated by Spears [34], in order for small concentrations of dopant atoms to produce visible changes in the electronic properties, it is necessary that the density of states in the gap be low. Preliminary photoemission measurements of this entire series of samples indicate minimal tailing and a well-defined gap with a negligible density of states within the gap.

Complex doping mechanisms have been noted in amorphous [35], microcrystalline [36], and polycrystalline Si [37] in which the interaction between dopant atoms, local defects and hydrogen passivation control the doping efficiency. Hydrogen plays an important role in passivating defects, thus enabling the structural sensitivity necessary for doping in the amorphous material. In polycrystalline Si, at low dopant atom concentrations, there is no change

in carrier concentration; the dopant atoms play the role of defect compensation, and changes in carrier concentrations are noted only at higher dopant atom concentrations. As is the case in Si:H, the CVD growth process for doping boron carbide using hydrogen rich precursor gases (specifically nickelocene) are potential sources for the introduction of hydrogen into the film. We note however, that in previous experiments using PECVD grown films of $B_5C_1H_2$ doped with nickelocene, IR measurements indicate no significant increase in the intensity of the B-H or C-H bond with doping, implying at best only a small increase in the H concentration [7]. Doping effects are readily apparent at rather low levels of doping, implying that defect compensation plays a minor role. Further measurements of the density of gap states, the electron affinity and the band structure are necessary to elucidate the doping mechanism.

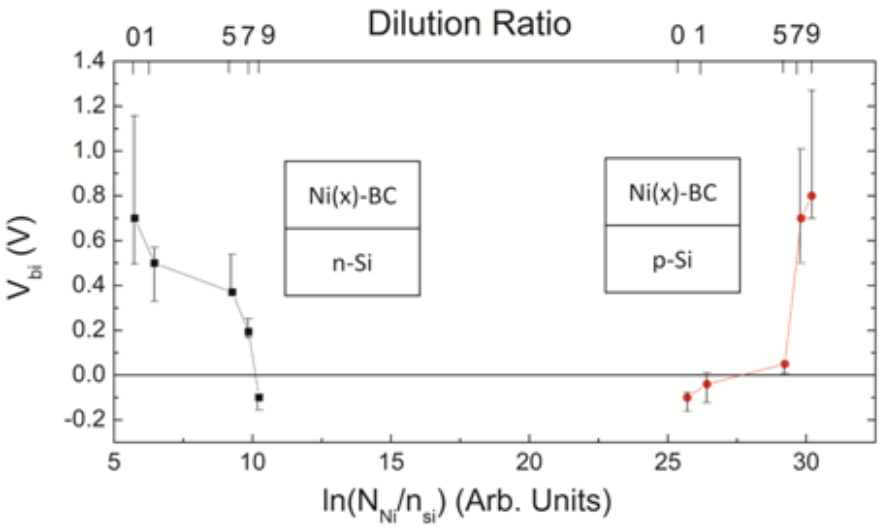

Figure 5. 9 The plots of built-in potential vs. natural log of relative Ni concentration normalized by the electron carrier concentration of n (or p)-type Si. The top scale shows the dilution ratio, increasing to the right. Since n_{Si} for the p-type Si substrate is much smaller than that for the n-type substrate, all data on the p-type Si are shifted to the right. The non-linearity of these curves indicate that the carrier concentration n in the $B_5C_1H_2$ layer is not proportional to the dopant concentration, N_D .

5.5 Conclusions

We have demonstrated controlled doping of semiconducting boron carbide thin films grown by PECVD using Ni as an n-type dopant. The overall trend from p to n was investigated as a function of dilution ratio which was controlled by the source molecule's flow rate. Doping does not affect the surface roughness, but does alter the crystal structure. Incorporation of Ni into the $B_5C_1H_2$ film was shown to be relatively inefficient; however, even these small quantities of dopant are shown to notably affect the electronic properties. Over the range of doping investigated, there is a significant change in the position of the Fermi level as measured by the built–in voltage. The controlled doping of semiconducting boron carbide over this large range is extremely promising for future applications in neutron detectors and magnetic tunnel junctions.

REFERENCES

1. Braunstein, G., et al., *p type doping of zinc oxide by arsenic ion implantation.* Applied Physics Letters, 2005. **87**(19): p. 192103.
2. Hwang, S.-D., et al., *Fabrication of boron-carbide/boron heterojunction devices.* Applied Physics Letters, 1996. **68**(11): p. 1495-1497.
3. Hwang, S.-D., et al., *Fabrication of n-type nickel doped B_5C_1 homojunction and heterojunction diodes.* Applied Physics Letters, 1997. **70**(8): p. 1028-1030.
4. Adenwalla, S., et al., *Boron carbide/n-silicon carbide heterojunction diodes.* Applied Physics Letters, 2001. **79**(26): p. 4357-4359.
5. Hong, N., et al., *Ni doping of semiconducting boron carbide.* Journal of Applied Physics, 2010. **107**(2): p. 024513.
6. Byun, D., et al., *Comparison of different chemical vapor deposition methodologies for the fabrication of heterojunction boron-carbide diodes.* Nanostructured Materials, 1995. **5**(4): p. 465-471.
7. McIlroy, D.N., et al., *The incorporation of Nickel and Phosphorus dopants into Boron-Carbon alloy thin films.* Applied Physics A: Materials Science & Processing, 1998. **67**(3): p. 335-342.
8. Hwang, S., et al., *Nickel doping of boron carbide grown by plasma enhanced chemical vapor deposition.* Journal of Vacuum Science & Technology B: Microelectronics and Nanometer Structures, 1996. **14**(4): p. 2957-2960.
9. Day, E., M.J. Diaz, and S. Adenwalla, *Effect of bias on neutron detection in thin semiconducting boron carbide films.* Journal of Physics D: Applied Physics, 2006. **39**(14): p. 2920.

10. Hong, N., et al., *Boron carbide based solid state neutron detectors: the effects of bias and time constant on detection efficiency.* Journal of Physics D: Applied Physics, 2010. **43**(27): p. 275101.

11. Robertson, B.W., et al., *A class of boron-rich solid-state neutron detectors.* Applied Physics Letters, 2002. **80**(19): p. 3644-3646.

12. Caruso, A. N., et al., *The all boron carbide diode neutron detector: Comparison with theory.* Materials Science & Engineering B, 2006. **135**: p.129-133.

13. McGregor, D.S., et al., *Self-biased boron-10 coated high-purity epitaxial GaAs thermal neutron detectors.* Nuclear Science, IEEE Transactions on, 2000. **47**(4): p. 1364-1370.

14. *ENDF: Evaluated Nuclear Data File, http://www.nndc.bnl.gov/exfor/endf.htm.*

15. Bernard, L., et al., *Magnetoresistance in boron carbide junctions.* Applied Physics Letters, 2003. **83**(18): p. 3743-3745.

16. Bernard, L., et al., *The adsorption of orthocarborane on cobalt.* Thin Solid Films, 2003. **428**: p. 253-256.

17. *Sigma-Aldrich, http://www.sigmaaldrich.com.*

18. Torres-Gómez, L.A., G. Barreiro-Rodríguez, and F. Méndez-Ruíz, *Vapour pressures and enthalpies of sublimation of ferrocene, cobaltocene and nickelocene.* Thermochimica Acta, 1988. **124**(0): p. 179-183.

19. Pathak, H.A., et al., *Gas trapping and surface analysis study of boron film deposited using Ortho-Carborane.* Fusion Engineering 2005, 21st IEEE/NPS Symposium, 2005: p. 1-4.

20. Lemonnier, M., et al., *High vacuum two crystal soft X-ray monochromator.* Nuclear Instruments and Methods, 1978. **152**(1): p. 109-111.

21. Billa, R.B., *Optical properties of semiconducting boron carbide for neutron detection applications*, in *Ph.D. dissertation, The University of Nebraska - Lincoln*. 2009.

22. Sze, S.M., *Semiconductor Devices Physics and Technology*. 2nd ed. 2002: New York: Wiley.

23. Becerril, M., et al., *Indium doping of CdTe polycrystalline films prepared by co-sputtering of CdTe--In--Cd targets.* Applied Physics Letters, 1997. **70**(4): p. 452-454.

24. Ploog, K. and M. Druminski, *Strukturchemische Charakterisierung eines durch Gasphasenabscheidung darstellbaren orthorhombischen Borcarbids der Zusammensetzung B8C.* Kristall und Technik, 1974. **9**(1): p. 25-31.

25. Werheit, H., et al., *On the electronic properties of β-rhombohedral boron interstitially doped with 3d transition metal atoms.* Journal of Alloys and Compounds, 1997. **262**(0): p. 372-380.

26. Ignatov, A.Y., et al., *Pairwise cobalt doping of boron carbides with cobaltocene.* Journal of Applied Physics, 2007. **102**(8): p. 083520.

27. Wagner, C.D., et al., *Handbook of X-Ray Photoelectron Spectroscopy*. 1979: Physical Electronics, Eden Prairie, MN.

28. Dowben, P.A., et al., *3d transition metal doping of semiconducting boron carbides.* Materials Letters, 2009. **63**(1): p. 72-74.

29. Jiménez, I., et al., *Photoemission, X-ray absorption and X-ray emission study of boron carbides.* Journal of Electron Spectroscopy and Related Phenomena, 1999. **101**(0): p. 611-615.

30. Jiménez, I., et al., *Photoemission and x-ray-absorption study of boron carbide and its surface thermal stability.* Physical Review B, 1998. **57**(20): p. 13167-13174.

31. Lee, S., et al., *Characterization of boron carbide thin films fabricated by plasma enhanced chemical vapor deposition from boranes.* Journal of Applied Physics, 1992. **72**(10): p. 4925-4933.

32. Wood, C. and D. Emin, *Conduction mechanism in boron carbide.* Physical Review B, 1984. **29**(8): p. 4582-4587.

33. Frensley, W.R. and H. Kroemer, *Theory of the energy-band lineup at an abrupt semiconductor heterojunction.* Physical Review B, 1977. **16**(6): p. 2642-2652.

34. Spear, W.E., *Doped amorphous semiconductors.* Advances In Physics, 1977. **26**(6): p. 811-845.

35. Jackson, W.B., *Microscopic mechanism for dopant activation in hydrogenated amorphous silicon.* Physical Review B, 1990. **41**(17): p. 12323-12326.

36. Spear, W.E., et al. *Electronic properties of microcrystalline silicon films prepared in a glow discharge plasma*. in *Ninth International Conference on Amorphous and Liquid Semiconductors*. 1981: Journal de Physique Colloques.

37. Taniguchi, M., et al., *Current transport in doped polycrystalline silicon.* Japanese Journal of Applied Physics, 1980. **19**: p. 665.

Chapter 6 An Introduction to Neutrons, Neutron Capture, Neutron Detectors, and Moderators

6.1 Introduction: The shortage of ^{3}He

As the nuclear weapon stockpile has declined, the U.S. supply of ^{3}He, which depends entirely on the decay of tritium (${}_1^3T \rightarrow {}_2^3He^{1+} + e^- + \bar{\upsilon}_e$), has dwindled [1]. After the 9/11 terrorist attacks, the U.S. has used large amounts of ^{3}He in portal monitors at U.S. borders in an effort to interdict illicit nuclear materials and so-called dirty bombs [2, 3]. Currently, fast neutrons emitted by weapons grade plutonium-239 are detected by gas proportional ^{3}He neutron detectors, which are one of the few detectors that are sufficiently sensitive to the relatively low flux [1]. According to the 2010 U.S. Department of Energy (DOE) report, the demand for ^{3}He is approximately 65 m^3 per year while the supply is about 20 m^3 per year [4]. This imbalance has resulted in intensive discussions of alternative neutron detector technologies for homeland security, specifically for radiation portal monitor (RPM) systems [1, 4-6].

Alternatives to ^{3}He detectors hitherto developed include BF_3 filled proportional counters, boron-lined proportional counters, lithium-6 loaded glass fibers, and wavelength-shifting fibers coated with scintillator and ^{6}Li. The advantages and disadvantages of these individual detectors are well summarized in Ref. [5, 6] and briefly explained in the next section. None possess the required combination of high neutron detection efficiency, gamma-neutron discrimination, commercial availability, non-hazardousness, and robustness of deployment [1].

Because neutrons are neutral, currently available neutron detectors use the products of neutron capture to generate a detectable signal. For example, ^{10}B based neutron detectors use the secondary charged particles consisting of alpha and ^{7}Li ions which interact with the surroundings

through ionization or generation of electron-hole pairs. The development of a neutron detector with sufficiently high detection efficiency is not trivial due to the few elements with large neutron absorption cross sections. These include ^{3}He (5360 barns), ^{6}Li (961 barns), ^{10}B (3866 barns), ^{157}Gd (254,780 barns), and ^{235}U (688 barns), where the absorption cross section is quoted for thermal 0.025 eV neutrons [7]. The detection of the secondary ions produced on neutron capture requires additional functionality in the detectors. Boron carbide solid-state neutron detectors, which are the focus of the following three chapters, are attractive candidates for a room temperature, small size, non-toxic, semiconducting neutron detector [8]. The semiconducting property of the boron carbide solid form reveals a great advantage of generating huge numbers of electron-hole pairs in the neutron capture layer because the capture reaction product ions are highly energetic (^{7}Li (0.84 or 1.02 MeV) and ^{4}He (1.47 or 1.78 MeV)) while the ionization energy to generate an electron-hole pair is of the order of a few eV. At present, our biggest limitation to large area detectors is the increase in leakage current, resulting in increased noise.

6.2 Currently available alternative neutron detectors

6.2.1 BF_3 filled gas proportional neutron detectors

The ^{10}B atoms in the BF_3 gas absorb neutrons and the neutron capture products of alpha and ^{7}Li particles are detected by the gas proportional counter. This detector shows better gamma discrimination than ^{3}He detectors [5], however it requires very high operating voltage of 2300 V which exceeds the maximum voltage that can be supplied by the Science Applications International Corporation (SAIC) RPM. BF_3 is also very toxic (CAS 7637-07-2) [9] requiring strict regulations for the material transportation. The size and fragility are typical of gas-filled detectors.

6.2.2 Boron-lined proportional counters

Boron-lined proportional counters are thin boron coated tubes filled with an appropriate gas mixture which is chosen to optimize desired counting characteristics [5]. This gas-filled proportional counter is non-toxic but the neutron detection efficiency is limited because the thickness of the boron coatings cannot usefully exceed the range of the secondary ions, which is of the order of a few microns.

6.2.3 Lithium-6 loaded glass fibers doped (or coated) with scintillating materials

Neutrons are absorbed by the ^{6}Li atoms in the glass fiber and generate charged particles ($^{6}_{3}Li + n \rightarrow {}^{3}_{1}H + {}^{4}_{2}He + 4.78\ MeV$). The fiber is either doped or coated with scintillation materials to emit light [10-12]. Glass fibers can be easily formed into the desired shapes and the detector size is variable. However, the gamma sensitivity is very high relative to ^{3}He detectors.

In contrast, solid-state semiconducting boron carbide neutron detectors are small, low mass, robust, operate at low power and at room temperature and are potentially highly efficient even at very low thickness. Below, we show the neutron absorption efficiency for enriched and naturally occurring boron carbide thin films to thermal neutrons, showing that 50% efficiency is achieved at a thickness of 25 μm.

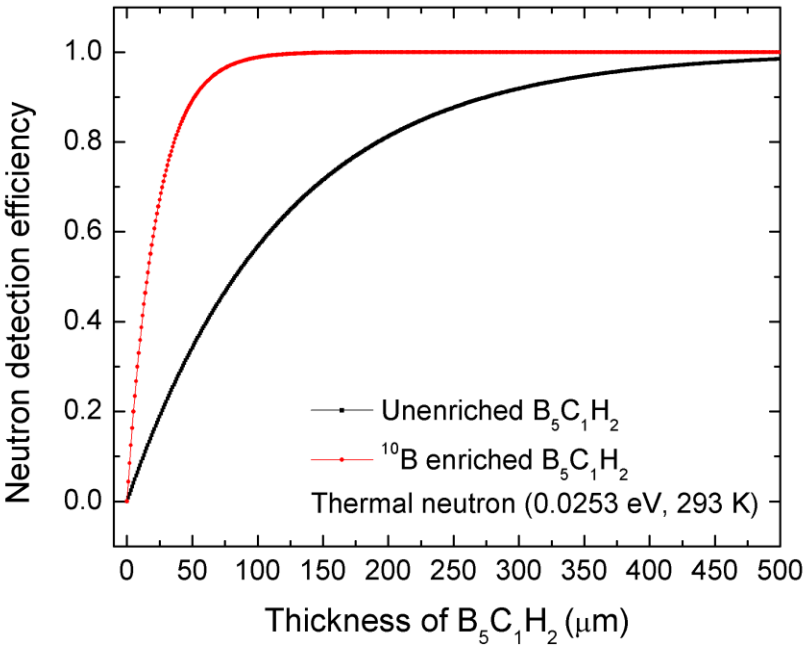

Figure 6. 1 Neutron capture efficiency for thermal neutrons for enriched and naturally occurring $B_5C_1H_2$ films.

6.3 Thermal neutrons

The neutron has no charge and a mass similar to that of a proton. The free neutron is unstable with a half-life of about 13 min and eventually decomposes to an electron, a proton, and a neutrino. Due to its charge neutrality, primary ionization by the neutron does not occur so that a neutron-nuclei reaction to generate secondary ions is necessary for neutron detection. Since the absorption cross section for the neutron-nuclei interaction is a strong function of neutron energy, different techniques have been developed for neutron detection in different energy ranges [13].

Neutrons are arbitrarily divided into slow and fast neutrons subcategories depending on the neutron's kinetic energy. Fast neutrons have energy greater than 1 eV, 0.1 MeV, or

approximately 1 MeV (depending on the definition). Slow neutrons have an energy less than or equal to 0.4 eV. Slow neutrons are further divided into smaller groups depending on their energy as shown below.

- Hot neutrons: E ~ 0.2 eV
- Thermal neutrons: E ~ 0.025 eV
- Cold neutrons: 5×10^{-5} eV < E < 0.025 eV

In this dissertation, we are mainly interested in the detection of slow neutrons using solid-state boron carbide neutron detectors.

6.3.1 Energy distribution of slow neutrons

Neutrons released by the fission reaction in a reactor or by the fusion reaction (DT or DD) of a neutron generator travel with high kinetic energies. The fast neutrons can be slowed down rapidly through numerous collisions with a moderating material and this process is called moderation or, alternatively, thermalization. Thermal neutrons are defined as neutrons in thermal equilibrium with their immediate surroundings. The energy or velocity distribution of neutrons that have been moderated by elastic collisions with moderator nuclei are approximately equivalent to a Maxwell-Boltzmann distribution, corresponding to the temperature of the surrounding medium [14, 15].

The velocity distribution of the neutrons in thermal equilibrium with a moderator can be written as

$$dn = n(v)dv = \frac{4\pi n_0}{(2\pi kT/m)^{3/2}} v^2 \exp\left(-\frac{\frac{1}{2}mv^2}{kT}\right) dv \qquad (6.1)$$

where n_0 is the number of neutrons per cm^3, m is the neutron mass, T the temperature, and k the Boltzmann constant. The corresponding energy distribution is:

$$dn = n(E)dE = \frac{2\pi n_0}{(\pi kT)^{3/2}} E^{1/2} \exp\left(-\frac{E}{kT}\right) dE \tag{6.2}$$

Here, the distribution functions n(v) and n(E) give the number of neutrons per unit velocity interval and per unit energy interval, respectively.

$$n(v) = \frac{dn}{dv} \quad \text{and} \quad n(E) = \frac{dn}{dE} \tag{6.3}$$

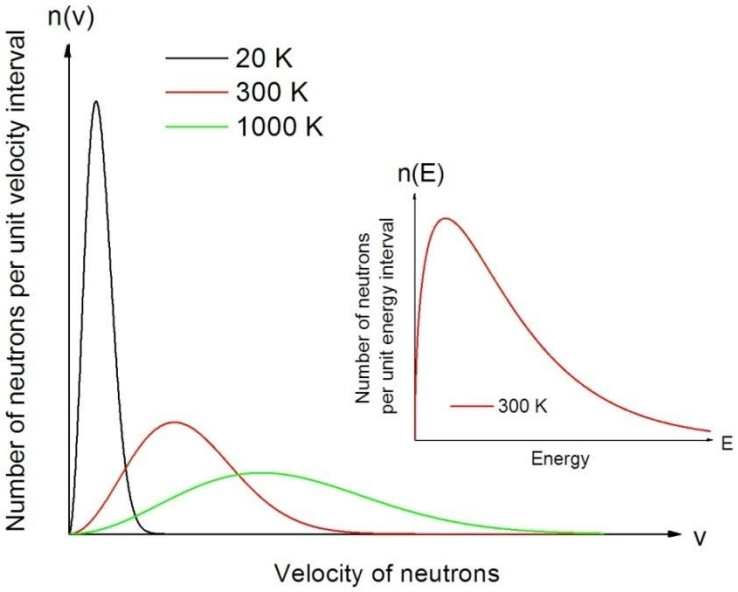

Figure 6. 2 The velocity distribution of neutrons in accordance with the Maxwell-Boltzmann distribution at 20 K (cold neutrons), 300 K (thermal neutrons), and 1000 K (hot neutrons). (Inset: Energy distribution at 300 K)

Figure 6.2 shows the Maxwell-Boltzmann distributions as a function of velocity at different moderator temperatures. By differentiating equations (6.1) and (6.2) and setting these equal to zero, the most probable velocity and the most probable energy can be obtained as follows.

- the most probable velocity $v_p = \left(\frac{2kT}{m}\right)^{\frac{1}{2}}$

- its corresponding energy $E_p = \frac{1}{2}mv_p^2 = kT$
- the most probable energy $E_0 = \frac{1}{2}kT$
- $E_p = 2E_0$

6.3.2 Neutron sources

To test boron carbide neutron detectors, we have used two neutron sources. The first one is the CG1D High Flux Isotope Reactor (HFIR) at Oak Ridge National Laboratory (ORNL) [16] that uses highly enriched uranium-235 as the fuel. It operates at 85 MW and the fast fission neutrons are thermalized (or moderated) by a liquid hydrogen moderator cooled to ~20 K to generate thermal and cold neutrons.

The other neutron source is the Thermo Scientific MP 320 neutron generator [17] in our lab which is commercially designed for field or laboratory applications. It is available with either a Deuterium-Tritium (DT) or a Deuterium-Deuterium (DD) neutron tube and results in neutrons of 14 MeV energy with a yield of 1.0×10^8 n/s. A 10 cm cube of beryllium (Be) placed directly in front of the DT generator acts as a moderator and a neutron multiplier. Moderation occurs because Be has a relatively large neutron scattering cross section, thereby slowing down the neutrons. In addition, the ^{9}Be isotope interacts with neutrons to produce 2 alpha particles and 2 neutrons, effectively doubling the number of neutrons, via the reaction

$$^9_4Be + n \rightarrow 2(^4_2He) + 2n.$$

Further moderation is achieved using a hydrogen rich material, in our case a 1 inch paraffin wax block right after the Be block and paraffin wax shielding which surrounds the neutron generator and detector system as shown in figure 6.3. The process of moderation can be treated as elastic collisions between neutrons and the nucleus of atoms in the moderator. Conservation of

momentum dictates that the energy loss of the neutron is greater for low mass target atoms. The large fraction of hydrogen in paraffin wax allows it to effectively moderate neutrons.

Calculations indicate that this combination of Be and paraffin wax are sufficient to fully thermalize the fast neutron beam and the expected energy distribution of the moderated neutrons will follow a room temperature Maxwell-Boltzmann curve. The incoming neutrons will be scattered within the paraffin wax, leading to an isotropic neutron beam on any detectors we test. We measure the neutron flux with a calibrated ^{3}He neutron detector [18] with an efficiency of 20% to thermal neutrons [18]. The ^{3}He detector is only calibrated for normal incident neutrons, resulting in difficulties in measuring the total isotropic neutron flux.

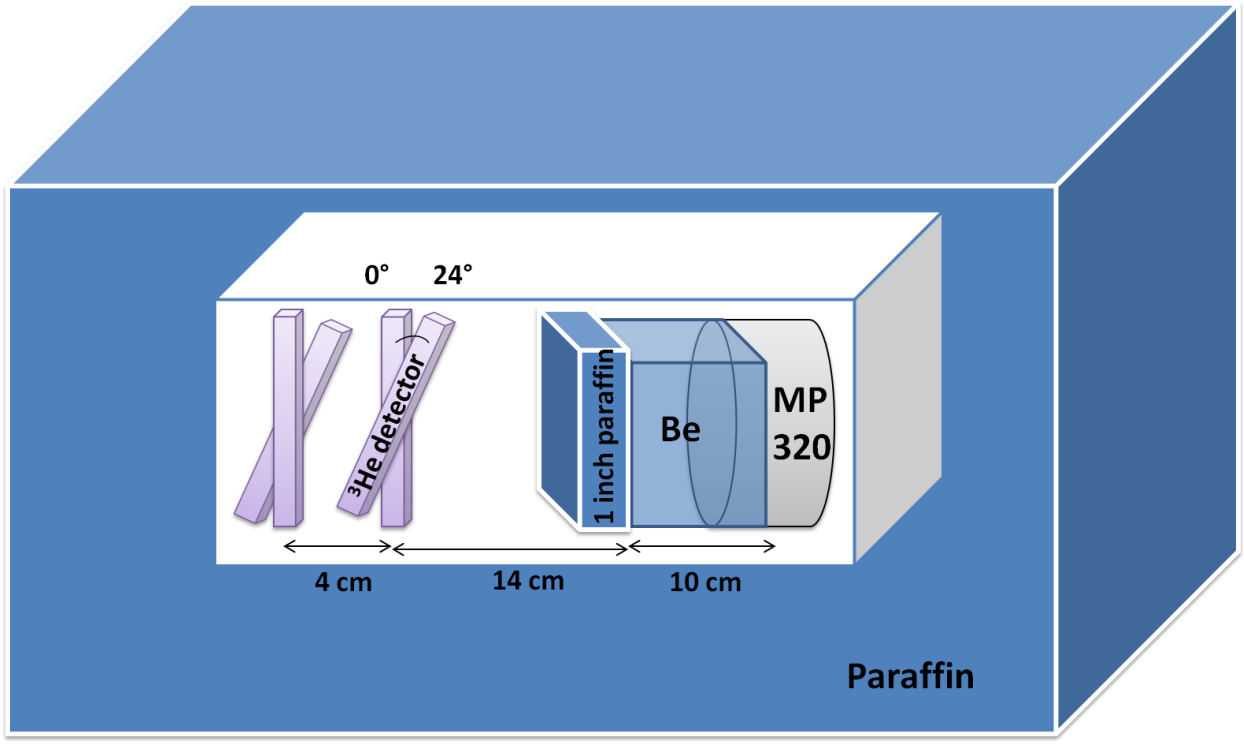

Figure 6. 3 A schematic diagram illustrating the MP 320 neutron generator and its moderation system. The position and the angle of the ^{3}He detector have been changed to test the distance and angle dependence of the neutron flux in the presence of Be and paraffin wax moderators.

6.4 Calibrations of the neutron beam flux generated by MP 320 surrounded by paraffin wax

The fast 14 MeV neutrons produced in the MP320 are emitted via a small aperture which acts as a point source, radiating neutrons in all directions. After thermalization, however, calculations indicate that the thermalized neutrons should be isotropically emitted. We have used several different geometries of the ^{3}He detector in an attempt to characterize the thermal neutron flux magnitude and direction. The detector is calibrated at 20% efficiency, but this assumes a normal incidence beam through the front face of the detector. In fact, the detector active volume is a rectangular parallelepiped of dimensions of 2.0 inch by 4.5 inch by 0.5 inch and is fully transparent to neutrons over its entire surface. This complicates the beam calibration because the path length of neutrons (and hence the probability of capture) within the detector varies with the position at which it strikes the surface. Figure 6. 4 (a) shows the counts in the ^{3}He detector (which is proportional to the neutron flux) with current in the generator when the voltage of the MP-320 is fixed and figure 6. 4 (b) shows the voltage dependence when the current is fixed. The neutron flux increases linearly with respect to the current and exponentially with respect to the voltage. This agrees with the results from the manufacturer [17].

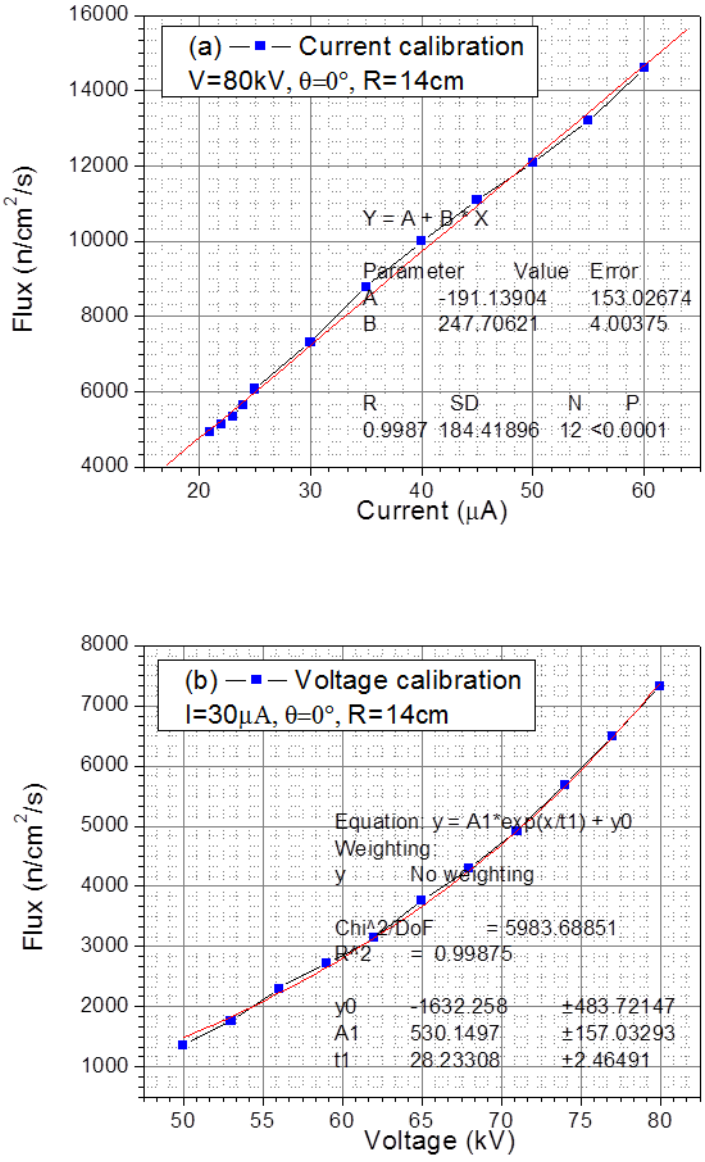

Figure 6. 4 The neutron flux calibrated by varying voltage at a fixed current of 30 μA (a) and by varying current at a fixed voltage of 80 kV (b).

To check on the beam intensity as function of angle and distance, we have performed two sets of experiments. In the first, the detector is covered with 0.025 mm thick Cd foil, which will block >94% of thermal neutrons. The relevant measurements are shown below.

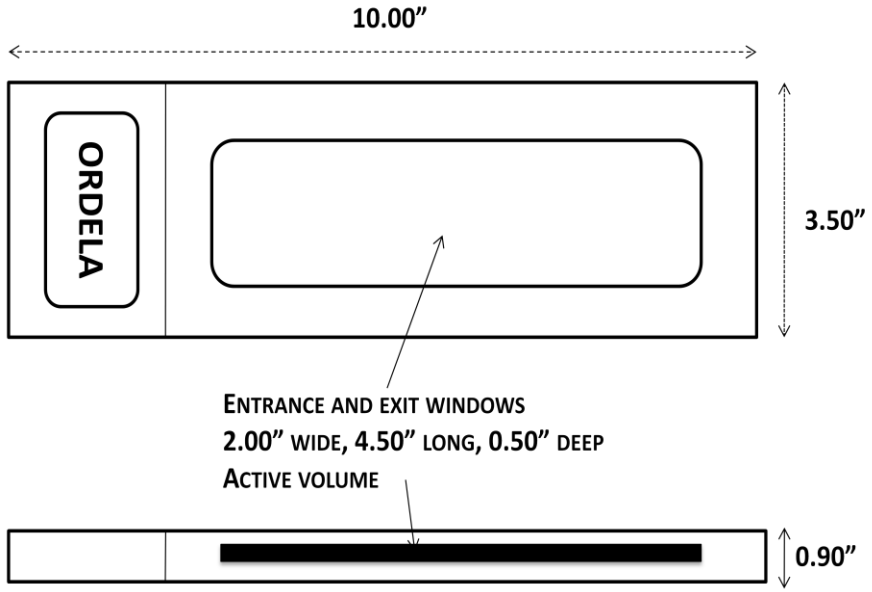

Case	Description	Neutron counts
1	The front window (2.00” ×4.50”) covered with a Cd foil and facing to the NG head	1.4×10^4
2	The front window (2.00” ×4.50”) covered a Cd foil and facing away from the NG head.	1.1×10^4
3	The front and back windows covered (2.00” ×4.50”) a Cd foil and facing to the NG head	1.02×10^4
4	All area covered (10.00” ×3.50” ×0.90”) a Cd foil and facing to the NG head	4.0×10^2
5	A circle (D=3mm) opened where all other area was covered (10.00” ×3.50” ×0.90”) a Cd foil facing to the NG head	4.0×10^2
6	Only front window opened (2.00” ×4.50”) facing to the NG head	3.0×10^3
7	Only front window opened (2.00” ×4.50”) facing away from the NG head	$3.0\sim3.05\times10^3$

Figure 6. 5 (Top) An illustration of the ^{3}He detector where the black volume contains ^{3}He gas sensitive to neutrons. (Bottom) Detector counts with Cd foil covering certain areas of the ^{3}He detector.

The comparison between 6 and 7 indicate that there is no (or little) preferred orientation of the neutron flux. Comparing 1,2 and 3 indicate that the entire cover of the detector is transparent to neutrons and that the neutrons come from all directions.

We have also varied the in-plane angle (θ) of the ^{3}He detector and the distance (R) from the Be powder block.

Table 6. 1 The neutron flux as functions of angle and distance with a constant voltage of 80 kV and a constant current of 30 μA.

	R=14 cm	R=18 cm
θ=0°	7.32×10^3 (n/cm^2·s)	3.01×10^3 (n/cm^2·s)
θ=24°	7.74×10^3 (n/cm^2·s)	3.19×10^3 (n/cm^2·s)

Table 6. 1 (second column) shows the dependence on angle when the front face of the detector is fixed at 14 cm from the Be with a constant voltage of 80 kV and a constant current of 30 μA on the MP 320. The angle is measured with respect to the surface of the neutron generator head as shown in figure 6.3. Our data show only a slight increase (of a few percent) in the measured neutron flux, as measured by the ^{3}He detector, with increasing angle. If in fact the neutrons have a preferred orientation along the beam tube direction, the increase in incident angle would result in a neutron trajectory that is approximately 10% longer in the ^{3}He detector, and result in some neutrons traversing the entire width (or length) of the detector. This would result in significantly higher neutron count numbers than observed. Table 6.1 shows the distance dependence when the angle is fixed at 0 ° and 24 °, for distances of 14 cm and 18 cm from the block. The larger distance leads to a 60% decrease in the neutron flux as the distance increases. This is evidence that the neutron beam flux is not homogeneous along the initial fast neutron beam direction. A

complete set of figures and tables for the calibration of the neutron beam using the ^{3}He detector is shown in the Appendix.

A calculation of the detection efficiency for the ^{3}He detector for any angle other than normal incidence is complicated by the finite thickness of the active volume. A neutron that enters the detector via any of the six faces has a path length within the detector that depends on the angle of incidence, the face it enters and the position at which it enters. An isotropic beam vastly complicates this already complex situation. We have instead calibrated our boron carbide detector at a well-calibrated neutron source (see Chapter 8) and used that calibration to obtain the isotropic neutron flux (see Chapter 7). We assume that at a fixed position, for a given current and voltage, the flux is constant.

REFERENCES

1. Kouzes, R.T., *The ^{3}He Supply Problem*. 2009.
2. Kouzes, R.T., *Detecting Illicit Nuclear Materials.* Journal Name: American Scientist, 93(5):422-427; Journal Volume: 93; Journal Issue: 5, 2005.
3. Kramer, D., *DOE begins rationing helium-3.* Physics Today, 2010. **63**(6): p. 22-25.
4. Kouzes, R.T. and J.H. Ely, *Status Summary of ^{3}He and Neutron Detection Alternatives for Homeland Security*. 2010.
5. Kouzes, R.T., et al., *Alternative Neutron Detection Testing Summary*. 2010. p. Medium: ED; Size: PDFN.
6. Van Ginhoven, R.M., R.T. Kouzes, and D.L. Stephens, *Alternative Neutron Detector Technologies for Homeland Security*. 2010.
7. *ENDF: Evaluated Nuclear Data File, http://www.nndc.bnl.gov/exfor/endf.htm.*
8. Caruso, A. N., *The physics of solid-state neutron detector materials and geometries*. Journal of Physics: Condensed Matter, 2010. **22**(44):p.443201.
9. Lintereur, A., et al., *3He and BF3 neutron detector pressure effect and model comparison.* Nuclear Instruments and Methods in Physics Research Section A: Accelerators, Spectrometers, Detectors and Associated Equipment. **652**(1): p. 347-350.
10. Bliss, M., et al. *Glass-fiber-based neutron detectors for high- and low-flux environments*. 1995: SPIE.
11. Seymour, R.S., et al. *Performance of a neutron-sensitive scintillating glass fiber panel for portal, freight, and vehicle monitoring*. 1999: SPIE.

12. Seymour, R., et al., *Scintillating-Glass-Fiber Neutron Sensors, their Application and Performance for Plutonium Detection and Monitoring.* Journal of Radioanalytical and Nuclear Chemistry, 2000. **243**(2): p. 387-388.

13. Knoll, G.F., *Radiation detection and measurement*. 2nd ed. 1989, New York: Wiley.

14. Isbin, H.S., *Introductory nuclear reactor theory*. Reinhold chemical engineering series. 1963, New York: Reinhold Pub. Corp.

15. Liverhant, S.E., *Elementary introduction to nuclear reactor physics*. 1960, New York,: Wiley.

16. *HFIR at ORNL, http://neutrons.ornl.gov/facilities/HFIR/*.

17. *Thermo Scientific, http://www.thermoscientific.com.*

18. *Ordela Neutron Beam Monitor Model 4511N, http://www.ordela.com*.

19. Hong, N., et al., *Boron carbide based solid state neutron detectors: the effects of bias and time constant on detection efficiency.* Journal of Physics D: Applied Physics, 2010. **43**(27): p. 275101.

Chapter 7 Boron Carbide Based Solid State Neutron Detectors: the Effects of Bias and Time Constant on Detection Efficiency

*This chapter is taken from my journal publication, Journal of Physics D: Applied Physics **43**, 275101 (2010), with some modifications and supplemental results.*

7.1 Introduction

The development of efficient all solid state neutron detectors is hampered by the transparency of most materials to the passage of neutrons. Few elements possess a significant capture cross section for thermal neutrons and, among these elements, those suitable for forming a semiconducting solid are rare indeed. Boron is uniquely suitable, having a large capture cross section for thermal neutrons, generating high energy ions that are easily detectable on neutron capture and forming a boron rich semiconducting solid, boron carbide [1, 2], grown by plasma enhanced chemical vapor deposition (PECVD). The growth and properties of a semiconducting form of boron carbide have been intensively studied for the last 20 years, resulting in heterojunction and homojunction diodes [1, 3-7], Esaki tunnel diodes [8], and, most relevant for this manuscript, solid state neutron detectors [2, 9].

These all solid state neutron detectors are quite distinct from conversion layer detectors, in which the neutron capture coatings do not function as semiconducting materials. In such conversion layer detectors, ^{6}Li, ^{10}B, ^{113}Cd, and ^{157}Gd have been used to capture the neutrons, resulting in secondary particles that are transferred to the semiconducting charge capture layers [10-13]; these neutron detectors suffer from self-absorption effects [12] that leading to low attainable efficiencies. Semiconducting boron carbide circumvents these restrictions by

combining both neutron absorption and charge capture in the same material, leading to much higher potentially attainable efficiencies.

The neutron capture reaction with ^{10}B is well known :

$$(94\%)\ ^{10}B + n \rightarrow {}^{7}Li\ (0.84\ MeV) + {}^{4}He\ (1.47\ MeV) + \gamma\ (0.48\ MeV)$$

$$(6\%)\ \ ^{10}B + n \rightarrow {}^{7}Li\ (1.02\ MeV) + {}^{4}He\ (1.78\ MeV) \qquad (7.1)$$

and results in the ejection of highly energetic charged ions that generate large numbers of electron-hole pairs in a semiconductor. Naturally occurring boron contains 19% ^{10}B; for a fully enriched thin film of boron carbide, 50% neutron capture efficiencies would be attainable at a thickness of 14.5 μm [14]. Planar conversion layer detectors are limited to efficiencies of ~4% due to neutron absorption effects. Non planar geometries, such as pinhole and vias, relax this constraint somewhat, resulting in calculated efficiencies of 20-30% , depending on aspect ratio [15]. However, these more complex geometries require a concomitant increase in the complexity of construction. Unlike planar conversion layer detectors calculated neutron capture efficiencies in boron carbide based diodes scale with thickness; however, the overall detection efficiency is highly dependent on the charge capture efficiency in *both* semiconductors. As the thickness of the boron carbide layer is increased, the semiconducting properties of the boron carbide layer assume increased importance.

This fundamental difference between the two types of detectors leads to differing efficiencies, pulse height signatures and detection thresholds as shown both in GEANT4 Monte Carlo simulations [16] and a simple physical model [14, 16]. There is a clear distinction between a true solid state boron carbide neutron detector, in which the boron carbide layer is capable of both neutron absorption and charge capture, and conversion layer detectors. There are two striking differences—the models indicate that for a boron carbide/Si diode, the energy deposition

spectra are weighted to higher energies, with a cut-off below the lowest energy signature at 0.84 MeV, whereas in the boron carbide conversion layer, the pulse height spectra are weighted towards lower energies with a cut-off at the highest energy of 1.78 MeV. In both cases, a thickness of 1 μm boron carbide leads to a substantial smearing of the individual peaks associated with the He and Li ions. In addition, in the case of the diode detector, sum peaks at the energies of the *sum* of the Li and He ion should be present, an effect absent in the case of a conversion layer detector since charge capture and neutron capture occur in two different layers. Both predictions are modified in the presence of electronic and statistical noise and both depend on the assumption of 100% charge capture, an assumption we will show is highly dependent on the parameters of the associated processing electronics and the properties of the semiconductor.

In *thin* boron carbide/thick Si heterojunctions, much of the charge capture occurs in the Si layer due to geometrical constraints, and hence the neutron detection signatures are very similar to those of conversion layer detectors. In the earliest successful solid state neutron detector, a 276 nm thick film of boron carbide formed a diode with n-type Si [9], leading to a neutron detection efficiency of 5×10^{-5}, much lower than the expected neutron detection efficiency of 1.3×10^{-3}. Subsequent measurements on a 232 nm thick $B_5C_1H_2$/n-type Si heterojunction diode [2] resulted in a much improved efficiency of 3.35×10^{-3} even at zero applied bias—almost exactly equal to the calculated neutron capture efficiency. We attribute this higher efficiency to the improved semiconducting properties of the boron carbide that allow for more efficient charge capture. The effect of increasing the bias led to small increases in the detection efficiency of less than 10%, leading to the conclusion that such a large amount of charge is liberated on neutron capture that capturing even small fractions of it leads to a charge pulse above threshold noise [2]. Subsequent efforts on neutron detection in boron carbide/Si

heterojunction diodes have focused on the parameters important for increased efficiency. Although increasing the thickness of the boron carbide layer must increase the neutron capture rate, the entire process from neutron capture to charge collection (in both the boron carbide and the Si) and the subsequent pulse processing are found to play important roles in the overall detection efficiency.

In this manuscript, we describe neutron detection experiments on 640 nm boron carbide on n-type Si. This increase in thickness over previous samples leads to a greater proportion of charge being captured in the semiconducting boron carbide layer. As expected, the properties of the boron carbide play a much larger role in the neutron detection efficiencies. As we demonstrate below, the charge pulse risetime is governed by the characteristics of the semiconducting material and is substantially different for the two materials. Both the applied bias voltage and the integration time constants are shown to lead to much improved detection efficiencies.

The neutron capture reaction in the boron carbide/Si heterojunction detector for thermal neutrons is described in equation (7.1) and illustrated in figure 7.1. Neutron capture occurs *only* in the p-type boron carbide side, with the neutron capture site serving as the origin for highly energetic Li and He ions. Electron-hole pairs are generated by the passage of these secondary ions through the semiconductor. The signal at either electrode arises mainly from charges generated within the depletion layer. The charge carriers are accelerated due to the internal electric field, with negative (positive) charge drifting towards the positive (negative) electrode. Depending on the ground and center conductor connection of the coaxial cable, the charge pulse consists either of electrons (from the Si side) or holes (from the $B_5C_1H_2$ side). Hence the charge pulse we collect consists of only one type of charge. Since the mobility of carriers on the boron

carbide and Si side differ vastly, the choice of time constants has a significant impact on the charge collection and, consequently on the neutron detection efficiency. We will show that there is a significant difference in the signal, depending on whether electrons or holes are collected at the center conductor.

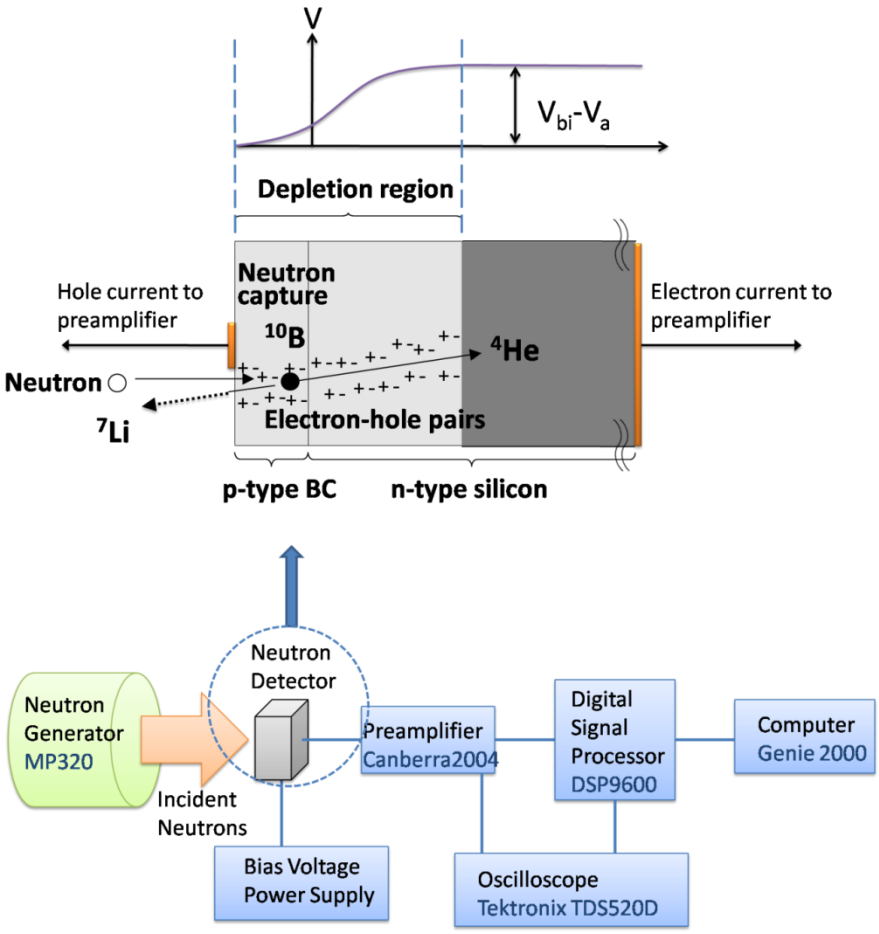

Figure 7. 1(Top) A neutron capture event in a boron carbide ($B_5C_1H_2$)/Si heterojunction diode detector. (Diagram not to scale) The boron carbide film is fully depleted at 0 V. Increased bias leads to an increase in the depletion width on the Si side. The neutron is captured in the boron carbide layer, resulting in ^{4}He and ^{7}Li ions, which move in opposite directions, generating electron-hole pairs on both sides of the junction. The charge sensitive preamplifier may be connected to either side of the junction, collecting either a hole or an electron current. (Bottom) Schematic diagram of the neutron detection system used showing the associated electronics. Oscilloscope traces taken directly after the preamplifier are dominated by the risetime associated with charge capture within the semiconductor whereas oscilloscope traces taken after the DSP show a convolution of the risetime with the selected time constant.

7.2 Experimental details

The 640 nm boron carbide layers were grown on n-type Si (111) substrates (resistivity ~100 Ωcm) using PECVD from an orthcarborane closo-1,2-dicarbadodecaborane ($C_2B_{10}H_{12}$) precursor [17] in a custom designed parallel plate 13.56 MHz rf PECVD reactor [1]. The base pressure was 4×10^{-7} torr and the working pressure was 200 mtorr Ar gas. The substrate temperature was held at 330 ℃ during deposition with 30 W rf-power supplied. The film growth rate, 80 nm/10 min., was deduced using ex situ grazing incidence x-ray reflectivity. Elastic recoil detection analysis (ERDA) showed the boron carbide film composition to be $B_5C_1H_2$.

Ohmic contacts for $B_5C_1H_2$ and Si layers were sputter-deposited using Cr and Au metal targets [1] with contact areas ranging in size from 0.785 to 19.625 mm^2 on the $B_5C_1H_2$ side. The Si side contacts covered the entire area of the chip, ~ 1 cm^2. The p-n diode showed the built-in potential, V_{bi} = 0.7 V determined by the first derivatives of current-voltage (I-V) curves on the selected area at room temperature. A capacitance-voltage (C-V) curve (Chapter 5, Figure 5.3) confirmed the same turn on voltage at the same condition. V_{bi} is a measure of the Fermi level in the two semiconductors [18] and the unchanging turn-on voltage (reproduced numerous times) confirms the reproducibility of the PECVD growth process for $B_5C_1H_2$.

The neutron source used was a Thermo Electron Corporation MP320 [19], operated to generate a flux of 1.0×10^8 n/s 14 MeV neutrons. Moderation was effected using a 10 cm thick beryllium block followed by 8 cm of paraffin wax. A coaxial cable connected the detector to a Canberra 2004 charge-to voltage preamplifier and subsequently to a Canberra Digital Signal Processor (DSP 9600) for pulse counting. The outer shield of the coaxial cable was grounded and connected to either the p or n side of the junction. The scope traces were obtained on a Tektronix TDS520D oscilloscope. Three different trapezoidal time constant filters were used to

process the signal from the preamplifier. Background measurements were obtained using a 0.025 mm Cd foil, as a thermal neutron shield [20]. All experiments with and without Cd foil were performed under identical conditions of neutron flux and applied bias, to obtain the most reliable measurement of background.

7. 3 Results and discussion

A typical I-V curve for the p-type $B_5C_1H_2$/n-type Si heterojunction diode is shown in figure 7.2. The low leakage currents are crucial in suppressing the noise peak and enabling the detection of neutron capture signals. The combination of low leakage current and large reverse breakdown voltage (> 20V) allow for the application of large bias voltages without significant increases in the noise level. This enhancement of the device properties for neutron detection was accomplished by use of more stable plasma control, low-doped (100 Ωcm) Si wafers, and thick $B_5C_1H_2$ deposits. The 640 nm $B_5C_1H_2$ layer with a contact area of 3.14 mm^2 and a leakage current of 0.244 μA, (corresponding to a current density of 3.4 $\mu A/cm^2$) at an applied bias of -19 V shows about 500 times decrease in the leakage current compared to the thin boron carbide diode used in previous work [2].

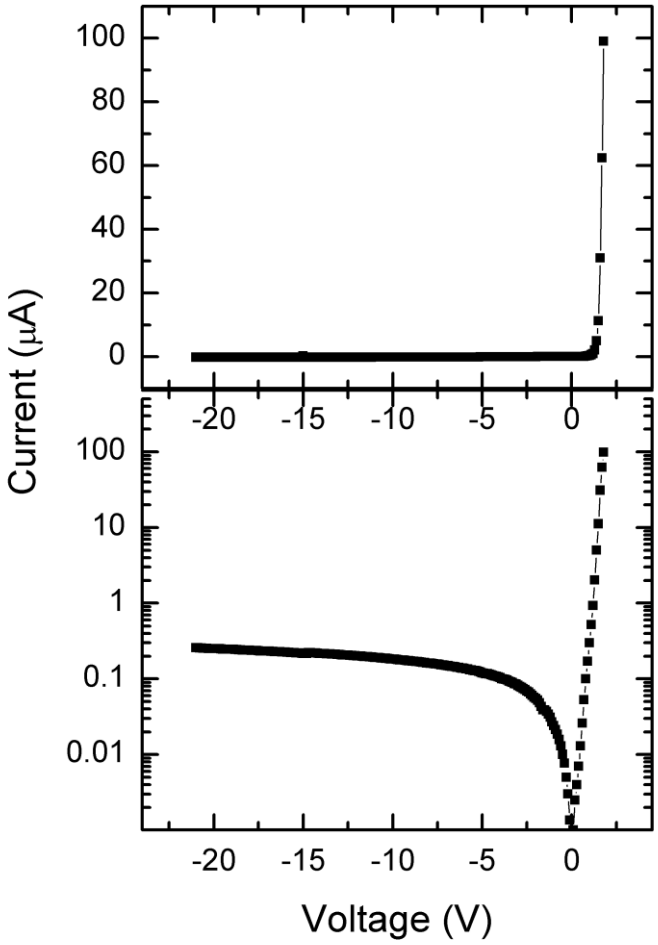

Figure 7. 2 I-V curves of the 640nm $B_5C_1H_2$/Si heterojunction diode at room temperature in linear (top) and log (bottom) scales. The built-in voltage is 0.7 V.

In a diode detector, the active region for charge capture is the depletion region, where charge recombination is highly suppressed. The depletion region thickness increases with increasing reverse bias as expected, as was shown in the C-V measurement in Chapter 5, with a $1/\sqrt{V}$ dependence expected for a step junction [21]. The C-V curve indicates that the device is not entirely depleted over the range of reverse bias used for neutron detection measurements

(from 0 to -19 V). The calculated doping density (in Chapter 5) of 4.5×10^{12} cm^{-3} in $B_5C_1H_2$, corresponds to a depletion width of 10 μm at zero bias—well above the thickness of the $B_5C_1H_2$ film. Hence, over the entire bias range, the $B_5C_1H_2$ is always fully depleted. Application of a reverse bias leads to an increase of the depletion width on the Si side of the heterojunction, as well as increasing the internal electric field, both of which have implications for charge collection. Previous measurements of the resistivity of boron carbide range from 10^8 to 10^{10} Ωcm imply a mobility ranging from 10^{-4} to 10^{-2} cm^2/Vs, many orders of magnitude lower than the mobility of the n-type Si (1400 cm^2/Vs). This substantially lower mobility has a pronounced effect on charge capture efficiency.

Neutron detection pulse height spectra with and without Cd foil are shown in figures 7.3 and 7.4 as functions of applied bias and integration time constants respectively. All data shown in these figures were collected from the Si n-type side of the heterojunction diode, with the $B_5C_1H_2$ side grounded, and hence correspond to electron collection. Four bias voltages (figure 7.3) using the longest time constant with rise and fall times of 28 μs and a flat top time of 3.0 μs, and three different trapezoidal time constants (figure 7.4) at a fixed bias voltage are shown. The details of the trapezoidal time constants are indicated in figure 7.4 (right-hand side).

The pulse height spectra for the 640 nm $B_5C_1H_2$ diode detector show three peaks, corresponding to the 0.84 MeV ^{7}Li ions (first peak), 1.47 MeV ^{4}He ions (second peak), and 1.78 MeV ^{4}He ions (much smaller third peak). At 0 V, part of the 0.84 MeV peak is subsumed within the noise peak but is clearly discernible at an applied reverse bias of 10 V. The low intensity of the 1.78 MeV peak arises from the much lower probability (6%) of the reaction generating the 1.78 MeV He ions. A peak from the 1.02 MeV ^{7}Li ions is not distinguishable within our energy resolution but may be embedded within the first peak.

With increasing applied bias, the pulse height spectrum broadens and shifts to higher channel numbers—an effect also seen in earlier work on thinner detectors [2]. The secondary ions produced as a result of neutron capture within the $B_5C_1H_2$ layer are emitted with equal probability in all directions. Momentum conservation dictates that the He and Li ion travel initially in opposite directions, as shown in figure 7.1. These ions have path lengths of a few μm in both the boron carbide and the Si (the path lengths are not identical), and hence the amount of energy lost by the ions within the diode varies from a minimum which occurs when the ions are emitted normal to the film plane to a maximum which occurs when the ions are emitted parallel to the plane of the sample. The capture product energy loss corresponds to the number of electron-hole pairs produced and; of these, the electron-hole pairs produced in the depletion region are available for charge collection. An increase in the applied bias results in increases in both the depletion width and the internal electric field. Both will lead to a greater fraction of charge being collected from the electron-hole pairs produced by the highly energetic ions. The increase in the depletion width allows for collection over a larger region and increases in the internal electric field accelerate the charges, resulting in less charge trapping and recombination. The broadening of the pulse may be explained by considering the range of possible angles that lead to a charge collection signal. At low bias and small depletion widths, charge is only collected from ions that are emitted almost parallel to the sample plane, since, compared to ions emitted at angles close to the normal, these ions lose a larger fraction of their energy within the depletion layer. At larger depletion widths, charge may be collected from a much larger range of solid angles, resulting in a larger range of energies deposited and collected, leading to a broadening of the energy deposition peaks.

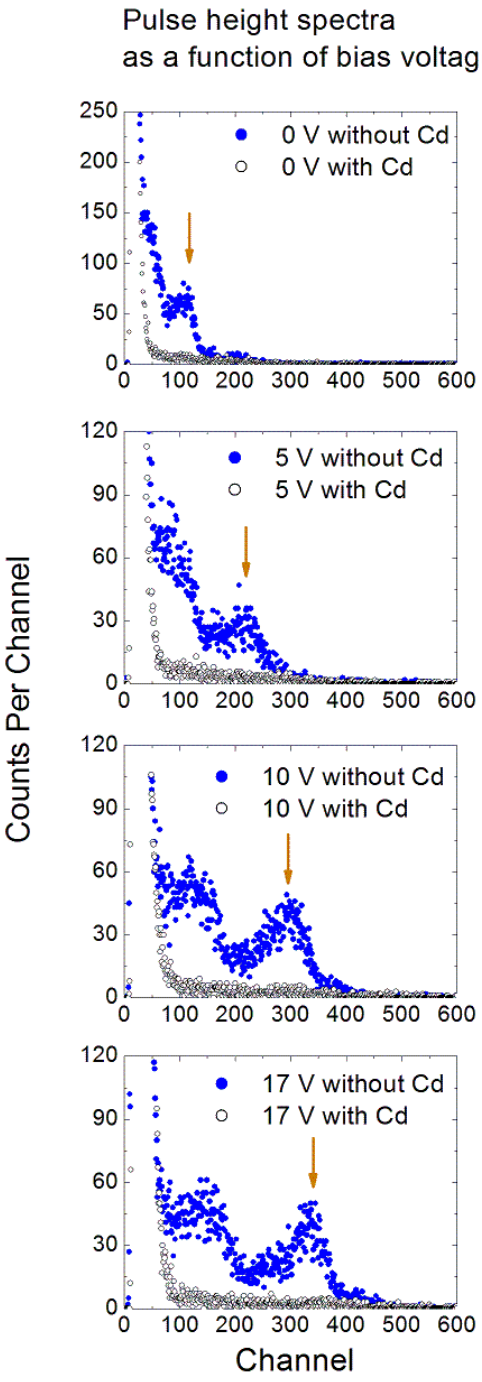

Figure 7. 3 Pulse height spectra as a function of reverse bias voltage with (o) and without (•) Cd foil on the 640 nm $B_5C_1H_2$/Si heterojunction detector, both with a trapezoidal time constant with rise and fall times of 28 μs and a flat top time of 3.0 μs. Four different bias voltages are shown. As the bias increases, the channel numbers for each peak increase due to the longer depletion width and resulting increase in charge collection. The broadening of these peaks with increased bias is due to the larger solid angle over which charge may be collected as the depletion width increases.

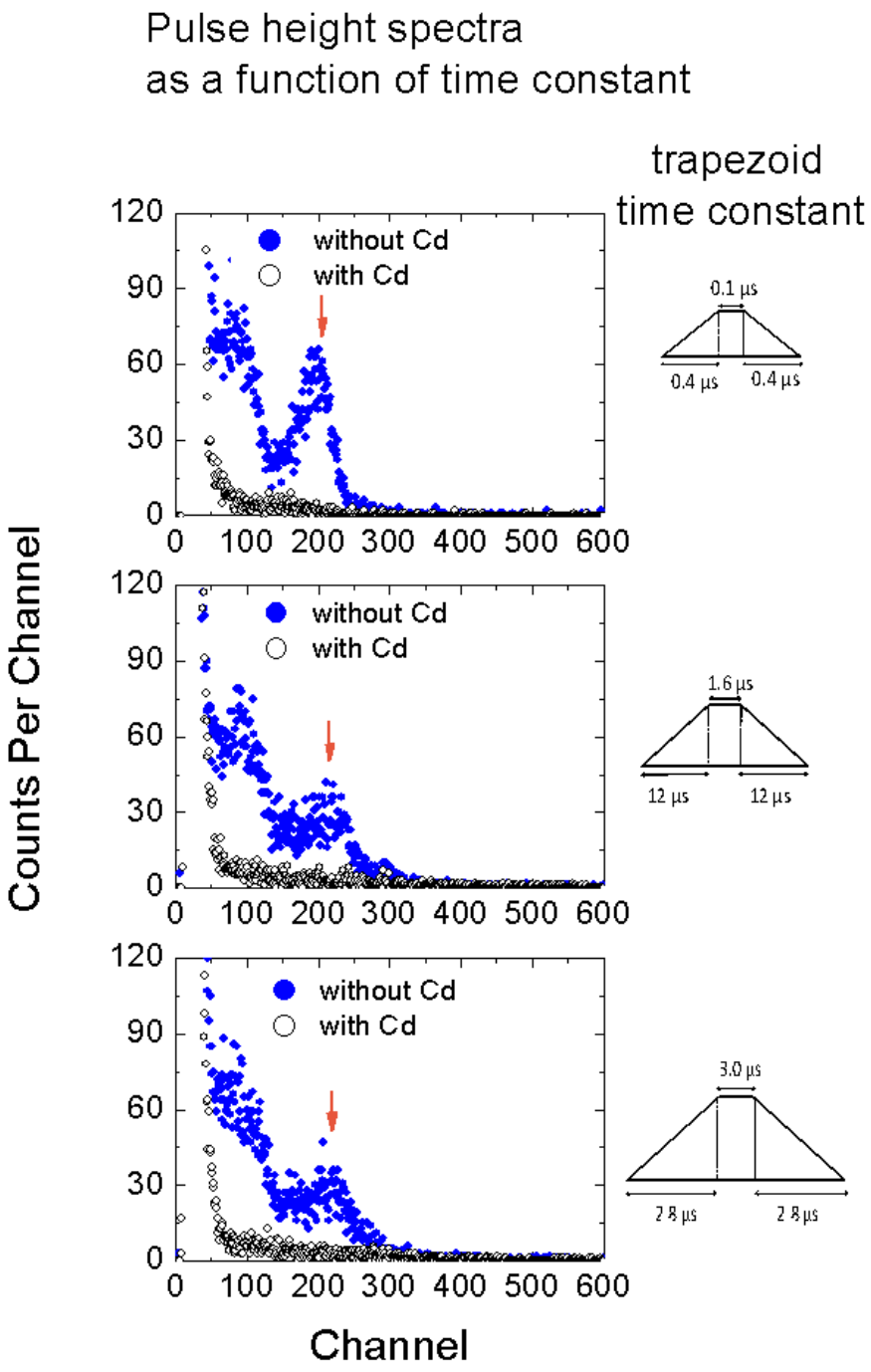

Figure 7. 4 Pulse height spectra as a function of time constant with (o) and without (•) Cd foil on the 640 nm $B_5C_1H_2$/Si heterojunction detector at 5 V reverse bias. Right-hand side figures depict the shape of the trapezoidal time constants for each case.

A quantitative measure of the shift in the pulse height spectra with increasing bias may be obtained by using the second peak. A plot of the peak position versus the applied bias (figure 7.5) shows a $\sqrt{V}$ dependence, similar to that of the C-V curve, further suggesting that, as the depletion width (or reverse bias) increases, the fraction of charge collected increases proportionately. The peak position approaches, but does not reach, saturation even at 20 V and, since the device is not entirely depleted, we may assume that applying still higher bias voltages would lead to increased charge collection. Because the range of the He ion in Si is ~5 μm [20] and because all ions must originate in the $B_5C_1H_2$ layer, increasing the depletion width beyond 5 μm in Si (reached at a bias voltage of 2.3 V) should lead to no further increase in the charge collection. The increases in peak position at biases > 2.3 V must result from increased acceleration of charge on both sides of the junction.

However, as will be discussed in figure 7.8, this does not correspond to increases in efficiency. Unlike in solid state gamma and x-ray detectors [20], the positions of the peaks in the $B_5C_1H_2$/Si pulse height spectra provide no information about the neutron energy and energy resolution is not important; rather, it is the intrinsic efficiency that must be maximized. For a particular neutron capture event, incomplete charge capture will still lead to a neutron count provided the signal to noise ratio is large enough.

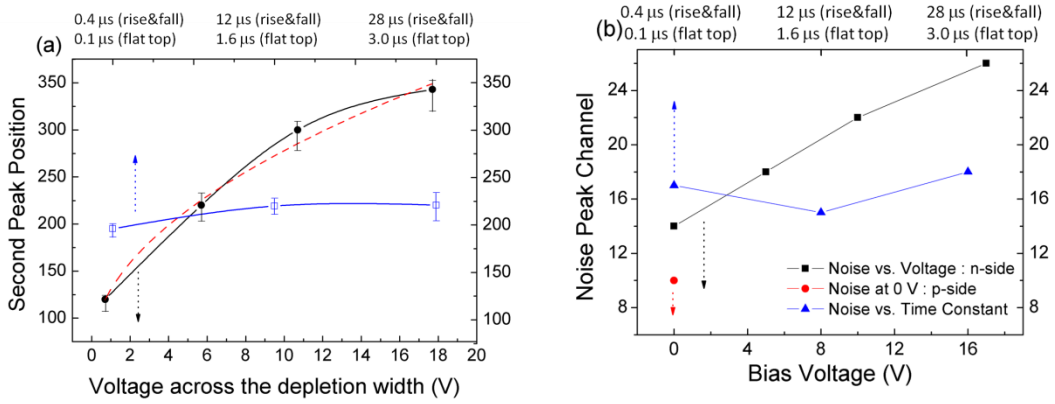

Figure 7. 5 (a) The channel number of the peak assigned to the 1.47 MeV ^{4}He ion in the 640 nm $B_5C_1H_2$/Si heterojunction diode detector as a function of bias voltage (filled circles), and time constant (unfilled squares). The channel number corresponds to the size of the collected charge pulse and increases with applied bias. The dashed curve is a $\sqrt{V}$ fit, indicating that the increase in channel number (and charge capture) is proportional to the depletion width. Charge collection increases in going from the rise and fall times of 0.4 µs and the flat top time of 0.1 µs time constant to the rise and fall times of 12 µs and the flat top time of 1.6 µs time constant and saturates thereafter, as expected from the ~20 µs risetime of charge in the $B_5C_1H_2$ layer. (b) The noise peak channel as a function of bias voltage (squares) and time constant (triangles) with charge signal obtained from the n-side. The noise channel is linear with bias voltage, similar to the leakage current, and independent of the time constant. Hence, increases in signal-to-noise are best achieved by increasing the time constant. The noise peak at 0 V for collection from the p-side of the diode is also shown (red circle) and is significantly lower.

The time constant of the digital signal processor has a pronounced effect on the pulse height spectra and the neutron detection efficiency, showing higher efficiency at larger time constant. With increased time constant, the peaks become broader and shift to (slightly) higher channel number, implying that longer time constants permit larger fractions of the charge to contribute to the pulse height spectra. The effect is most pronounced on changing from the shortest time constant with rise and fall times of 0.4 µs and a flat top time of 0.1 µs to rise and fall times of 12 µs and a flat top time of 1.6 µs time constant. This is consistent with earlier observations of a long rise time of ~20 µs for charge pulses within the $B_5C_1H_2$ layer [2], compared to the < 20 ns rise time for the signal from the Si layer. This large difference in

risetimes presents an obstacle to obtaining ideal efficiencies because the signal processor we used (in common with other commercially available processors) may not recognize the long slow risetime signal from the $B_5C_1H_2$ as a peak when this signal follows the short risetime Si-sourced signal, thereby ignoring the energy deposited in the $B_5C_1H_2$.

These effects of the processing time constants are well described using both mathematical convolutions of the time constant with a model charge pulse as well as scope traces from the output of the DSP (see figure 7.6). Since the output signal from the DSP is a time convolution of the trapezoidal weighting function and the peaks from the $B_5C_1H_2$ and Si layers, the peak voltage for the integrated charge pulse determines the channel in the pulse height spectrum and the values of the time constant are key in determining this peak voltage. A time constant much shorter than the signal will lead to a deficiency in the peak voltage and may result in a signal that is subsumed in the noise channels, whereas too long of a time constant will lead to a flat top in the DSP output and a subsequent saturation of the signal.

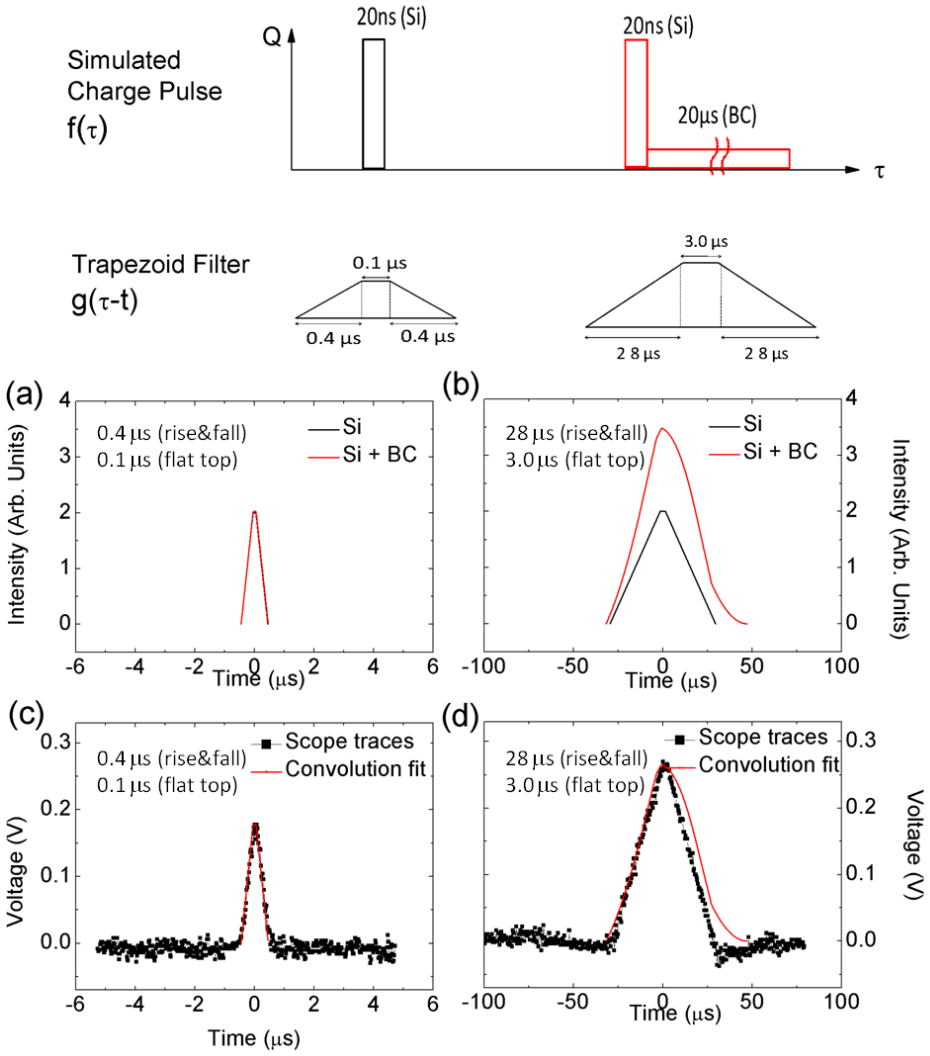

Figure 7. 6 (from top to bottom) Two simulated charge pulses, one using a short rise time of 20 ns (as seen in Si) and the other using two risetimes, one of 20 ns (for Si) and 20 μs (for $B_5C_1H_2$). The two trapezoidal time constants are illustrated in the second row. Outputs of the convolution integral between the charge pulse and the filter are shown in (a) and (b). Note that the y-axis, albeit in arbitrary units, is the same for (a) and (b); hence the heights may be directly compared. Convolutions of the Si peak and the ($B_5C_1H_2$+Si) peak with the short time constant overlap exactly, since the short time constant ignores the contribution of the 20 μs signal. The convolution using the long time constant with the (Si+ $B_5C_1H_2$) pulse (red line in figure (b)) results in a higher voltage peak. Two scope traces taken from the same sample using the same reverse bias voltage of 5 V are shown in (c) and (d). The trace on the left is taken using a short time constant (rise and fall times of 0.4 μs and a flat top time of 0.1 μs) and the trace on the right a long time constant (rise and fall times of 28 μs and a flat top time of 3.0 μs). It should be noted that the time over which charge is collected is increased in the figure on the right. The convolution curves of (a) and (b) are scaled for height and then overlaid on the scope traces indicating excellent agreement.

A MATLAB [22] simulation, in which rectangular pulses with time durations corresponding to the expected charge collection times in the Si (20 ns) and $B_5C_1H_2$ (20 μs) layers respectively are mathematically convoluted with the appropriate time constants, is shown in figure 7.6(a) and (b). The area under each rectangular pulse is assumed to be the same, corresponding to equal amounts of total charge collected, an assumption we will show later to be erroneous. Black and red lines indicate the results of the convolution of the charge pulse from Si and from (Si+ $B_5C_1H_2$), respectively. The short 20 ns pulse from Si results in a voltage peak independent of the time filter, since the pulse duration is much shorter than the shortest time constant. The longer 20 μs pulse shows a significant (~75%) enhancement in the voltage peak with increased time constant. This simulation is for a particular *single* pulse in which the same amount of charge is liberated and collected in both the Si and the $B_5C_1H_2$. The pulse height spectra are histograms of a large number of events that record the frequency of occurrence of the entire range of differing charge pulse heights, originating from $B_5C_1H_2$ and Si. In general, for a single event, the charge pulses in the $B_5C_1H_2$ and the Si are of different heights. However, it is reasonable to assume that on average the same amount of charge is generated in both, albeit with some small differences due to the differing path lengths of the ions and the depletion width in each. With longer time constants and the resulting improved charge collection form the $B_5C_1H_2$ side, the entire pulse height spectra should be shifted to higher channel number by 75%—the same amount seen for a single pulse, but this is not the case.

Scope traces of charge pulses taken after the DSP are shown in figure 7.6(c) and (d), using the short (rise and fall times of 0.4 μs and a flat top time of 0.1 μs) and long (rise and fall times of 28 μs and a flat top time of 3.0 μs) trapezoidal filters respectively with the same applied bias of 5 V. The output signals from the DSP are processed using the chosen trapezoidal filter,

allowing for an investigation of the effect of the time constant directly from these scope traces. An overlay of the convolution integral on the corresponding scope traces indicate excellent agreement as a function of time, the voltage heights having been scaled to match as shown in figure 7.6. Hence, the discrepancy between the expected 75% increase in channel number and the experimentally obtained 13% increase must result from incomplete charge capture, most likely from the $B_5C_1H_2$ side. Since the entire calculated increase results wholly from the signal in the $B_5C_1H_2$ layer, a simple calculation indicates that the 13% increase in channel number implies that at most 20% of the charge generated in the $B_5C_1H_2$ layer is captured. Impurities and structural defects in the PECVD deposited $B_5C_1H_2$, which is at best an imperfect crystal [18], hamper the charge transport process, trapping charge carriers into deep impurity levels and/or recombination centers leading to a loss of charge carriers [20].

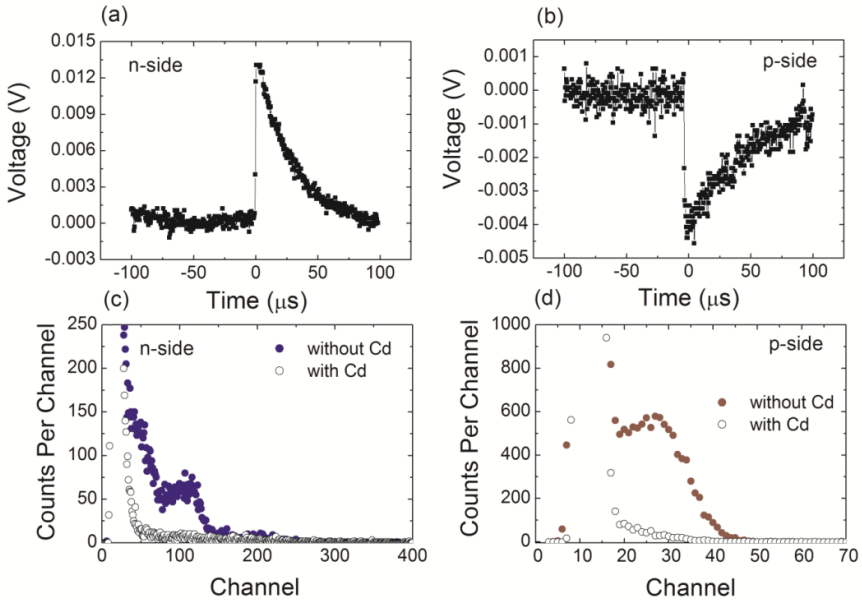

Figure 7. 7 Scope traces at the output of the preamplifier from (a) electron signals (from the n-type Si) and (b) hole signals (from the p-type $B_5C_1H_2$). (c) and (d) Pulse height spectra for the 640 nm $B_5C_1H_2$/n-Si detector with the center conductor connected to the n-side (c) and the p-side (d) of the diode. All data shown are at 0 V bias using the longest time constant. The efficiency for neutron detection using signals from the p-side is 0.63 %, a 21% increase in efficiency compared to an efficiency of 0.52 % for the n-side.

The disparate charge collection times and efficiencies are also relevant in any discussion of the expected sum peak. The position of the sum peak in the pulse height spectra obtained from the Si side is complicated by the much lower charge collection from the $B_5C_1H_2$ semiconductor. A simple analysis of the sum peak for the more probable neutron capture reaction shows that the peak will deviate substantially from its expected position. Assuming that only 20% of the charge liberated by the He and Li ions is captured within the $B_5C_1H_2$ layer, the sum peak position, rather than lying at the channel corresponding to 2.31 MeV, will instead be spread over channels ranging from a low of 0.46 MeV (well below the first Li peak energy and occurring for the rare event in which both ions are captured within the $B_5C_1H_2$ layer) to a high of 1.64 MeV (for neutron capture events at the $B_5C_1H_2$/Si boundary in which the He ion traverses only the Si layer and the Li ion traverses the $B_5C_1H_2$ layer). The substantial broadening and lowering of energy make it impossible to definitively identify the sum peak in the pulse height spectra. Any evidence of the sum peak will only be present as higher energy tailing of the He peak and is subsumed within the less probable 1.78 MeV ^{4}He peak.

The pulse height spectrum for charge (hole) capture on the p-type $B_5C_1H_2$ side is shown in figure 7.7, together with oscilloscope traces, at 0 V applied bias. Two striking differences are apparent when compared to electron collection from the Si side of the junction. The noise and signal peak are shifted to lower channel number (corresponding to lower voltage pulse heights), and are extremely narrow. Correspondingly, the number of counts in the signal channel is significantly higher, with a peak height of ~600 counts (as compared to ~175 and 75 for the Li and He peaks respectively for charge collected from the Si side). The lowered noise level arises from better grounding on the Si side due to the higher conductivity of Si as compared to $B_5C_1H_2$.

The neutron detection signal is peaked at channel 28, much lower than either the He or Li peak identified in the pulse height spectra collected from the Si side, a consequence of the loss of charge carriers within the $B_5C_1H_2$ layer. The identification of the peak is not simple. Assigning it to the 1.47 MeV ^{4}He peak, the peak position at channel 28 (compared to the peak position of channel 120 for collection on the Si side) is consistent with the low fraction of charge (20%) that we estimate for collection at the $B_5C_1H_2$ side electrode. However, the 0.63% efficiency obtained is anomalously high, as in this scenario all signal from the Li ion is buried within the noise peak. If, instead, the peak is assigned to overlapping Li and He peaks, then the increased efficiency from the $B_5C_1H_2$ side compared to the Si side may be attributed to the lower noise level and hence the greater collection counts associated with the lower energy Li peak. In fact, the separation of the signal peak from the noise is similar to that seen for the much higher bias voltage of 10 V (figure 7.3(b)) for charge collection on the Si side and the efficiency is similar for these cases—0.63% at 0 V for p-side and 0.65% at 10 V for n-side. The width of the peak, < 40 channels, is significantly lower than for charge collection on the Si side (> 200 channels). This is because, for charge collection on the Si side, charge that is generated in the $B_5C_1H_2$ layer is severely attenuated by charge trapping and recombination, before reaching the Si layer, whereas the charge generated by the passage of ions through the Si layer is barely attenuated. Hence the charge collected is distributed over a large range of channels, with the lowest channel number corresponding to charge production almost entirely within the $B_5C_1H_2$ layer and the highest channel number corresponding to charge production almost entirely within the Si layer. For collection on the $B_5C_1H_2$ side, however, all charges, whether generated in the $B_5C_1H_2$ or Si layer, must pass through the $B_5C_1H_2$ layer, being severely attenuated by charge capture and recombination. Hence, the spread in the charge pulse heights is small.

The effects of increased bias voltage and time constant are summarized in figure 7.5 and 7.8. Figure 7.5 shows the channel number shift with applied bias and time constant. Increased bias voltages shift both the signal and noise peaks to higher channel number, limiting the efficiency attainable using increased bias. Increasing the time constant has no effect on the noise peak position, but does cause a small increase in the signal channel number, that saturates at rise and fall times of 12 μs and a flat top time of 1.8 μs time constant.

The ideal efficiency for a normally incident neutron beam with a room temperature Maxwell-Boltzmann distribution may be calculated from

$$\text{Detection efficiency} = 1 - \mathrm{e}^{-\left(\sigma^{\text{eff}}\,(\text{R.T.})\rho l\right)} \tag{7.2}$$

where $\sigma^{\text{eff}}(\text{R.T.})$ is the effective absorption cross section of ^{10}B averaged over a room temperature Maxwell-Boltzmann distribution, ρ is the number density of ^{10}B in the boron carbide material, and *l* is the thickness of the neutron capture layer**.** For a 640 nm thick layer of, with elemental composition $B_5C_1H_2$, the neutron detection efficiency (assuming all captured neutrons give rise to a measureable signal) is 0.474%. However, because the neutron source is moderated and uncollimated after moderation, we expect the neutron beam to be isotropic. This has also been experimentally verified by tests we carried out on the source with a ^{3}He neutron detector as shown in Chapter 6. For an isotropic neutron beam, the expression for the neutron detection efficiency is

$$\text{Detection efficiency for an isotropic neutrons} = 2\int_0^{\theta_{\max}} \left[1 - \mathrm{e}^{-\left(\frac{\sigma^{\text{eff}}\,(\text{R.T.})\rho l}{\cos\theta}\right)}\right] \sin\theta \mathrm{d}\theta \tag{7.3}$$

where the limits range from $\vartheta = 0$ to a maximum that is given by $\cos^{-1}$(height/width). A numerical integration using Maple 13 gives an expected efficiency of 5.4%.

The commercial ^{3}He neutron detector is calibrated only for normal incidence neutrons. A similar calculation as given above for isotropic neutrons is complicated by the depth of the ^{3}He detector, necessitating a point-by-point calculation over the entire surface. Instead, we base our efficiency numbers on the experiments described in Chapter 8 in which we obtain close to ideal efficiency for normal incident neutrons in a well-calibrated beam. The data in Chapter 8 were obtained at a bias voltage of -17 V with a time constant of rise and fall times of 28 μs and a flat top time of 3.0 μs. Hence we normalize our efficiency to these conditions and set the efficiency to 5.4% at these conditions.

The neutron detection counts were obtained as functions of bias and time constants by taking the difference between the total integrated detected counts with and without Cd foil above a chosen channel number (depending on the noise signal) and are shown in figure 7.8. Below ~10 V, increases in applied bias lead to marked increases in the neutron detection efficiency. Above this value, there is little change in the efficiency although the pulse height spectra indicate increased charge collection since, as long as each neutron capture event leads to sufficient charge collection (i.e. above the noise level), further increases in charge collection lead to no increase in efficiency. At 0 V, the depletion width in the Si is 2.45 μm, comparable to the (totally depleted) 640 nm thickness of the $B_5C_1H_2$ and a greater fraction of the charge will arise from the $B_5C_1H_2$ layer, traveling through the depleted $B_5C_1H_2$ and into the Si. Hence, at this low bias, the effect of increased time constant is most pronounced, and arises from the greater fraction of charge with the slow risetime associated with the low mobility of charges within the $B_5C_1H_2$ layer. As the bias increases, depletion on the Si side increases and leads to more efficient charge capture in the Si.

The average time interval between consecutive incident neutrons for our experiments is 0.01 s. The sum of the rise and decay times for charge generation and capture is less than 0.0001s for a single neutron capture event. Therefore, at ~5% detection efficiency, the average time interval between successive incident neutrons is 2 orders of magnitude larger than the time duration of the voltage pulse from a single neutron detection event (based on Poisson statistics) making pulse pile-up highly improbable. The detector showed no degradation in neutron detection efficiency over a period of 15 months.

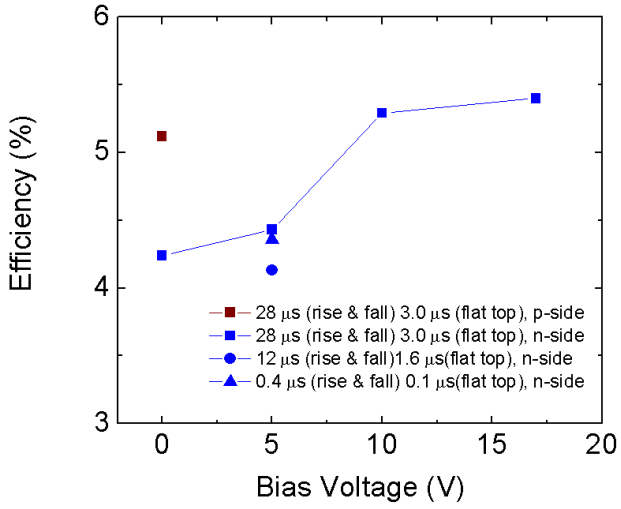

Figure 7. 8 Neutron detection efficiencies as a function of bias voltage and time constant obtained from either the p-type $B_5C_1H_2$ layer or the n-type Si layer.

7.4 Conclusions

The parameters necessary for the efficient operation of the solid state 640 nm $B_5C_1H_2$/Si neutron detector have been investigated. The novelty of such a detector requires the development of a fundamental understanding of their operation since it differs from that of other detectors. This work investigated the effects of the disparate semiconducting properties, of electronic and statistical noise, and the effects of the above on the pulse height spectra and

efficiency on $B_5C_1H_2$ layers that are much thicker than previously tested. Excellent diode characteristics with low reverse bias current and much higher breakdown voltages facilitate sensitive neutron detection.

The lightly doped $B_5C_1H_2$ layer is fully depleted even at zero bias and so operation at zero bias is feasible, albeit with somewhat reduced efficiency. Increased bias voltages lead to increased charge collection, shifting the peak in the pulse height spectra to higher channel number. At low bias, the effects of increased time constant are most pronounced due to the short depletion width on the Si side and the low mobility of charge carriers in $B_5C_1H_2$. This effect of greatly enhanced efficiency with a longer time constant is the strongest evidence to date of charge collection occurring in the $B_5C_1H_2$ layer. If charge collection were occurring only in Si, increasing the time constant would have no effect because the charge pulse risetime in Si is of the order of < 20 ns. Neutron detection signatures from both the n-doped Si side and the p-doped $B_5C_1H_2$ side have been observed and the observed spectra from the $B_5C_1H_2$ side are consistent with the incomplete charge capture that we deduce from the behavior of the pulse height spectra with increasing time constant. A surprising feature is the greatly enhanced neutron detection efficiency for detection on the p-side of the junction, which we attribute to the lower noise due to better grounding on the Si side.

The efficiency of neutron detection will be greatly improved by decreasing noise and increasing the charge collection fraction within the $B_5C_1H_2$ layer—a function of its semiconducting properties. Recent investigations of the effects of growth temperature, in-situ annealing and in-situ sputtering of the substrate are encouraging. Our data clearly show that even at this much lower charge collection efficiency, highly efficient neutron detection in all $B_5C_1H_2$ detectors is possible, provided the noise level is adequately low.

REFERENCES

1. Adenwalla, S., et al., *Boron carbide/n-silicon carbide heterojunction diodes.* Applied Physics Letters, 2001. **79**(26): p. 4357-4359.
2. Day, E., M.J. Diaz, and S. Adenwalla, *Effect of bias on neutron detection in thin semiconducting boron carbide films.* Journal of Physics D: Applied Physics, 2006. **39**(14): p. 2920.
3. Ahmad, A.A., et al., *Sputter deposition of high resistivity boron carbide.* Thin Solid Films, 1998. **335**: p. 174-177.
4. Byun, D., et al., *Heterojunction fabrication by selective area chemical vapor deposition induced by synchrotron radiation.* Applied Physics Letters, 1994. **64**(15): p. 1968-1970.
5. Lee, S., et al., *Characterization of boron carbide thin films fabricated by plasma enhanced chemical vapor deposition from boranes.* Journal of Applied Physics, 1992. **72**(10): p. 4925-4933.
6. Hwang, S., et al., *Nickel doping of boron carbide grown by plasma enhanced chemical vapor deposition.* Journal of Vacuum Science & Technology B: Microelectronics and Nanometer Structures, 1996. **14**(4): p. 2957-2960.
7. Hwang, S., et al., *Fabrication of n-type nickel doped B_5C_1 homojunction and heterojunction diodes.* Applied Physics Letters, 1997. **70**(8): p. 1028-1030.
8. McIlroy, D.N., et al., *The incorporation of Nickel and Phosphorus dopants into Boron-Carbon alloy thin films.* Applied Physics A: Materials Science & Processing, 1998. **67**(3): p. 335-342.
9. Robertson, B.W., et al., *A class of boron-rich solid-state neutron detectors.* Applied Physics Letters, 2002. **80**(19): p. 3644-3646.

10. Mireshghi, A., et al., *High efficiency neutron sensitive amorphous silicon pixel detectors.* Nuclear Science, IEEE Transactions on, 1994. **41**(4): p. 915-921.

11. Seshadri, S., et al., *Demonstration of an SiC neutron detector for high-radiation environments.* Electron Devices, IEEE Transactions on, 1999. **46**(3): p. 567-571.

12. McGregor, D.S., et al., *Design considerations for thin film coated semiconductor thermal neutron detectors: basics regarding alpha particle emitting neutron reactive films.* Nuclear Instruments and Methods in Physics Research Section A: Accelerators, Spectrometers, Detectors and Associated Equipment, 2003. **500**: p. 272-308.

13. Schmid, G.J., et al., *CVD diamond as a high bandwidth neutron detector for inertial confinement fusion diagnostics.* Review of Scientific Instruments, 2003. **74**(3): p. 1828-1831.

14. Harken, A.D. and B.W. Robertson, *Comparative modelling of performance limits of solid-state neutron detectors based on planar B-rich capture layers.* Journal of Physics D: Applied Physics, 2006. **39**(23): p. 4961.

15. Shultis, J.K. and D.S. McGregor, *Design and performance considerations for perforated semiconductor thermal-neutron detectors.* Nuclear Instruments and Methods in Physics Research A, 2009. **606**: p. 608.

16. Lundstedt, C., et al., *Modeling solid-state boron carbide low energy neutron detectors.* Nuclear Instruments and Methods in Physics Research Section A: Accelerators, Spectrometers, Detectors and Associated Equipment, 2006. **562**(1): p. 380-388.

17. *Sigma-Aldrich, http://www.sigmaaldrich.com.*

18. Hong, N., et al., *Ni doping of semiconducting boron carbide.* Journal of Applied Physics, 2010. **107**(2): p. 024513.

19. *Thermo Scientific, http://www.thermoscientific.com.*

20. Knoll, G.F., *Radiation detection and measurement*. 2nd ed. 1989, New York: Wiley.

21. Sze, S.M., *Semiconductor Devices Physics and Technology*. 2nd ed. 2002: New York: Wiley.

22. *The Math Works, http://www.mathworks.com.*

Chapter 8 Time-Of-Flight Neutron Detection Using PECVD Grown Boron Carbide Diode Detector

Part of the work reported in this chapter on TOF neutron detection was performed in collaboration with L. Crow of Neutron Facilities Development Division, Oak Ridge National Laboratory, Oak Ridge, TN, U.S.A. The optical microscopic image was performed in collaboration with Anil K. Rajapitamahuni of Department of Physics & Astronomy, University of Nebraska-Lincoln, Lincoln, NE, U.S.A.

8.1 Introduction

In this chapter, I describe an experimental measurement of the neutron detection efficiency of semiconducting boron carbide neutron detectors using time-of-flight (TOF) experiments at a well-calibrated, non-monochromatic, normal incident cold neutron beam source. Both the absolute efficiency and the wavelength dependence of the efficiency are investigated. Because efficiency measurements are often plagued by uncertainties regarding the incident neutron flux and wavelength distribution, this work provides an excellent benchmark for two important questions that will affect the ultimate use of these materials as neutron detectors, viz. the experimentally attainable efficiencies and the wavelength dependence of the efficiency. In particular, the experimental neutron detection efficiency as a function of wavelength has not been investigated in solid-state neutron detectors.

Additional motivation for this work comes from the impending shortage of ^{3}He, as discussed in Chapter 6. Because special nuclear materials (SNM) radiate over a wide range of neutron energies and, because moderation of those neutrons will result in a thermal distribution of neutron energies, it is imperative that the efficiencies of solid state neutron detectors are

shown to follow the expected wavelength dependent efficiency, if they are to be used for the detection of SNM.

8.2 Experimental details

640 nm thick boron carbide films were deposited on n-type Si (111) substrates (resistivity ~100 Ωcm) at 200 mTorr Ar gas ambient pressure by plasma-enhanced chemical vapor deposition (PECVD) at a substrate temperature of 330 ℃ [1]. Orthocarborane closo-1,2-dicarbadodecaborane ($C_2B_{10}H_{12}$) [2], carried by 90 ℃ Ar gas, was used as a source molecule. The source was not enriched in ^{10}B, resulting in thin films with the naturally occurring 19.6% fraction of ^{10}B. Elastic recoil detection analysis (ERDA) results show that the boron to carbon ratio of the source molecule is well preserved in the deposited boron carbide film and the hydrogen concentration is dramatically reduced, leading to an elemental composition of $B_5C_1H_2$. The material density of 2.463 g/cc was determined from the critical angle observed in x-ray reflectivity (XRR) measurements. The p-n diode properties of the p-type $B_5C_1H_2$ on the n-type Si detectors have been measured [1] using current-voltage and capacitance-voltage measurements.

Neutron detection experiments were performed on the CG1D beam, a single chopper TOF system, on the High Flux Isotope Reactor (HFIR) at Oak Ridge National Laboratory (ORNL) [3]. The neutron beam has a square profile of 4.1 cm by 4.1 cm at the selected detector position and was monitored by a divergence-mapping neutron camera during the entire measurement process. A nitrogen (N_2) monitor (manufactured by ORDELA, Oak Ridge, TN) with a measured efficiency of 1.01×10^{-5} at 1.8 Å was placed behind the $B_5C_1H_2$ diode detector to obtain the incident neutron beam spectrum. There is a negligible loss of neutrons within the $B_5C_1H_2$ detector because of its small thickness and low efficiency. Neutron detection signatures

from the $B_5C_1H_2$ detector were monitored by TOF techniques and a multichannel analyzer, respectively for one hour. The details of the electronics and data acquisition for pulse height spectra have been described in Chapter 7. All data within the $B_5C_1H_2$ detector reported here were measured at room temperature with a reverse bias of 17 V.

A cold "white" beam of incident neutrons, moderated by a hydrogen moderator cooled to 20 K, and transported through a curved guide with a 1.8 Å cut-off, was incident on a 40 Hz chopper. The chopper opening was 2 degrees, leading to an open time of 139 μs. The neutron wavelengths were sorted by TOF techniques, with faster, short wavelength neutrons arriving first at the detector. Both the N_2 detector and boron carbide detector TOF measurements were performed for one hour, accumulating 144,000 passes with a time bin width of 0.025 ms. The bin width implies a wavelength resolution of 0.03305 Å over a wavelength range from 1.8 Å to 20.01 Å. The Bragg edges that arise from scattering off the Al in the beam path result in notches in the continuous spectrum and were used for wavelength calibration of the TOF neutrons [3, 4]. Note that the absorption cross sections for both ^{10}B and ^{14}N scale with wavelength and that this dependence must be taken into account when analyzing the detector TOF signal.

8.3 Results and discussion

Figure 8.1 (a) illustrates the incident neutron flux as a function of wavelength, obtained by the TOF data on the N_2 detector after correction for the linear dependence of the absorption cross section as a function of wavelength. For ^{14}N [5], this dependence is given by $\sigma = 1.02\lambda$ where σ is the absorption cross section in barns and λ is the neutron wavelength in Å. The two notches at 4.048 Å and 4.676 Å match the aluminum (200) and (111) diffraction peaks. The shape of the spectrum is determined by the Maxwell-Boltzmann distribution for neutrons in thermal equilibrium with the hydrogen moderator [6] and is given by Eq. (1)

$$dn = n(\lambda)d\lambda = -4\pi n_0 \left(\frac{m_n}{2\pi kT}\right)^{\frac{3}{2}} \left(\frac{h^3}{{m_n}^3\lambda^4}\right) \exp\left(-\frac{h^2}{2kT\,m_n\lambda^2}\right) d\lambda \quad (1)$$

where n_0 is the total number of neutrons per cm^3, T is the moderator temperature, and k the Boltzmann constant. The red line in figure 8.1 is a Maxwell-Boltzmann fit for the incident neutron beam spectrum (black line). The best fit for the data measured on the N_2 detector is obtained for a moderator temperature of 49.40 K. The TOF experiment on the 640 nm thick $B_5C_1H_2$ detector shown in figure 8.1(b) was performed concurrently with that on the N_2 detector. Here too, the measured response has been normalized by the wavelength dependent absorption cross section for ^{10}B, given by $\sigma = 2137\lambda$ [5]. A noise discriminator level was set high enough to eliminate possible noise signals for the 640 nm detector, resulting in the smooth curve seen in figure 8.1. The Maxwell-Boltzmann best fit for this detector shows an effective moderator temperature of 57.16 K. The best fits for both detectors show a significantly higher moderator temperature than 20K, an effect that is not unexpected. Thermal hardening effects, consisting of the preferential capture of lower energy neutrons in the material along the beam path, together with a steady influx of high energy fission neutrons in the reactor, will result in a preferential weighting to the higher energy side of the spectrum. Secondly, the thermal moderator behind the cold source in the HB-4 beamtube (see figure 1 of Ref. [7] for the four horizontal beamtubes at the HFIR core assembly) contributes to the intensity of neutrons entering the guide [7]. Thirdly, the hydrogen moderator is relatively thin and this leads to a slightly elevated effective moderator temperature because the moderation is incomplete. All three factors generate effectively "warmer" neutrons. In addition, the curved guide which cuts off the spectrum at about 1.8 Å could modify the observed spectrum to lower effective temperatures. This cut-off is clearly visible in figure 8.1.

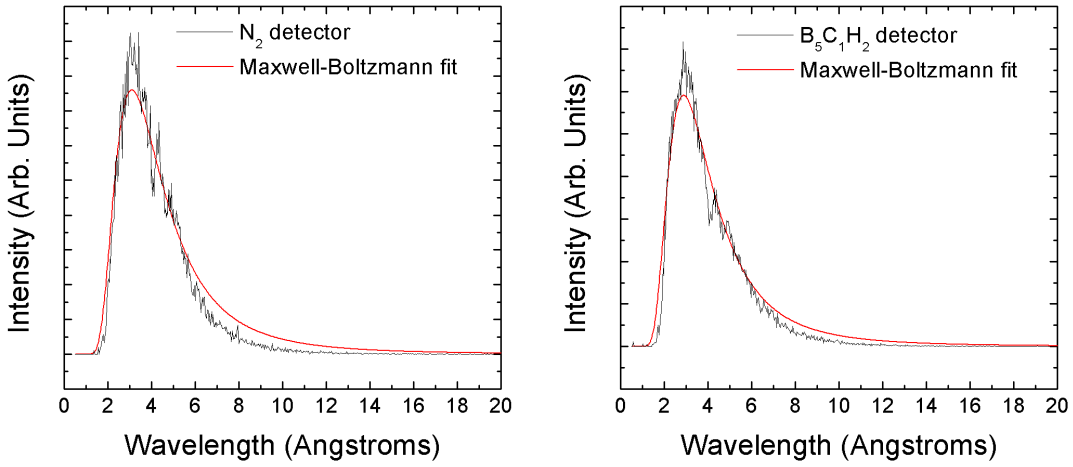

Figure 8. 1 Wavelength distribution of the incoming neutron flux from the CG1D beam source (black line) and the fit to the Maxwell-Boltzmann distribution (red line) as expressed in equation (6.3) obtained from TOF measurements on the N_2 detector (left) and the $B_5C_1H_2$ detector (right). The wavelength dependence of the absorption cross section for each detector has been taken into account so that the TOF curves represent the incoming neutron profile as a function of wavelength.

The calibrated N_2 detector and boron carbide detector were placed in the beam path and monitored simultaneously so as to obtain an accurate measure of the incident beam flux in real time. However, the small path length difference between the two resulted in air attenuation and so in a slightly attenuated beam for the N_2 detector. Although air attenuation effects were expected to be small, the low efficiency of the N_2 detector (and the fact that it contains the major gaseous constituent of air) necessitate a calculation of the air attenuation. We calculated the air attenuation with the help of Dr. Lowell Crow at ORNL.

Air attenuation is sensitive to atmospheric conditions that determine the vapor pressure of water in air. The model for this calculation used 1) a temperature of 25 ℃ (room temperature), 2) a barometric pressure at 760 mmHg (standard atmosphere), and 3) a dew point at 10 ℃ (checked against the weather conditions when the experiment was conducted). The gases included in the model calculation were N_2, O_2, CO_2, Ar, Ne, He, Kr, Xe, H_2, CH_4, N_2O, and H_2O.

The distance between the two detectors was 31.4 cm, which was calculated from the time-to-wavelength conversion. Figure 8.2 shows a plot of the air transmission as a function of wavelength under the above atmospheric conditions along the 31.4 cm pathway. Longer wavelengths are attenuated more, causing a deformation of the neutron spectrum incident on the N_2 detector as compared to that incident on the $B_5C_1H_2$ detector.

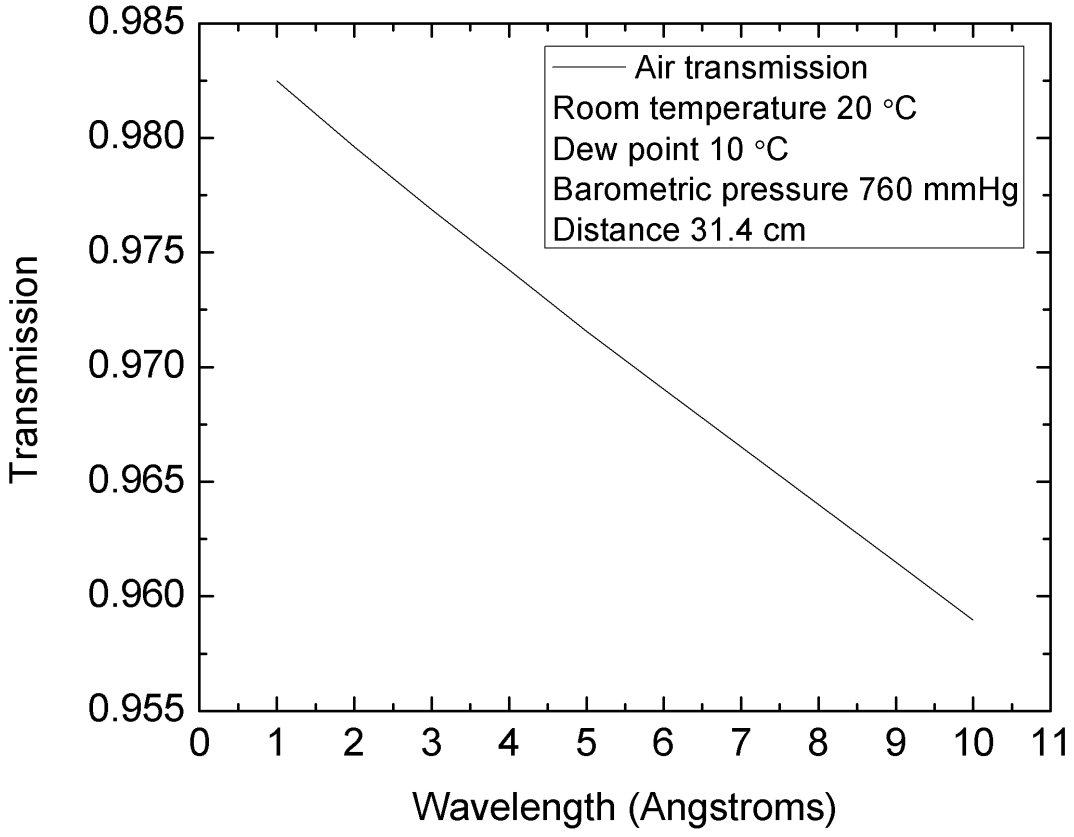

Figure 8. 2 Air transmission as a function of wavelength calculated based on the weather conditions when the TOF experiment was performed.

With the data shown in figure 8.2, we could construct a new spectrum for the N_2 detector, taking air attenuation into account. This spectrum, shown in figure 8.3, is the incoming neutron spectra incident on the $B_5C_1H_2$ detector, and is the spectral response that we would expect if the N_2 detector were at the same position in the beam path as the $B_5C_1H_2$ detector. Figure 8.3 compares the TOF results for the N_2 detector with (red line) and without (black line) air attenuation. The spectrum after air attenuation is taken into account shows a small enhancement of the longer wavelengths (as expected from the transmission versus wavelength plot in figure 8.2) and a slightly lower moderator temperature of 47.20 K.

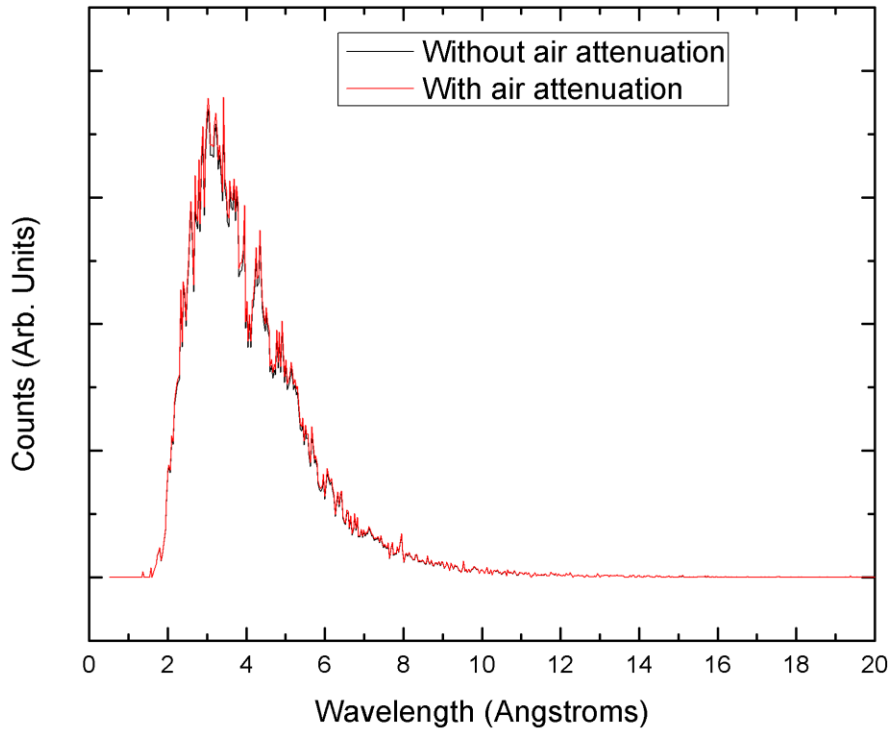

Figure 8. 3 A comparison of the TOF spectrum of the N_2 detector without air attenuation (black line) and after taking into account air attenuation between the two detectors (red line).

The overall shapes of the two TOF spectra for the two detectors are overlapped in figure 8.4. The spectrum from the $B_5C_1H_2$ detector is shifted to slightly lower wavelengths by about 0.40 Å , an effect that could arise from uncertainty in the wavelength caused by the bin size of 0.025 ms as well as from inaccuracies in the positions of the Al Bragg edges due to insufficient statistics. The close agreement between the two spectra in figure 8.4 is an important step in confirming that the $B_5C_1H_2$ diode detectors show the expected neutron detection behavior over this range of wavelengths and are suitable as beam monitors.

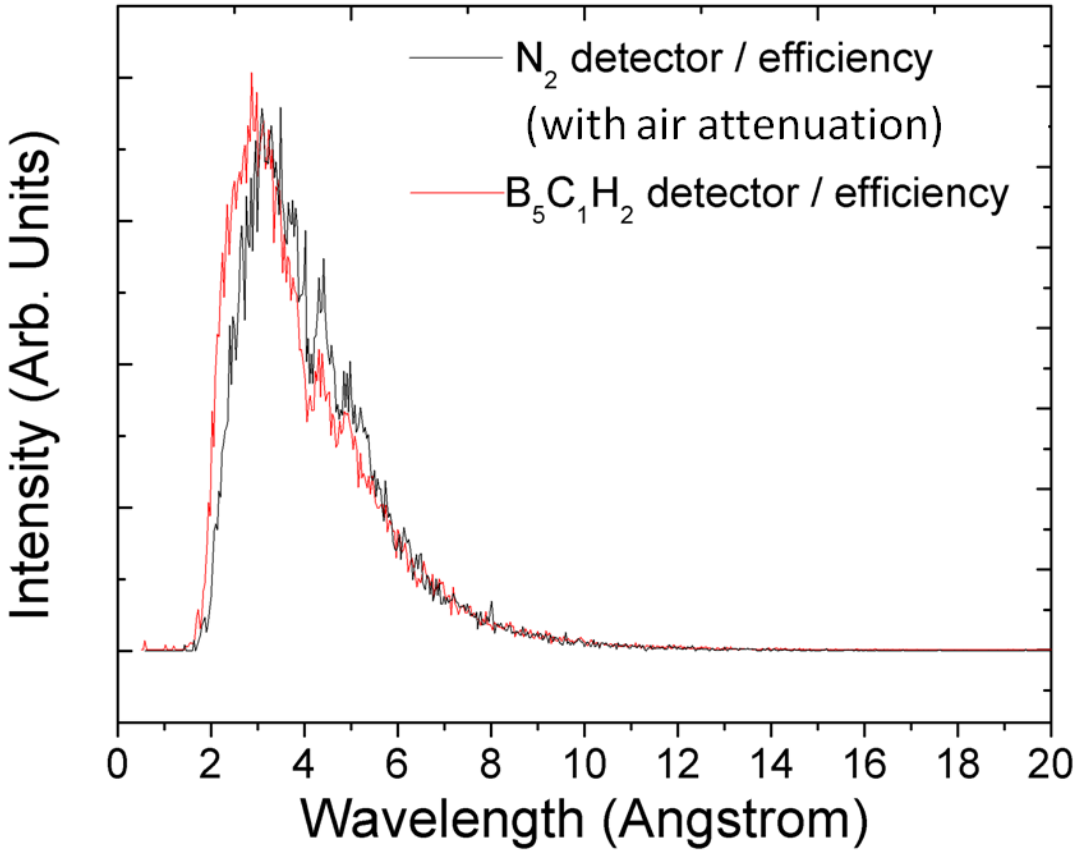

Figure 8. 4 A comparison of the two TOF spectra for the N_2 and $B_5C_1H_2$ detector scaled by wavelength dependent efficiency.

The results of the wavelength dependence of the neutron capture efficiency of the $B_5C_1H_2$ and the calibrated N_2 detector allow us to make an accurate measure of the efficiency of the $B_5C_1H_2$ detector. Shown in figure 8.5 is the pulse height spectrum of the 640 nm $B_5C_1H_2$ detector, indicating the number of neutrons captured at each channel number. The applied reverse bias of 17 V and the integration trapezoidal time constant with rise and fall times of 28 μs and a flat top time of 3.0 μs have been shown in previous work [1] to result in optimal charge collection and hence efficiency for the $B_5C_1H_2$/Si detectors. The peaks in the pulse height spectrum correspond to ^{7}Li (0.84 MeV) and ^{4}He (1.47 MeV). The total number of neutrons incident on the 3.14 mm^2 active area in the measurement time of 1 hour is 3,110,772, which is calculated from the wavelength distribution of the incoming neutrons shown in figure 8.4. At low channel numbers, the signal is dominated by noise, as shown by the green line, measured in an identical experiment with the neutron beam off. Because the noise is zero for all channel numbers > 31, the measured neutron efficiency of 1.25% with a cut-off at channel 32 (the green line) is an excellent *lower* limit for the efficiency. Calculations of the neutron detection over the entire spectral range require appropriate weighting factors for each wavelength. For a Maxwell Boltzmann distribution at a temperature T, the effective absorption cross section is given by $\frac{1}{1.128}\left(\frac{293\ K}{T}\right)^{1/2}\sigma^{th}$, where σ^{th} is the absorption cross section at a temperature of 293 K (0.0253 eV) [8]. Using the Maxwell-Boltzmann distribution at a temperature of 57.16 K, we obtain an effective absorption cross section of 7710 barns. The corresponding neutron capture efficiency over the entire range of wavelengths for the 640 nm $B_5C_1H_2$ detector is ~1.07%.

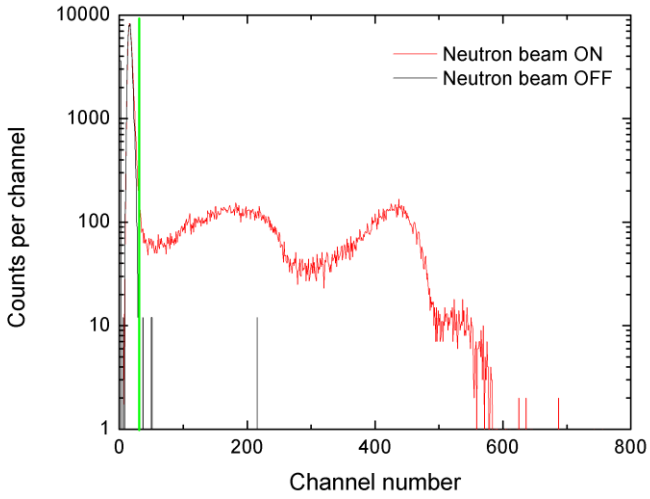

Figure 8. 5 The pulse height spectrum where the neutron beam was ON (red) or OFF (black). The green line indicates the noise cut-off line (channel number 32) for the calculation of neutron detection efficiency.

What are the possible uncertainties in our efficiency measurements and calculations? Because we have simultaneous monitoring of the neutron spectra from the N_2 detector, we can rule out fluctuations in the beam intensity. The apparent spectral shift to higher energies seen in the spectrum of the $B_5C_1H_2$ detector could lead to slightly lower estimates of efficiency. If instead, we used the spectrum obtained at the N_2 detector, the calculated efficiency would correspond to a Maxwell Boltzmann distribution corresponding to a temperature of 47.20 K and would be higher, 1.12 %. Geometric effects, such as the angle of the detector with respect to the beam direction, the collimation of the beam and the accuracy with which we can measure the area of the electrode also contribute to the uncertainty in the measurements. We consider each effect individually: The neutron beam divergence has been measured to be $<1^0$ [9]. This slight divergence over the detector area would increase the path length of neutrons within the boron carbide layer by less than 0.001%, resulting in no detectable change in the neutron detection

efficiency. Imperfect alignment of the detector with respect to the beam would result in angle variations at most of $\pm 3^0$, resulting in a slightly higher path length and less than 1% increase in the calculated neutron detection efficiency (i.e. from ~1% to 1.01%). The area measurement of the electrode, however, has considerable uncertainty. The nominal 1mm radius is obtained from the dimensions of the shadow mask used for deposition of the electrode but there are notable shadowing effects, which may increase the electrode area significantly. This uncertainty in the electrode area results in a corresponding uncertainty in the number of incident neutrons. From measurements using an optical microscope, we obtain an electrode radius of 1±0.07 mm leading to an uncertainty in the area of ~±0.31 mm^2. This leads to an uncertainty of 307,114 in the number of incident neutrons resulting in an experimental neutron detection efficiency which ranges from 1.14% to 1.39%. This range of the measured efficiency is consistent with the calculated neutron detection efficiency for the 47 K Maxwell-Boltzmann distribution.

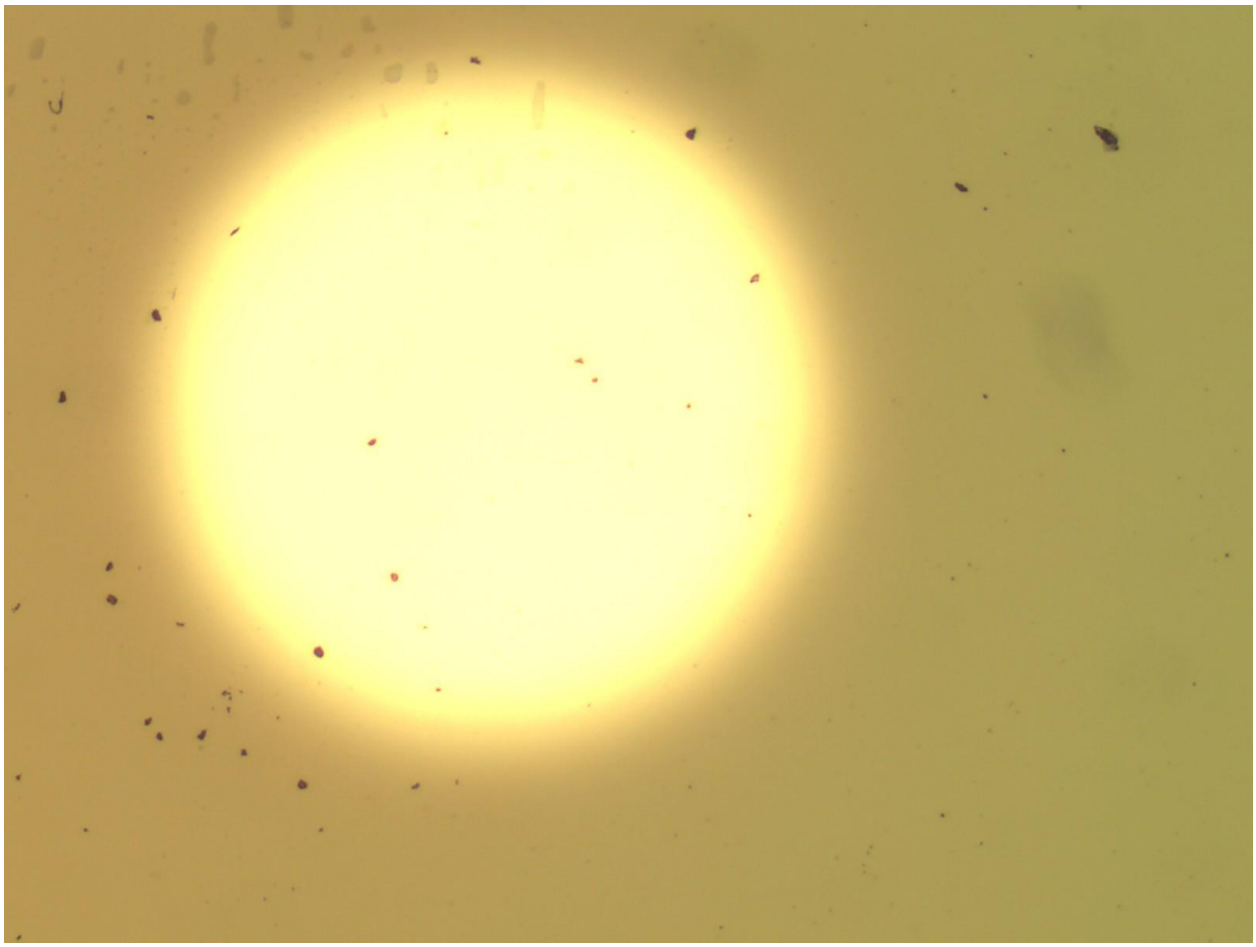

Figure 8. 6 An optical image of an electrode with its radius of 1 mm.

In conclusion, we have measured a Maxwell-Boltzmann neutron spectrum in an all solid state neutron detector that shows excellent agreement with a known calibrated N_2 detector. Because the neutron source is collimated and well calibrated we are able to obtain an accurate experimental neutron detection efficiency which ranges from 1.14% to 1.39% showing a good agreement with the calculated neutron detection efficiency for a Maxwell-Boltzmann distribution at a temperature of 47 K.

REFERENCES

1. Hong, N., et al., *Boron carbide based solid state neutron detectors: the effects of bias and time constant on detection efficiency.* Journal of Physics D: Applied Physics, 2010. **43**(27): p. 275101.
2. *Sigma-Aldrich, http://www.sigmaaldrich.com.*
3. Crow, L., et al., *The CG1 instrument development test station at the high flux isotope reactor.* Nuclear Instruments and Methods in Physics Research Section A: Accelerators, Spectrometers, Detectors and Associated Equipment, 2011. **634**: p. S71-S74.
4. Lorusso, G., et al., *Time-energy relation of the n_TOF neutron beam: energy standards revisited.* Nuclear Instruments and Methods in Physics Research Section A: Accelerators, Spectrometers, Detectors and Associated Equipment, 2004. **532**(3): p. 622-630.
5. *ENDF: Evaluated Nuclear Data File, http://www.nndc.bnl.gov/exfor/endf.htm.*
6. Liverhant, S.E., *Elementary introduction to nuclear reactor physics*. 1960, New York,: Wiley.
7. Robertson, J.I. and E.B. Iverson, *Measurement of the neutron spectrum of the HB-4 cold source at the High Flux Isotope Reactor at Oak Ridge National Laboratory.* Proceedings of the 13th International Symposium on Reactor Dosimetry, Akersloot, Netherlands, May 2008, World Scientific Publishing Co., Singapore, 2009: p. 85-93.
8. *Radiation Detection and Nuclear Instrumentation Laboratory, http://inst.nuc.berkeley.edu/NE104/.*
9. Moon, R., *Final design and Performance of Cold Guide Systems.* ORNL internal report, 2001.

Chapter 9 GEANT4 Simulations of the Pulse Height Spectra and Neutron Detection Efficiencies of Solid State Boron Carbide Neutron Detectors: Dependence on Semiconducting Properties

Part of the work reported in this chapter was performed with Michael K. Chu of Department of Physics, University of California, San Diego La Jolla, CA, U.S.A.

9.1 Introduction

Neutron detectors play an important role in national security applications, in oil well logging, as nuclear reactor monitors, and in the basic science of neutron scattering experiments. The gold standard neutron detector is based on gaseous ^{3}He, and offers high sensitivity, low false positives and high gamma blindness. The advantages of solid state radiation detectors compared to gas-filled detectors lie in the much higher density of neutron absorbing material, potentially resulting in a dramatic reduction in the needed volume. The use of semiconducting materials as radiation detectors can result in a significant number of charge carriers (in the form of electron-hole pairs) that are generated during the radiation detection process, thus enabling efficient detection well above the noise. Semiconductor diode detectors, such as Schottky diodes with semiconductor-metal contacts, p-n diodes, and p-i-n diodes, can operate at low (and even zero) applied bias voltages because the built in potential in the depletion region will sweep the charges out to the electrodes.

The ability to make a semiconductor with a large neutron absorption cross section is key to the development of an all solid state neutron detector, because this enables neutron capture, charge production and charge capture within a single material. Plasma enhanced chemical vapor deposition of boron carbide results in a semiconducting material with proven neutron detection

capabilities [1-6]. In Chapter 7 (taken from Ref. [2]) , we show that the operating parameters of reverse bias voltage, the time constants for integration and the choice of the collection electrode in boron carbide/Si p-n diode detectors influence the shape of the pulse height spectrum and the neutron detection efficiency. Electronic noise will alter [7-9] the pulse height spectrum, by broadening the peaks. Charge collection efficiency variations in the boron carbide [10] will also significantly alter the pulse height spectrum, and indirectly the neutron detection efficiency.

Here we simulate the neutron pulse height spectrum using a Monte Carlo simulation, GEANT4 (Geometry ANd Tracking [11, 12]) for boron carbide/n-type Si p-n diode detectors under a variety of operating conditions. Although this simulation is confined to boron carbide/n-type Si diode neutron detectors, our simulation provides insight into the distortion of pulse height spectra for other types of detectors (for example, using different materials). We vary the charge collection efficiencies to predict the neutron detection efficiencies as well as the expected shape of the pulse height spectra.

For the GEANT4 simulations, the detector geometry (see figure 9.1) is chosen to closely approximate the detectors we fabricate. The detector is a cylinder of radius 1 mm, with a 1μm thick film of unenriched $B_5C_1H_2$ on a Si substrate of standard thickness 381 μm. The stoichiometry and the density are obtained from previous ion beam analysis and x-ray reflectivity experiments respectively. A monoenergetic thermal neutron beam at 0.025 eV is incident normally upon the surface. Using GEANT4, we 1) track the secondary ions in the p-n diode in terms of energy and position and 2) obtain the number of neutron captures for a fixed number of incident neutrons. A simple script using Perl [13] is used to parse the outputs of the GEANT4 results in order to plot pulse height spectra. This allows for convenient application of specific mathematical functions to the tracks of the secondary ions by writing the script instead of

running a separate GEANT4 simulation. For example, the effect of electronic noise can be simulated by convoluting the noise free spectrum with a Gaussian function of a given width. The effect of incomplete charge collection efficiency can be simulated by multiplying a weighting function with the tracks of the secondary ions. The energy, flux, angular and spatial dependence of the neutron flux are generated using the General Particle Source (GPS, GEANT4 class name: G4GeneralParticleSource).

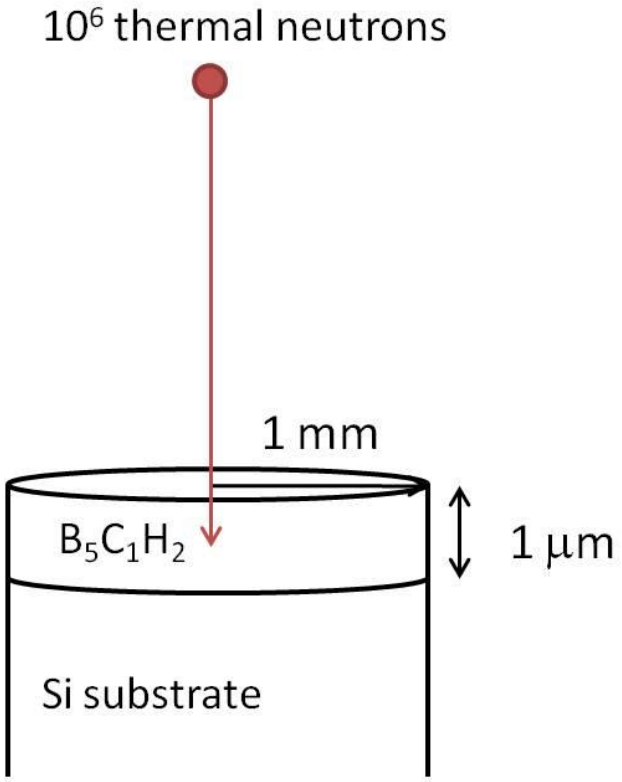

Figure 9. 1 The geometry used in GEANT4 simulations for active and conversion layer detectors. The metal electrodes are not shown and the drawing is not to scale.

9.2 Comparison of active layer and conversion layer detectors

For purposes of comparison, we first modeled ideal detectors—both an active layer and a conversion layer on Si. These have been modeled previously using a simple physical model [14], GEANT4 simulations [7], and a simple Monte Carlo procedure [15] and indicate clear differences in the pulse height spectra and efficiencies in these two cases. The ^{10}B neutron capture reaction is given by,

(94%) $^{10}B + n \rightarrow {}^{7}Li\ (0.84\ MeV) + {}^{4}He\ (1.47\ MeV) + \gamma\ (0.48\ MeV)$

(6%) $^{10}B + n \rightarrow {}^{7}Li\ (1.02\ MeV) + {}^{4}He\ (1.78\ MeV)$ (9.1)

The highly energetic Li and He ions have equal and opposite momentum and lose energy as they move through the material. As before, we define an active layer to be one in which both neutron *and* charge capture occur, as would be the case for a ^{10}B rich semiconductor, with the energetic Li and He ions produced in the $B_5C_1H_2$ layer leading to the production and sweep out of electron hole pairs within the $B_5C_1H_2$ layer as well as in the Si. In contrast, in a single-sided planar conversion layer detector, one layer (in this case a passive $B_5C_1H_2$ layer with the same density) captures neutrons while charge production and capture occur in an adjacent semiconductor layer, which usually consists of an additional diode device (p-n or p-i-n) or a Schottky junction. In our model of the conversion layer detector, the fully depleted Si plays the role of an electrically active region for the generation and sweep out of electron-hole pairs. In both cases, we have made the following assumptions of ideal behavior: (i) 100% charge collection efficiency in the Si layer (ii) The depletion width in the Si is greater than the longest range of the capture product ions and (iii) electronic noise is zero. In the case of the active layer, additional assumptions include (i) the ionization energy to generate an electron-hole pair in both

layers is the same and is 3.62 eV and (ii) the charge collection efficiency in the $B_5C_1H_2$ layer is also 100%.

Under these assumptions, the GEANT4 simulation of the pulse height spectra for an active layer and a conversion layer are shown in figure 9.2, with the Li and He energy peaks clearly visible. In common with earlier results, the spectra display two striking differences that are a direct consequence of the ability (or lack of ability) of the neutron capture layer to capture charge. The individual Li and He peaks show high energy tailing for the active layer, and low energy tailing for the conversion layer, an effect that is most apparent below 0.84 MeV, the energy of the lowest energy ion. In the active layer, there are no counts below 0.84 MeV, implying that noise levels below this energy will have no effect on the neutron detection efficiency. In addition, the active detector shows the presence of two additional peaks, the sum peaks, that occur at the energy corresponding to the sum of the Li and He energies. Both differences are a consequence of the charge production and capture process that occurs in the active layer. The process of electron-hole pair generation by secondary ions is shown in figure 9.2 (c) and (d). In an active layer, charges are captured over the entire path length of the highly energetic ions. In contrast, in a conversion layer, the ion will lose energy as it moves through the neutron capture layer and charge capture will occur only after it has reached the adjacent semiconducting layer. Hence in an active layer, the majority of neutron capture events will generate charge equivalent to the energy of one ion, in addition to a fraction of the energy of the other ion. The sum peaks occur when the trajectory of the Li and He ions is such that both ions lose all their energy within the device. In a conversion layer, only a fraction of the energy lost results in charge capture whereas in an ideal active layer, all the energy is converted to a charge

pulse. We shall see, however, that these distinctions are blurred when we consider non-ideal cases.

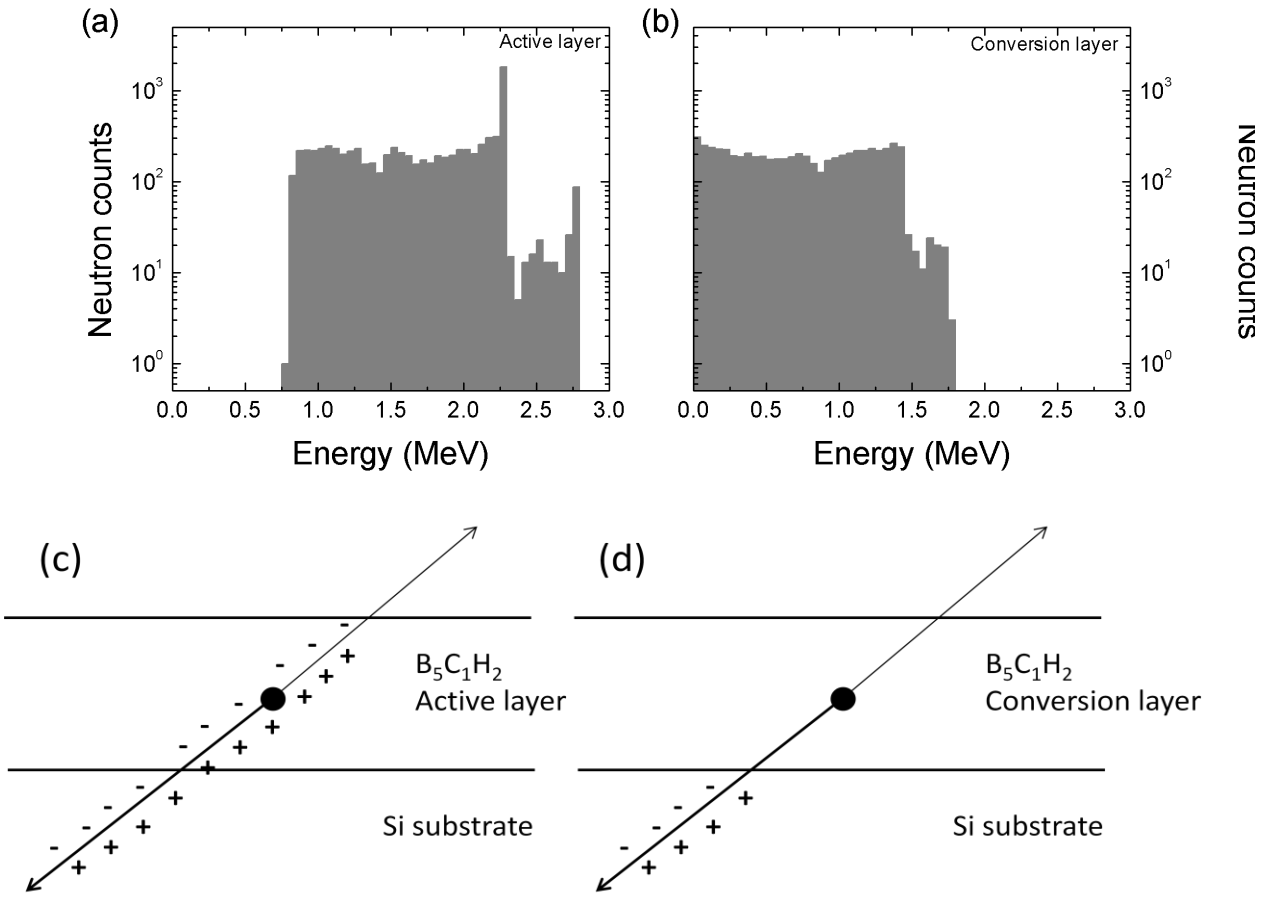

Figure 9. 2 Pulse height spectra of (a) an active layer and (b) a conversion layer detector in a GEANT4 simulation assuming ideal conditions. The number of incident neutrons is 10^6. The schematics in (c) and (d) illustrate the different mechanisms of electron-hole pair generation for active and conversion layer detectors. In the single-sided conversion layer detector, charge generation and capture occur only within the adjacent semiconductor.

The efficiencies of these ideal detectors as a function of thickness has been calculated using both GEANT4 and the equation

$$\text{Detection efficiency} = 1 - \mathrm{e}^{-(\sigma \rho\, l)} \tag{9.2}$$

where, σ is the absorption cross section of ^{10}B for thermal neutron

ρ is the number density of ^{10}B in the boron carbide material

l is the thickness of the neutron capture layer

These efficiencies, shown in figure 9.3, indicate that the conversion layer detection efficiency saturates at a thickness of about 4 μm, a thickness that is on the order of the range of the Li and He ions in this material. The ranges of the secondary ions in $B_5C_1H_2$ and Si were obtained from the SRIM/TRIM code developed by Ziegler, et al. [16]. The longest range is 3.94 μm for the ^4He (1.78 MeV) ion in the $B_5C_1H_2$ film as shown in table 9.1. Neutron capture events that occur beyond this range, further away from the interface with the semiconducting charge capture layer, will not result in a charge pulse in the conversion layer detector, resulting in lowered efficiency.

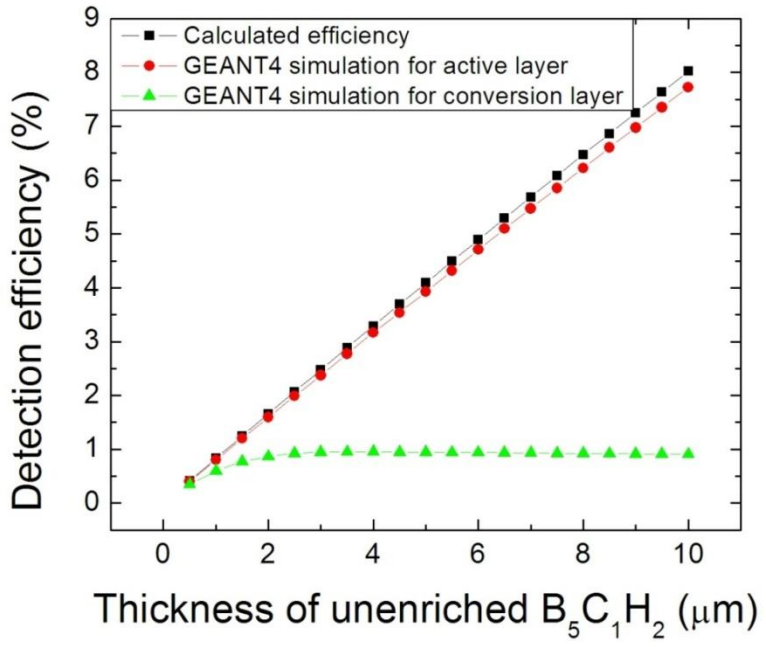

Figure 9. 3 Detection efficiencies obtained from equation (9.2) and GEANT4 simulations as a function of thickness of an unenriched $B_5C_1H_2$ film. The active layer shows a monotonic increase in efficiency (red circles) but the conversion layer efficiency peaks at about 4 um, the maximum range of the high energy ions produced during neutron capture.

Table 9. 1 Range of secondary ions in the $B_5C_1H_2$ film and the Si substrate calculated using the SRIM/TRIM code.

		^{7}Li (0.84 MeV)	^{7}Li (1.02 MeV)	^{4}He (1.47 MeV)	^{4}He (1.78 MeV)
Projected range	$B_5C_1H_2$	1.65 μm	1.86 μm	3.19 μm	3.94 μm
	Si	2.46 μm	2.82 μm	5.15 μm	6.36 μm

9.3 Effects of incomplete charge capture in active layer detectors

The properties of the semiconductor dictate the extent to which the ideal scenario outlined above will occur. The pulse height spectra shown in figure 9.2 assume that the entire energy of the Li and He ions is used to create electron-hole pairs and that every electron-hole pair that is created is captured at the electrodes and results in an electrical signature. However, if some fraction of the electrons and holes created by ionization are not captured at the electrodes [10], as can occur because of deep impurities in the semiconducting material or because of the high recombination rate of electron-hole pairs or because of any other types of charge traps which hold the charge for time scales that are longer than the signal processing time, the pulse height spectra will be shifted to apparently lower energies. The previous assumption of 100% charge capture efficiency in the $B_5C_1H_2$ film is unlikely because PECVD grown boron carbide has multiple polytypes [4], resulting in structural inhomogeneities and defects as well as deep impurity levels. In order to take account of these effects, we varied the charge collection efficiencies in the $B_5C_1H_2$ layer, while keeping that in the Si fixed at 100%.

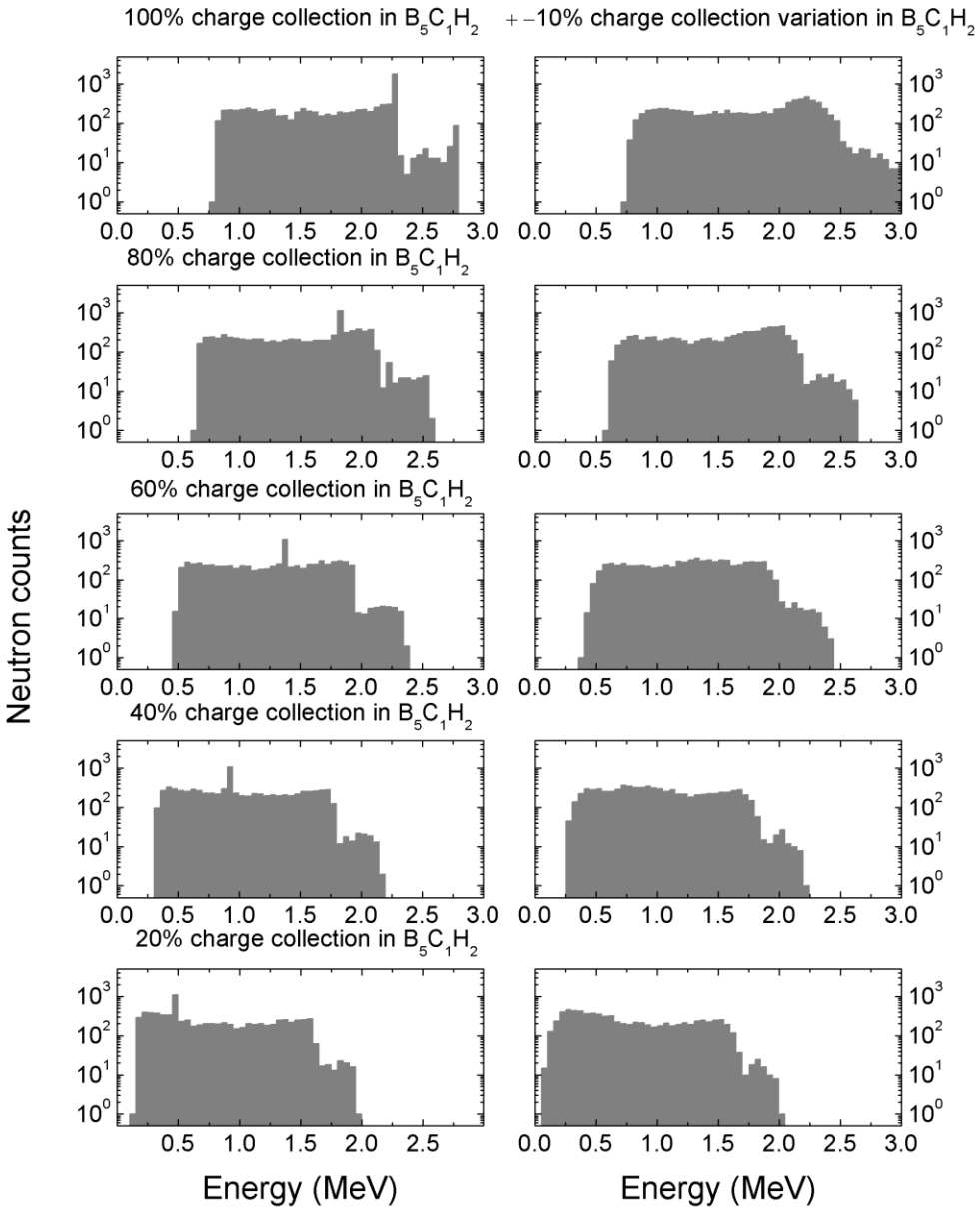

Figure 9. 4 Pulse height spectra obtained from GEANT4 simulations for a 1 μm thick active $B_5C_1H_2$ layer with incomplete charge collection efficiency. The left column shows the spectra for charge collection efficiencies ranging from 20% (bottom) to 100% (top). The right column allows for a variation of ±10% in the charge collection efficiency about the central value.

The left column of figure 9.4 shows the pulse height spectra generated by GEANT4 for five different charge collection efficiencies of the $B_5C_1H_2$ film, ranging from 100% to 20%. As the charge collection efficiency decreases, the charge collected at the electrodes is reduced, leading to red shifts (to lower energies) of the pulse height spectra. In particular, the two sharp sum peaks move to lower energy as the charge collection efficiency decreases. These peaks correspond to neutron capture events that result in full energy deposition *only* in the $B_5C_1H_2$ layer. For example, for 60% charge collection efficiency, the spectrum shows a sharp peak at 1.39 MeV, which is 60% of the full energy sum of ^{4}He (0.84 MeV) and ^{7}Li (1.47 MeV), and another at 1.68 MeV, 60% of the full energy sum of ^{4}He (1.02 MeV) and ^{7}Li (1.78 MeV).

Neutron capture events that result in deposition of the total energy in the device, but divided so that the full energy deposition occurs partly in the Si and partly in the $B_5C_1H_2$ layer will not result in sharp peaks, because the fraction of energy deposited within the $B_5C_1H_2$ layer will vary depending on the location of the neutron capture event in the $B_5C_1H_2$ layer and on the trajectory of the He and Li ions, leading to a wide distribution of charge signal. Although the simulated overall efficiency remains unaffected, the increasing shift of the spectrum to lower energies implies that, for any realistic experiments, larger fractions of the response signal will be subsumed into the noise

The right column shows the effect of allowing for a distribution of charge collection efficiencies—a much more realistic scenario. Variations in charge collection efficiency occur, for example, if radiation capture events take place at different depths [10] in the semiconductor. In this case, if the transit time to the electrodes is comparable to the recombination times, the corresponding charge collection efficiencies could vary considerably. Variations in the charge

collection efficiency may also occur due to inhomogeneities within the semiconductor, such as might occur for PECVD grown boron carbide films.

Each spectrum in the right column corresponds to a ±10% uncertainty in the charge collection centered about the charge collection efficiencies of the corresponding spectra in the left column. The probability for each charge collection efficiency within this ±10% range is assumed to be equal. Under this scenario, even at 100% charge collection efficiency, the full-energy peaks disappear. A smaller spread in charge collection efficiencies may result only in a blurring of the sharp peak. Variations in the charge collection efficiency broaden the spectral shape, shifting yet more weight into the low energy channels, further decreasing the signal-to-noise.

In the pulse height spectra, the energy of the peak positions (the y-axis) are related to the number of electron-hole pairs generated by E/ε where E is the energy of the ion deposited in the semiconductor material and ε is the ionization energy. The ionization energy of a semiconductor results from the Coulombic interactions between the ions and the electrons in a semiconductor, resulting in the ionization of a semiconductor atom and the subsequent generation of electron-hole pairs. The ionization energy has been empirically observed to be almost invariant with respect to the energy of incident charged particles [17]. The ionization energies for elements or binary compounds with tetrahedral bonding have been experimentally well characterized, by $\varepsilon = 2.67E_g + 0.87\ (\mathrm{eV})$ [12] where E_g is the direct or indirect bandgap energy. The ionization energy for semiconducting Si is 3.62 eV at 300 K [17]. If we use the same empirical results and the optical band gap of 2.2 eV [18] to calculate the ionization energy for boron carbide (which is not tetrahedral), we obtain a value of 6.744 eV. Higher ionization energies for $B_5C_1H_2$ (as compared to Si), will result in a smaller number of electron-hole pairs in the $B_5C_1H_2$ for an

identical deposition of energy, shifting the peaks to lower energy. In general, we expect differing ionization energies to result in a broadening of the features in the pulse height spectra.

9.4 Effect of noise lower level discriminators (LLD)

Any experimental measurement of neutron detection efficiencies must include the effects of detector noise and the ability to distinguish signals from electronic noise. The leakage current in a reverse biased semiconductor is the primary source of noise, but the entire system including the detection electronics contributes to the noise level. In order to simulate the effects of noise on the experimental detection efficiencies, we include a lower level discriminator (LLD) setting in our simulations, cutting off the signal from low energy channels in which noise is dominant. The effects on the efficiency are more marked in pulse height spectra that are weighted to lower energy channels as expected, revealing another advantage of active vs. conversion layer detectors, because, in active detectors, there is little to no signal in the lowest energy channels. In conversion layers, even under the assumptions of perfect charge collection and long depletion widths in the adjacent semiconductor, the expected pulse height spectrum has a sizable fraction of counts in the lowest energy channels. In contrast, in an active detector, even with only 40%±10% charge collection efficiency (see right column in figure 9.4), there is little to no signal below 0.25 MeV. To evaluate the effect of noise and a LLD on the detection efficiency, we can select a lower energy cut-off in the simulated spectrum and see how the detection efficiency varies with the choice of the cut-off.

Figure 9.5 shows the effect of the LLD on efficiencies for an ideal conversion layer detector and for two active layer detectors, with incomplete charge capture (40% and 80%). As expected, the efficiency of the conversion layer detector decreases at even the lowest LLD settings because the pulse height spectrum is weighted to lower energy. As the LLD level

increases, the corresponding detection efficiency decreases linearly. For active layer detectors with 40% and 80% charge collection efficiency, the neutron detection efficiencies remain constant for LLD settings as high as 0.3 MeV and 0.6 MeV, respectively. This feature which is unique to active layer detectors and is a consequence of the spectral shift to higher energies indicates that active layer detectors can tolerate noisy environments with their neutron detection capabilities intact. The sharp drops in the detection efficiency at LLD settings of 0.8 MeV and 1.6 MeV correspond to levels at which the sharp sum peaks appear in the pulse height spectra in figure 9.4 (left side). The detection efficiencies drop to zero at LLD settings of 2.4 MeV for 40% charge collection efficiency and 2.6 MeV for 80% charge collection efficiency. These correspond to the highest energies of the neutron detection signal as shown in figure 9.4 (left-hand side).

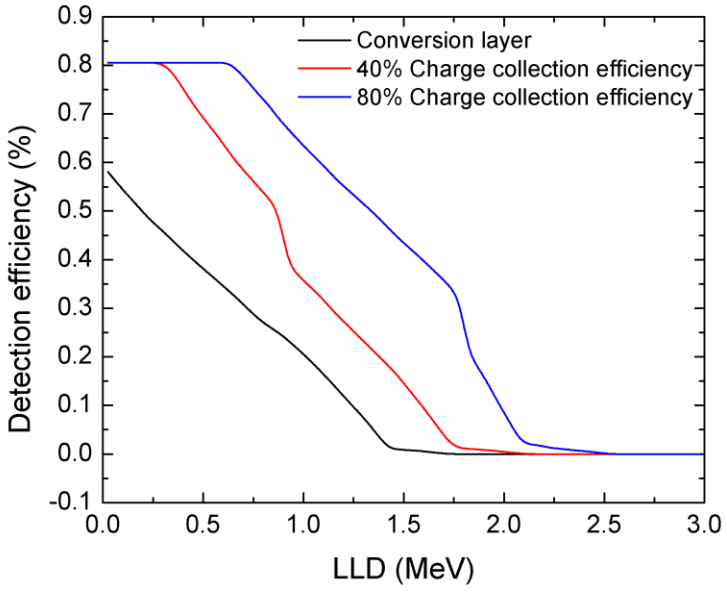

Figure 9. 5 Neutron detection efficiency as a function of LLD settings. The black curve denotes a $B_5C_1H_2$ conversion layer detector with 100% charge collection efficiency in the adjoining Si. The red and blue curves denote active layer detectors with 40% (red), and 80% (blue) charge collection efficiencies in the $B_5C_1H_2$ layer and 100% charge capture efficiency in the Si layer.

9.5 Conclusions

We have extended the GEANT4 toolkit to take into account the semiconducting properties of boron carbide, $B_5C_1H_2$, and have shown that the neutron detection signatures are highly dependent on the properties of the semiconductor. Incomplete charge collection, unequal ionization energies and variations within the materials are shown to shift and broaden the expected spectral response, resulting in pulse height spectra that blur the distinctions between active and conversion layer detectors. In particular, as the charge collection efficiency within the $B_5C_1H_2$ material decreases, the pulse height spectra shift to lower energies. In active layer detectors, this shift of the pulse height spectra to lower energies is not necessarily detrimental to the neutron detection efficiency, as long as the noise peak remains below a certain threshold, indicating that even with imperfect semiconducting properties, the neutron detection efficiencies of active layer detectors remain robust.

REFERENCES

1. Osberg, K., et al., *A Handheld Neutron-Detection Sensor System Utilizing a New Class of Boron Carbide Diode.* Sensors Journal, IEEE, 2006. **6**(6): p. 1531-1538.
2. Hong, N., et al., *Boron carbide based solid state neutron detectors: the effects of bias and time constant on detection efficiency.* Journal of Physics D: Applied Physics, 2010. **43**(27): p. 275101.
3. Day, E., M.J. Diaz, and S. Adenwalla, *Effect of bias on neutron detection in thin semiconducting boron carbide films.* Journal of Physics D: Applied Physics, 2006. **39**(14): p. 2920.
4. Day, E.E., *Boron carbide devices for neutron detection applications*, in *Ph.D. dissertation, The University of Nebraska - Lincoln*. 2006.
5. Caruso, A.N., et al., *The all boron carbide diode neutron detector: Comparison with theory.* Materials Science and Engineering: B, 2006. **135**(2): p. 129-133.
6. Harken, A.D., *Modeling and Signal Analysis of Semiconducting B_5C Neutron Detectors*, in *Ph.D. dissertation, The University of Nebraska - Lincoln*. 2006.
7. Lundstedt, C., et al., *Modeling solid-state boron carbide low energy neutron detectors.* Nuclear Instruments and Methods in Physics Research Section A: Accelerators, Spectrometers, Detectors and Associated Equipment, 2006. **562**(1): p. 380-388.
8. Goulding, F.S. and D.A. Landis, *Signal Processing for Semiconductor Detectors.* Nuclear Science, IEEE Transactions on, 1982. **29**(3): p. 1125-1141.
9. Radeka, V. and N. Karlovac, *Least-square-error amplitude measurement of pulse signals in presence of noise.* Nuclear Instruments and Methods, 1967. **52**(1): p. 86-92.

10. Shah, K.S., J.C. Lund, and F. Olschner, *Charge collection efficiency in a semiconductor radiation detector with a non-constant electric field.* Nuclear Science, IEEE Transactions on, 1990. **37**(2): p. 183-186.

11. *http://geant4.cern.ch/*.

12. Agostinelli, S., et al., *Geant4- a simulation toolkit.* Nuclear Instruments and Methods in Physics Research Section A: Accelerators, Spectrometers, Detectors and Associated Equipment, 2003. **506**(3): p. 250-303.

13. *The Perl Programmig Language, www.perl.org*.

14. Harken, A.D. and B.W. Robertson, *Comparative modelling of performance limits of solid-state neutron detectors based on planar B-rich capture layers.* Journal of Physics D: Applied Physics, 2006. **39**(23): p. 4961.

15. McGregor, D.S. and J. Kenneth Shultis, *Spectral identification of thin-film-coated and solid-form semiconductor neutron detectors.* Nuclear Instruments and Methods in Physics Research Section A: Accelerators, Spectrometers, Detectors and Associated Equipment, 2004. **517**(1-3): p. 180-188.

16. *James Ziegler - SRIM & TRIM, www.srim.org.*

17. Knoll, G.F., *Radiation detection and measurement*. 2nd ed. 1989, New York: Wiley.

18. Billa, R.B., *Optical properties of semiconducting boron carbide for neutron detection applications*, in *Ph.D. dissertation, The University of Nebraska - Lincoln*. 2009.

Chapter 10 Conclusions

The research reported in this dissertation has focused on the investigation of boron carbide based neutron detectors in the form of semiconducting boron carbide/Si heterostrcutured diodes. The two main thrusts were: (i) the fabrication of neutron detectors and experimental measurements and simulations (using GEANT4 modeling) of detector performance and (ii) material characterization of semiconducting boron carbide films to optimize the operating conditions for neutron detection applications.

Boron carbide films were deposited by plasma enhanced chemical vapor deposition (PECVD) technique on either n-type or p-type Si substrates and insulating glass or sapphire substrates with substrate temperatures of ~330 ℃. X-ray photoelectron spectroscopy results indicate that the process of chamber passivation was critical in obtaining the appropriate stoichiometry of boron carbide films. An important finding for the growth of thick uniform films was that minimizing the temperature gradient along the gas lines resulted in longer deposition times without arcing. The elemental compositions of thin and thick films with or without post-annealing at 600 ℃ were obtained by Rutherford backscattering and elastic recoil detection analysis. The results showed that the top 50 nm of the film surface were contaminated by carbon and oxygen from the atmosphere, but that the bulk region preserved the boron to carbon ratio of the precursor molecule at 5:1. Eight out of twelve (or four out of six) hydrogen atoms were eliminated during deposition leading to an elemental composition of $B_5C_1H_2$ for the PECVD grown boron carbide thin films. This may or may not be the chemical stoichiometry because of inhomogeneities within the film. The post-annealing treatment reduces the hydrogen concentration near the film surface as the hydrogen migrates into the bulk. Infrared (IR) and Raman spectra of undoped and Ni-doped boron carbide films were analyzed using the fingerprint

method by referring to previous research on icosahedral boron rich carbon compounds with various composition ratios. These measurements indicate that the icosahedral cage of the source molecule is preserved, as well as showing evidence of the expected center chains that would occur if the icosahedra formed a crystalline solid. Because we have seen no evidence of long range order from either x-ray diffraction or electron diffraction, we believe that the film is either amorphous or nanocrystalline with very small grains. IR spectroscopy of Ni-doped boron carbide showed significantly reduced icosahedral vibrations. The Raman spectra for both films were almost identical.

Heterojunction p-n diodes using p-type undoped boron carbide and an n-type Si wafer were examined by current-voltage (I-V) and capacitance-voltage (C-V) measurements for neutron detection. The I-V curve revealed a highly suppressed leakage current (nA to μA) with a high reverse break down voltage (>40 V) which enabled neutron detection measurements at high internal electric fields to sweep out charge, concurrently with low electronic noise. The carrier concentration for undoped boron carbide films ~4.5×10^{12} cm^{-3} was calculated from the C-V curve, using the step junction model. The neutron detection efficiency of the boron carbide p-n diode increased with increasing reverse bias voltages due to the longer depletion width and the higher electric field. Additional effects that optimized the neutron detection efficiency measurements are due to the long risetime (~20 μs) of the semiconducting boron carbide layer with respect to the short risetime (<20 ns) of the semiconducting Si layer. The differences in the signal transit time of each layer required a long enough time filter in the digital pulse processor to obtain fully convoluted signals.

We were able to attain highly accurate neutron detection efficiencies for a 640 nm boron carbide p-n diode detector at the instrumentation beamline at Oak Ridge National Lab. These

measurements confirmed the wavelength dependence of the cross section and showed that boron carbide neutron detectors could be used as reliable beam monitors.

The semiconducting properties of boron carbide alter the expected efficiencies and the pulse height spectra. The role of incomplete charge collection efficiency in PECVD grown boron carbides on the pulse height spectrum were simulated using a Monte Carlo GEANT4 simulation. Incomplete charge collection in an active layer heterojunction p-n diode detector results in a significant distortion of the pulse height spectrum in a form similar to the pulse height spectrum for a conversion layer detector. Simulations that include a lower level discriminator (LLD) to simulate the effect of noise revealed that incomplete charge collection efficiency reduced the neutron detection efficiency due to shifting of in the pulse height spectra to lower channel numbers, but that lowered noise (or LLD) levels can still lead to close to the expected efficiency.

There are significant advantages in using semiconducting boron carbide for neutron detection purposes. These include the low dark current of the p-n diode detector on an n-type Si substrate, low power operation at room temperature, good detection response to a wide wavelength range of neutrons, high temperature operation, small size, low mass and robustness. However, the scale of the detector is limited to a few inches at best with current deposition techniques and their use as portal monitors would require extensive technological development. The small size of such semiconducting boron carbide neutron detectors would, however, make them attractive as hand-held neutron detectors. The fundamental drawback for neutron detectors using PECVD grown boron carbides is the present low charge collection efficiency.

The results of this dissertation suggest that progress on this front could be made by achieving the following: The quickest (albeit expensive) method to increase efficiency is by

enriching the source compound to ~100% ^{10}B, which will enhance the neutron detection efficiency by a factor of 5. Further progress will come from enhanced geometries that minimize the effects of incomplete chare capture. First, a homojunction neutron detector utilizing Ni as n-type dopant could be fabricated in which the discrepancy between the charge collection times and efficiencies would be minimized, allowing for integration time constants that matched through the entire device. An ingenious method to minimize the effect of incomplete charge collection has been suggested by Professor Mathias Schubert, in analogy to techniques used in solar cells. Multiple homojunctions with interleaved ohmic contacts could be stacked in a multilayer structure as shown below. Because of the short distance to the electrodes, charge collection can be greatly enhanced; the overall thickness would be determined by the requirements for neutron efficiency. Alternatively, multiple layers of n- or p-type boron carbide layers sandwiched between Schottky contact metallic layers would also achieve this objective. Improvement of the semiconducting properties so as to increase the charge collection is of course also a viable route, albeit likely much slower for development. Over the period of this dissertation work, we have achieved substantial improvements in the operating parameters of the heterojunction diodes (low leakage currents, higher breakdown voltages, improved homogeneity, thicker films and improved film adhesion) and much greater consistency in the films.

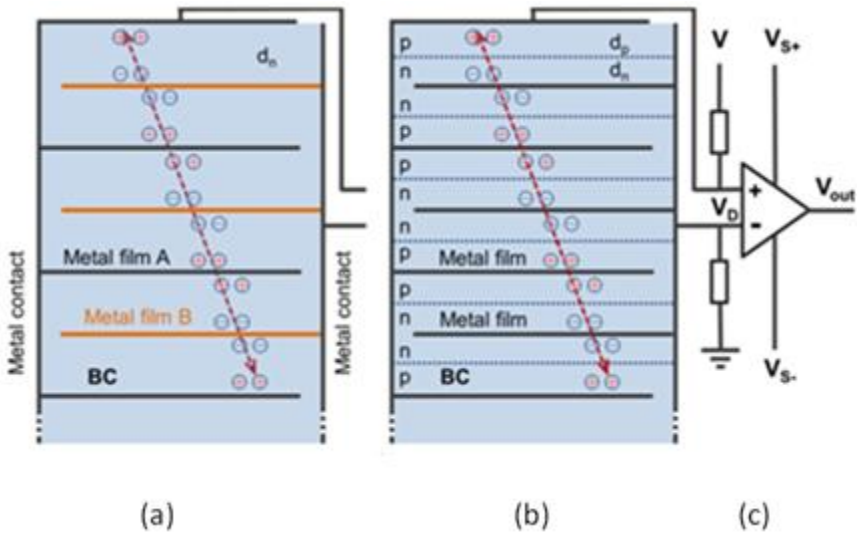

Figure 10. 1 (a) Proposed boron carbide semiconductor multilayer neutron detector sensor device with sequences of Schottky barriers established between biased (V_D), masked, back-to-back thin metal layer contacts. (b) Same as (a) with layer sequences of p-type n-type boron carbide homojunctions. Individual boron carbide layer thickness parameters (d_p, d_n) are optimized to match the free carrier mobility-life-time product. Collision-induced electron-hole pairs are separated by the internal electric field, and collected at the nearest electrode. (c) Differential input electronic voltage amplifier circuitry, supplied by small voltage V_S, discriminates capture events dV_d/dt for electronic processing. For optimum collection in (b), both p and n layers must be fully depleted. High-bias V_D and Schottky contacts are envisioned for (a). Low V_D and ohmic contacts are required for the p-n junction device (b). Multilayers are created, as needed, to reach total thickness d.

Appendix

Calibration of the neutron beam generate by MP 320 using the ^{3}He detector.

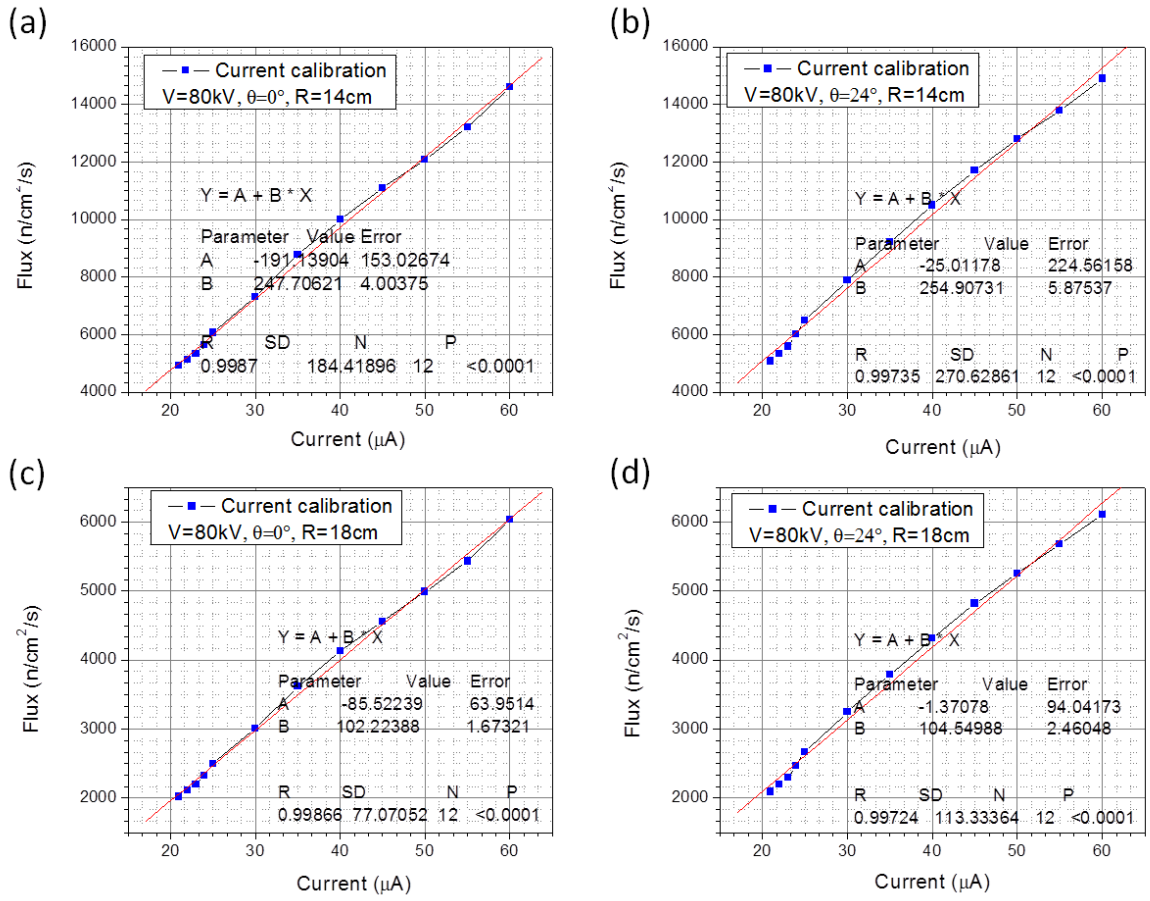

Figure A. 1 The neutron flux calibrated by varying current at a fixed voltage of 80 kV. The angular dependence is seen in the comparison between (a) and (b) and between (c) and (d) at distances of 14 cm, and 18 cm, respectively. The distance dependence of the flux is seen in the comparison between (a) and (c) and between (b) and (d) at constant angles of 0 ° and 24 °, respectively.

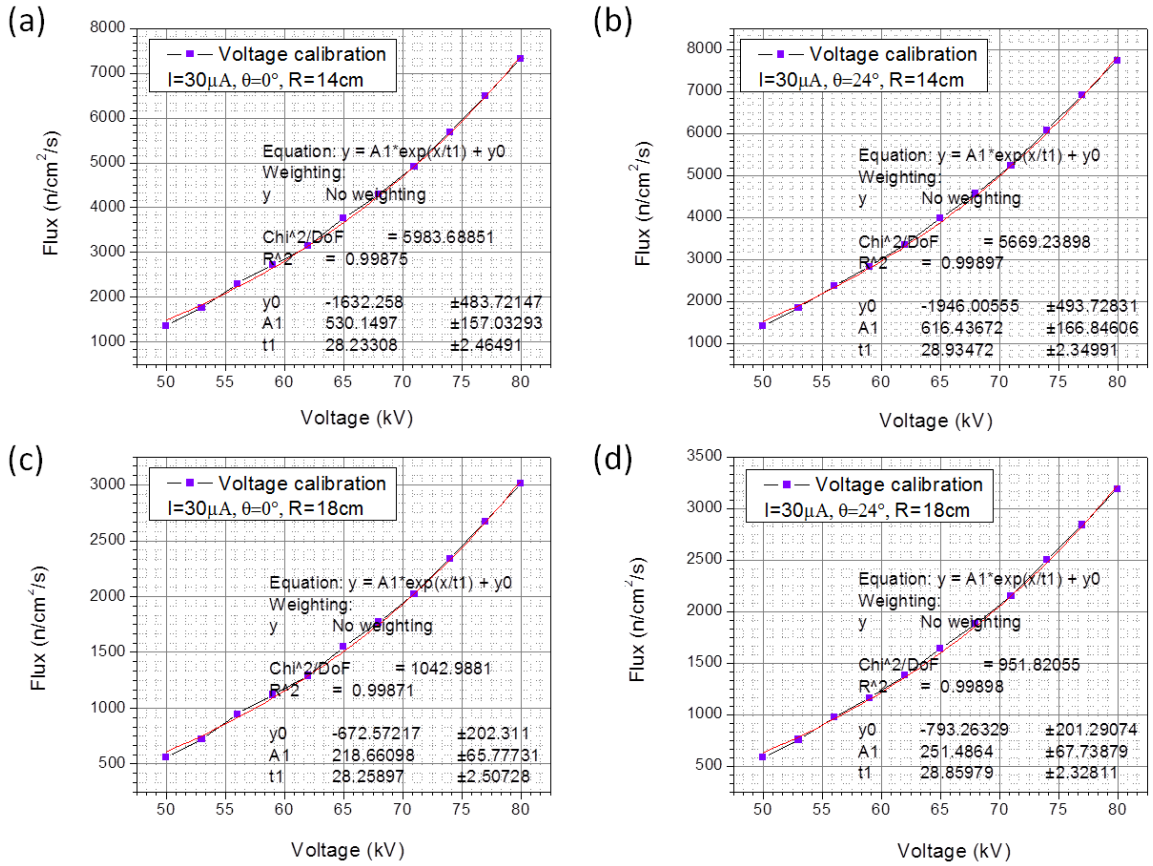

Figure A. 2 The neutron flux calibrated by varying voltage at a fixed current of 30 μA. The angular dependence is seen in the comparison between (a) and (b) and between (c) and (d) at distances of 14 cm and 18 cm, respectively. The distance dependence of the flux is seen in the comparison between (a) and (c) and between (b) and (d) at constant angles of 0 ° and 24 °, respectively.

Table A. 1 The neutron flux as a function of current at a fixed voltage of 80 kV with a detector at an angle of 0 º (top) and 24 º (bottom) to the MP 320 generator.

Current Calibration at V=80 kV, θ=0º

Voltage (KV)	Current (μA)	Flux (n/cm^2·s), R=18cm	Flux (n/cm^2·s), R=14cm
80	60	6.03×10^3	1.46×10^4
80	55	5.43×10^3	1.32×10^4
80	50	4.99×10^3	1.21×10^4
80	45	4.56×10^3	1.11×10^4
80	40	4.13×10^3	1.00×10^4
80	35	3.62×10^3	8.79×10^3
80	30	3.01×10^3	7.32×10^3
80	25	2.50×10^3	6.07×10^3
80	24	2.33×10^3	5.65×10^3
80	23	2.20×10^3	5.34×10^3
80	22	2.11×10^3	5.13×10^3
80	21	2.02×10^3	4.92×10^3

Current Calibration at V=80 kV, θ=24º

Voltage (kV)	Current (μA)	Flux (n/cm^2·s), R=18cm	Flux (n/cm^2·s), R=14cm
80	60	6.11×10^3	1.49×10^4
80	55	5.68×10^3	1.38×10^4
80	50	5.25×10^3	1.28×10^4
80	45	4.82×10^3	1.17×10^4
80	40	4.31×10^3	1.05×10^4
80	35	3.79×10^3	9.21×10^3
80	30	3.25×10^3	7.89×10^3
80	25	2.67×10^3	6.49×10^3
80	24	2.47×10^3	6.01×10^3
80	23	2.30×10^3	5.59×10^3
80	22	2.20×10^3	5.34×10^3
80	21	2.09×10^3	5.08×10^3

Table A. 2 The neutron flux as a function of voltage at a fixed current of 30 μA with the detector at an angle of 0 º (top) and 24 º (bottom) to the MP 320 generator.

Voltage Calibration at I=30 μA, θ=0º

Voltage (kV)	Current (μA)	Flux (n/cm^2·s), R=18cm	Flux (n/cm^2·s), R=14cm
50	30	5.60×10^2	1.36×10^3
53	30	7.23×10^2	1.76×10^3
56	30	9.47×10^2	2.30×10^3
59	30	1.12×10^3	2.72×10^3
62	30	1.29×10^3	3.14×10^3
65	30	1.55×10^3	3.77×10^3
68	30	1.77×10^3	4.29×10^3
71	30	2.02×10^3	4.92×10^3
74	30	2.34×10^3	5.69×10^3
77	30	2.67×10^3	6.49×10^3
80	30	3.01×10^3	7.32×10^3

Voltage Calibration at I=30 μA, θ=24º

Voltage (kV)	Current (μA)	Flux (n/cm^2·s), R=18cm	Flux (n/cm^2·s), R=14cm
50	30	5.86×10^2	1.42×10^3
53	30	7.58×10^2	1.84×10^3
56	30	9.73×10^2	2.36×10^3
59	30	1.16×10^3	2.82×10^3
62	30	1.38×10^3	3.35×10^3
65	30	1.64×10^3	3.98×10^3
68	30	1.88×10^3	4.56×10^3
71	30	2.15×10^3	5.23×10^3
74	30	2.50×10^3	6.07×10^3
77	30	2.84×10^3	6.91×10^3
80	30	3.19×10^3	7.74×10^3